High Order Stochastic Transport and Lagrangian Data Assimilation

by

Arkopal Dutt

B.Tech, Indian Institute of Technology Bombay (2015)

Submitted to the Department of Mechanical Engineering
in partial fulfillment of the requirements for the degree of

Master of Science in Mechanical Engineering

at the

MASSACHUSETTS INSTITUTE OF TECHNOLOGY

February 2018

Author . . . .

Signature redacted

Department of Mechanical Engineering
January 18, 2018

Signature redacted

Certified by . . . .

Pierre F.J. Lermusiaux
Professor, Department of Mechanical Engineering
Thesis Supervisor

Signature redacted

Accepted by . . . .

Rohan Abeyaratne
Chairman, Department Committee on Graduate Theses

High Order Stochastic Transport and Lagrangian Data Assimilation

by

Arkopal Dutt

Abstract

Ocean currents transport a variety of natural (e.g. water masses, phytoplankton, zoo-plankton, sediments, etc.) and man-made materials (e.g. pollutants, floating debris, particulate matter, etc.). Understanding such uncertain Lagrangian transport is imperative for reducing environmental damage due to natural hazards and for allowing rigorous risk analysis and effective search and rescue. While secondary variables and trajectories have classically been used for the analyses of such transports, Lagrangian Coherent Structures (LCSs) provide a robust and objective description of the important material lines. To ensure accurate and useful Lagrangian hazard scenario predictions and prevention, the first goal of this thesis is to obtain accurate probabilistic prediction of the underlying stochastic velocity fields using the Dynamically Orthogonal (DO) approach. The second goal is to merge data from both Eulerian and Lagrangian observations with predictions such that the whole information content of observations is utilized.

In the first part of this thesis, we develop high-order numerical schemes for the DO equations that ensure efficiency, accuracy, stability, and consistency between the Monte Carlo (MC) and DO solutions. We discuss the numerical challenges in applying the DO equations to the unsteady stochastic Navier-Stokes equations. In order to maintain consistent evaluation of advection terms, we utilize linear centered advection schemes with fully explicit and linear Shapiro filters. We then discuss how to combine the semi-implicit projection method with new high order implicit-explicit (IMEX) linear multi-step and multistage IMEX-RK time marching schemes for the coupled DO equations to ensure further stability and accuracy. We also review efficient numerical re-orthonormalization strategies during time marching. We showcase our results with stochastic test cases of stochastic passive tracer advection in a deterministic swirl flow, stochastic flow past a cylinder, and stochastic lid-driven cavity flow. We show that our schemes improve the consistency between reconstructed DO realizations and the corresponding MC realizations, and that we achieve the expected order of accuracy.

In the second part of the work, we first undertake a study of different Lagrangian

instruments and outline how the DO methodology can be applied to obtain Lagrangian variables of stochastic flow maps and LCS in uncertain flows. We then review existing methods for Bayesian Lagrangian data assimilation (DA). Disadvantages of earlier methods include the use of approximate measurement models to directly link Lagrangian variables with Eulerian variables, the challenges in respecting the Lagrangian nature of variables, and the assumptions of linearity or of Gaussian statistics during prediction or assimilation. To overcome these, we discuss how the Gaussian Mixture Model (GMM) DO Filter can be extended to fully coupled Eulerian-Lagrangian data assimilation. We define an augmented state vector of the Eulerian and Lagrangian state variables that directly exploits the full mutual information and complete the Bayesian DA in the joint Eulerian-Lagrangian stochastic subspace. Results of such coupled Eulerian-Lagrangian DA are discussed using test cases based on a double gyre flow with random frequency.

Thesis Supervisor: Pierre F.J. Lermusiaux
Title: Professor, Department of Mechanical Engineering

Acknowledgments

First and foremost, I would like to thank my advisor Prof. Pierre Lermusiaux for his wonderful guidance, incredible support and invaluable advice. I am also extremely grateful to him for being infinitely patient and understanding. I have learned a tremendous amount from him throughout the last few years both on academic and personal fronts, and hope to learn much more in the future.

I would like to thank Dr. Pat Haley for all the help with MSEAS cluster and software. I am extremely grateful to him for numerous discussions and help with my presentations. Thank you Pierre and Pat for keeping the MSEAS team in high spirits during crunch situations with your jovial comments.

Thank you to Chris Mirabito for helping me with all the MSEAS website updates. Thank you to Sudip Jana for sharing Bengali jokes with me and testing the trajectory code.

The warm and "dusty" confines of the MSEAS research lab have become a second home. Thank you to Tapovan, John, Matt and Sydney for welcoming me to the lab. Jing (aka Master Shifu) has patiently answered all my questions over the years and has been a great swimming buddy along with Corbin. Thank you for sharing my enthusiasm for seafood and being such a great friend. Deepak-thank you for your life lessons, and advice on how to hone my presentation skills. It was fun navigating the AGU 2017 conference with you. Chinmay-thank you for being such a great roommate in the first year (and putting up with my weird idiosyncrasies), occasional project partner and all the reddit humor you bring into the group. Thanks to Corbin for always pushing me to go for swimming, listening to me talk on and on, and your quick wit that sparks happiness into our daily lives. Thanks to Johnathan (aka Jvo) for being the other foodie on the 8th floor of Sidpac! Florian, merci beaucoup for

5

Contents

List of Figures

11

12

13

14

List of Algorithms

Chapter 1

Introduction

1.1 Background and Motivation

Data assimilation has long been used in meteorology for numerical weather prediction [29] and in oceanography to better understand and predict ocean dynamics [63, 54, 55, 38, 86]. The process of merging measurements which contain information regarding the true state of a system with predictions from models to improve knowledge of the state is referred to as data assimilation [28, 49, 98]. Predictions from dynamical models involve uncertainty from different sources such as model uncertainty when the dynamical model governing the interactions between the different physical processes is not well known, imprecise knowledge of initial conditions, boundary conditions, forcing, parameters, and unresolved processes of spatial and temporal scales that may not interact or contribute strongly to the main physical process being modeled [55, 62, 58]. At the same time, available measurements are both sparse in time and space. It then becomes necessary to use both dynamical model and data to understand how a dynamical system evolves.

In the context of oceans, one may need to describe density, temperature, salinity, pressure and velocity to completely define the state. To understand and predict how material transport is organized, it is imperative to look at advection of material in the flow and Lagrangian Coherent Structures (LCS) which influence and organize material transport. Measurements may or may not be available in these variables

for assimilation. The different types of sensors used to make measurements include Eulerian instruments (e.g. fixed sensors, moorings, etc.) and Lagrangian instruments (e.g. drifters, floats, etc.). The differences between these instruments and the types of measurements they make are discussed later in chapter 3. Most methods of data assimilation have focused on incorporating observations made by Eulerian instruments. It is only in the past two decades that different methodologies [13, 51, 46, 82, 84] are being developed to assimilate observations made by Lagrangian instruments. It is desirable to assimilate Lagrangian data as such observations can have more spatial coverage and be more economical. Ideally, the assimilation methodology should provide the true Bayesian estimate combining all information rigorously in accord with probability densities. As a result, it should be capable of assimilating all of the Eulerian and Lagrangian information content of observations. This forms the core goal of this work.

1.2 Goal of this Work

In order to address the above challenges, this thesis develops numerical schemes for a reduced order approach for making high-order probabilistic predictions for stochastic Navier-Stokes and Boussinesq fluid flows and formulates a rigorous methodology for Eulerian-Lagrangian data assimilation. Specifically this involves:

1. **Probabilistic predictions of stochastic fluid flows** - develop and verify new numerical schemes for the Dynamically Orthogonal (DO) field equations that maintain consistency, accuracy, and efficiency in the DO solution

2. **Assimilation methodology for joint Eulerian-Lagrangian state estimation** - extend and apply the Gaussian Mixture Model (GMM)-DO filter to joint Eulerian-Lagrangian data assimilation, exploiting the nonlinear governing equations and Bayesian mutual information

18

1.3 Layout of Thesis

In chapter 2, new numerical schemes for the DO equations applied to the stochastic Navier-Stokes equations are formulated. We first provide an overview of the DO equations and the numerical challenges involved in the time-integration of these equations when applied to the stochastic Navier-Stokes equations. We then discuss how these numerical challenges may be overcome by using a suitable advection scheme with filtering and high-order implicit-explicit (IMEX) time-marching schemes. This is followed by a discussion on time-stepping and re-orthonormalization techniques. Finally, we verify the consistency and accuracy of these numerical schemes by applications to the stochastic passive tracer advection in a deterministic swirl flow, stochastic flow past a cylinder, and stochastic lid-driven cavity flow.

In chapter 3, a new methodology is proposed for Bayesian Eulerian-Lagrangian data assimilation. We first discuss the different types of Lagrangian instruments and the types of measurements that they make in the ocean. This is followed by a discussion on how Lagrangian Coherent Structures (LCS) may be described using the measure of the finite-time Lyapunov exponent (FTLE). A brief overview of how these may be obtained in stochastic flow is presented. We then give the formal problem statement of joint Eulerian-Lagrangian data assimilation with a survey of the existing methodologies in literature and the challenges that need to be handled. We then describe how the Gaussian Mixture Model (GMM)-DO filter can be extended to handle these challenges. Finally, the application of the methodology is presented considering the test case of stochastic double-gyre flow.

Summary of results, concluding remarks and future directions are given in chapter 4.

Chapter 2

Numerical Schemes for Dynamically Orthogonal Equations

Uncertainty quantification has become an important tool for making probabilistic predictions of truly stochastic dynamical systems or understanding the impact of error or imprecise knowledge in data such as initial conditions, boundary conditions, parameters, etc. [131, 52]. The most popular method in uncertainty quantification has been the Monte Carlo method and its variants which are all sampling based methods. Nonsampling methods include perturbation methods [72, 73] where random fields are expressed in their truncated Taylor series expansion around the mean. These methods do not perform well when magnitudes of uncertainty are high. Other methods include moment equations and operator-based methods [17, 18, 133]. Recently developed methods include Proper Orthogonal Decomposition (POD) method which was historically applied to turbulent flows [85, 78, 45] and generalized polynomial chaos (gPC) [132] which uses spectral representations in the random space. Here, we will focus on the Dynamically Orthogonal (DO) equations which was shown to be a generalization of the generalized PC and POD methods in [96].

2.1 Dynamically Orthogonal Equations

2.1.1 Review

Suppose that we are interested in the dynamics of the continuous stochastic field $X(\mathbf{r}, t; \omega)$ which is governed by the following stochastic partial differential equation (SPDE)

$$\frac{\partial X(\mathbf{r}, t; \omega)}{\partial t} = \mathcal{L}\left[X(\mathbf{r}, t; \omega); \omega\right], \quad \mathbf{r} \in \mathcal{D}, \ t \in \mathcal{T}, \ \omega \in \Omega \tag{2.1}$$

with stochastic initial conditions

$$X(\mathbf{r}, t_0; \omega) = X_0(\mathbf{r}; \omega) \tag{2.2}$$

and stochastic boundary conditions

$$\mathcal{B}\left[X(\mathbf{r}, t; \omega)\right]_{\mathbf{r}=\boldsymbol{\xi}} = h(\boldsymbol{\xi}, t; \omega) \tag{2.3}$$

where $\mathcal{B}$ is a linear differential operator and $\boldsymbol{\xi}$ denotes the spatial coordinate along the boundary.

The first step of the DO methodology involves taking the generalized time-dependent Karhunen-Loève (KL) decomposition of the stochastic process $X(\mathbf{r}, t; \omega)$

$$X(\mathbf{r}, t; \omega) = \bar{\mathbf{x}}(\mathbf{r}, t) + \sum_{i=1}^{n_s} \Phi_i(t; \omega) \tilde{\mathbf{x}}_i(\mathbf{r}, t) \tag{2.4}$$

where $\bar{\mathbf{x}}(\mathbf{r}, t)$ is the mean field, $\tilde{\mathbf{x}}_i(\mathbf{r}, t)$ are the orthonormal modes which forms a basis of the time-dependent stochastic subspace, $\Phi_i(t; \omega)$ are zero-mean stochastic processes, and n_s represents the number of first dominant modes which are retained in the decomposition and is also size of the stochastic subspace. The KL decomposition is the best biorthogonal approximation of the original stochastic process [74, 1] in terms of minimizing mean square error due to truncation. This is analogous to the singular value decomposition for matrices. It should be noted that both the modal basis and the stochastic coefficients are evolved in time and this is why the DO methodology is

a more general formulation than Polynomial Chaos (PC) [132] where the stochastic coefficients $\Phi_i(t;\omega)$ are fixed in time or Proper Orthogonal Decomposition (POD) [45] where the modes are fixed in time.

The DO evolution equations are obtained by enforcing the dynamically orthogonality condition of

$$\left\langle \frac{\partial \tilde{\mathbf{x}}_i(\cdot,t)}{\partial t}, \tilde{\mathbf{x}}_j(\cdot,t) \right\rangle = 0 \quad \forall i \neq j \in \{1,2,...,n_s\} \tag{2.5}$$

that is the stochastic subspace can evolve only orthogonal to itself. The operator $\langle a, b \rangle$ is the spatial inner product defined as

$$\langle a(\cdot,t), b(\cdot,t) \rangle = \int_{\mathcal{D}} a(\mathbf{r},t)^T b(\mathbf{r},t) d\mathbf{r} \tag{2.6}$$

The evolution equations of the mean, modes and stochastic coefficients respectively are given by (using Einstein notation)

$$\begin{cases} \dfrac{\partial \bar{\mathbf{x}}(\mathbf{r},t)}{\partial t} = \mathbb{E}\left[\mathcal{L}\left[\mathbf{X}(\mathbf{r},t;\omega);\omega\right]\right] \\ \dfrac{\partial \tilde{\mathbf{x}}_i(\mathbf{r},t)}{\partial t} = \Pi_{\mathcal{X}}^{\perp}\left(\mathcal{L}\left[\mathbf{X}(\mathbf{r},t;\omega);\omega\right]\Phi_j(t;\omega)\right)\mathbb{C}_{\Phi_i(t)\Phi_j(t)}^{-1} \\ \dfrac{d\Phi_i(t;\omega)}{dt} = \left\langle \mathcal{L}\left[\mathbf{X}(\mathbf{r},t;\omega);\omega\right] - \mathbb{E}\left[\mathcal{L}\left[\mathbf{X}(\mathbf{r},t;\omega);\omega\right]\right], \tilde{\mathbf{x}}_i(\mathbf{r},t) \right\rangle \end{cases} \tag{2.7}$$

where $\mathbb{E}[\bullet]$ is the expectation operator, and $\Pi_{\mathcal{X}}^{\perp}[\mathbf{z}]$ is the projection of the vector $\mathbf{z}$ onto the space orthogonal to the stochastic subspace.

$$\Pi_{\mathcal{X}}^{\perp}[\mathbf{z}] = \mathbf{z} - \Pi_{\mathcal{X}}[\mathbf{z}] = \mathbf{z} - \sum_{i=1}^{n_s}\langle \mathbf{z}, \tilde{\mathbf{x}}_i(\mathbf{r},t)\rangle\tilde{\mathbf{x}}_i(\mathbf{r},t) \tag{2.8}$$

The boundary conditions governing the mean and modes are given by

$$\mathcal{B}\left[\bar{\mathbf{x}}(\mathbf{r},t)\right]_{\mathbf{r}=\boldsymbol{\xi}} = \mathbb{E}[h(\boldsymbol{\xi},t;\omega)] \tag{2.9}$$

$$\mathcal{B}\left[\tilde{\mathbf{x}}_i(\mathbf{r},t)\right]_{\mathbf{r}=\boldsymbol{\xi}} = \sum_{j=1}^{n_s}\mathbb{E}[\Phi_j(t;\omega)h(\boldsymbol{\xi},t;\omega)]\mathbb{C}_{\Phi_i(t)\Phi_j(t)}^{-1} \tag{2.10}$$

The initial conditions are obtained through the KL decomposition and retaining the

23

dominant n_s modes. If one chooses to use $\{\tilde{\mathbf{x}}_{i0}\mathbf{r}\}_{i=1}^{n_s}$ as the modal basis to describe the stochastic subspace at time 0 then,

$$\bar{\mathbf{x}}(\mathbf{r}, t_0) = \mathbb{E}[\mathbf{X}_0(\mathbf{r}; \omega)] \tag{2.11}$$

$$\tilde{\mathbf{x}}(\mathbf{r}, t_0) = \tilde{\mathbf{x}}_{i0}\mathbf{r} \tag{2.12}$$

$$\Phi_i(t_0; \omega) = \langle \mathbf{X}_0(\cdot; \omega) - \bar{\mathbf{x}}_0(\cdot), \tilde{\mathbf{x}}_{i0}(\cdot) \rangle \tag{2.13}$$

A complete derivation of the DO equations can be found in [95] and details regarding handling stochastic boundary conditions in [35].

With the DO methodology, we have reduced the original stochastic partial differential equation of dimension n_X to (i) a partial differential equation (PDE) of dimension n_X for the mean, (ii) n_s PDEs of dimension n_X for the orthonormal bases which describe the stochastic subspace, and (iii) a set of stochastic differential equations which represents how the uncertainty evolves in the stochastic subspace through time. If the stochastic coefficients are represented using n_{MC} sampled Monte Carlo realizations [1], then this set of stochastic differential equations is transformed into $n_s \times n_{MC}$ ordinary differential equations (ODEs). Hence, the DO methodology is an efficient reduced-order approach of propagating uncertainty in stochastic dynamical systems.

2.1.2 Application to Navier-Stokes Equations

We are now interested in applying the DO methodology to the stochastic incompressible Navier-Stokes equations

$$\begin{cases} \nabla \cdot \mathbf{u}(\mathbf{r}, t; \omega) = 0 \\ \dfrac{\partial \mathbf{u}(\mathbf{r}, t; \omega)}{\partial t} + \mathbf{u}(\mathbf{r}, t; \omega) \cdot \nabla \mathbf{u}(\mathbf{r}, t; \omega) = -\nabla p(\mathbf{r}, t; \omega) \\ \hspace{4cm} + \nu(\mathbf{r}; \omega)\nabla^2 \mathbf{u}(\mathbf{r}, t; \omega) + \mathbf{f}(\mathbf{r}, t; \omega) \end{cases} \tag{2.14}$$

---

[1]To make sure the samples are representative of the uncertainty in each mode, it is suggested to use $n_{MC} \gg n_s$

where $\mathbf{u}$ is velocity, p is pressure divided by density of the fluid [2], ν is the kinematic viscosity and $\mathbf{f}$ a forcing term. In general, stochasticity can be introduced through initial conditions, boundary conditions, forcing terms, and parameters (e.g. viscosity, density, etc.). The stochastic initial conditions are expressed as

$$\mathbf{u}(\mathbf{r}, t_0; \omega) = \mathbf{u}_0(\mathbf{r}; \omega) \tag{2.15}$$

and the stochastic boundary conditions are separated according to the regions where Dirichlet and Neumann boundary conditions are enforced

$$\mathbf{u}(\mathbf{r}, t; \omega) = h_D(\mathbf{r}, t; \omega), \quad \mathbf{r} \in \partial \mathcal{D}_D, \quad \omega \in \Omega \tag{2.16}$$

$$\frac{\partial \mathbf{u}(\mathbf{r}, t; \omega)}{\partial n} = h_N(\mathbf{r}, t; \omega), \quad \mathbf{r} \in \partial \mathcal{D}_N, \quad \omega \in \Omega \tag{2.17}$$

To obtain the stochastic DO Navier-Stokes equations, we consider the following DO decompositions of velocity and pressure

$$\mathbf{u}(\mathbf{r}, t; \omega) = \bar{\mathbf{u}}(\mathbf{r}, t) + \sum_{i=1}^{n_s} Y_i(t; \omega) \tilde{\mathbf{u}}_i(\mathbf{r}, t) \tag{2.18}$$

$$p(\mathbf{r}, t; \omega) = \bar{p}(\mathbf{r}, t) + \sum_{i=1}^{n_s} Y_i(t; \omega) \tilde{p}_i(\mathbf{r}, t) \tag{2.19}$$

where they share the same set of stochastic coefficients Y_i. The initial DO decomposition is obtained by taking the KL decomposition of the initial conditions (eq. (2.15)) and retaining n_s modes. The stochastic DO Navier-Stokes equations can be obtained by applying the DO methodology described in the previous section to the stochastic Navier-Stokes equations (eq. (2.14)).

---

[2]For brevity, we will refer to p simply as pressure in rest of this work.

Mean

The evolution equation is given by

$$\begin{cases} \nabla \cdot \bar{\mathbf{u}} = 0 \\ \dfrac{\partial \bar{\mathbf{u}}}{\partial t} = -\nabla \cdot (\bar{\mathbf{u}}\bar{\mathbf{u}}) - \mathbb{C}_{Y_i Y_j} \nabla \cdot (\tilde{\mathbf{u}}_j \tilde{\mathbf{u}}_i) - \nabla \bar{p} + \nu \nabla^2 \bar{\mathbf{u}} \end{cases} \qquad (2.20)$$

with boundary conditions

$$\bar{\mathbf{u}}(\mathbf{r}, t) = \mathbb{E}[\mathbf{h}_D(\mathbf{r}, t; \omega)] = \bar{\mathbf{h}}_D, \quad \mathbf{r} \in \partial \mathcal{D}_D, \quad \omega \in \Omega \qquad (2.21)$$

$$\frac{\partial \bar{\mathbf{u}}(\mathbf{r}, t)}{\partial n} = \mathbb{E}[\mathbf{h}_N(\mathbf{r}, t; \omega)] = \bar{\mathbf{h}}_N, \quad \mathbf{r} \in \partial \mathcal{D}_N, \quad \omega \in \Omega \qquad (2.22)$$

and initial conditions

$$\bar{\mathbf{u}}(\mathbf{r}, t_0) = \mathbb{E}[\mathbf{u}_0(\mathbf{r}; \omega)] = \bar{\mathbf{u}}_0(\mathbf{r}; \omega) \qquad (2.23)$$

Modes

The evolution equation is given by

$$\begin{cases} \nabla \cdot \tilde{\mathbf{u}}_i = 0 \\ \dfrac{\partial \tilde{\mathbf{u}}_i}{\partial t} = \mathbf{Q}_i - \langle \mathbf{Q}_i, \tilde{\mathbf{u}}_j \rangle \tilde{\mathbf{u}}_j \end{cases} \qquad (2.24)$$

where

$$\mathbf{Q}_i = \nu \nabla^2 \tilde{\mathbf{u}}_i - \nabla \cdot (\bar{\mathbf{u}}\tilde{\mathbf{u}}_i) - \nabla \cdot (\tilde{\mathbf{u}}_i \bar{\mathbf{u}}) - \nabla \tilde{p}_i - \mathbb{C}_{Y_i Y_j}^{-1} \mathbb{M}_{Y_j Y_m Y_n} \nabla \cdot (\tilde{\mathbf{u}}_n \tilde{\mathbf{u}}_m) \qquad (2.25)$$

and $\mathbb{M}_{Y_j Y_m Y_n} = \mathbb{E}\left[Y_j Y_m Y_n\right]$

The boundary conditions are

$$\tilde{\mathbf{u}}_i(\mathbf{r}, t) = \sum_{j=1}^{n_s} \mathbb{E}[\Phi_j(t; \omega) \mathbf{h}_D(\mathbf{r}, t; \omega)] \mathbb{C}_{\Phi_i(t)\Phi_j(t)}^{-1} = \tilde{\mathbf{h}}_{i,D}, \quad \mathbf{r} \in \partial \mathcal{D}_D, \quad \omega \in \Omega \qquad (2.26)$$

$$\frac{\partial \bar{\mathbf{u}}(\mathbf{r}, t)}{\partial n} = \sum_{j=1}^{n_s} \mathbb{E}[\Phi_j(t; \omega) \mathbf{h}_N(\mathbf{r}, t; \omega)] \mathbb{C}_{\Phi_i(t)\Phi_j(t)}^{-1} = \tilde{\mathbf{h}}_{i,N}, \quad \mathbf{r} \in \partial \mathcal{D}_N, \quad \omega \in \Omega \qquad (2.27)$$

with initial conditions as

$$\tilde{\mathbf{u}}_i(\mathbf{r}, t_0) = \tilde{\mathbf{u}}_{i,0}(\mathbf{r}) \tag{2.28}$$

Stochastic Coefficients

Their evolution is given by

$$\frac{dY_i}{dt} = \langle \Psi_m, \tilde{\mathbf{u}}_i \rangle Y_m - \langle \nabla \cdot (\tilde{\mathbf{u}}_n \tilde{\mathbf{u}}_m), \tilde{\mathbf{u}}_i \rangle (Y_m Y_n - \mathbb{C}_{Y_m Y_n}) \tag{2.29}$$

where

$$\Psi_m = \nu \nabla^2 \tilde{\mathbf{u}}_m - \nabla \cdot (\tilde{\mathbf{u}}_m \bar{\mathbf{u}}) - \nabla \cdot (\bar{\mathbf{u}} \tilde{\mathbf{u}}_m) - \nabla \tilde{p}_m \tag{2.30}$$

The initial conditions of the stochastic coefficients are obtained by projecting the full stochastic field onto the corresponding mode after removal of the mean

$$Y_i(t_0; \omega) = \langle \mathbf{u}_0 - \bar{\mathbf{u}}_0, \tilde{\mathbf{u}}_{i,0}(\mathbf{r}) \rangle \tag{2.31}$$

Alternately one can use knowledge of the stochastic field when constructing the KL decomposition e.g. the stochastic coefficients are Gaussian for a Gaussian process.

The details of the stochastic DO Navier-Stokes equations is now complete. For a full derivation, the reader should refer [124] which actually discusses the case of stochastic Boussinesq equations. The numerical study that we describe in this work can be easily extended to stochastic Boussinesq equations.

2.1.3 Numerical Challenges

One of the broad goals of this work is to develop high-order numerical schemes for the DO equations that ensure efficiency, accuracy, stability, and consistency between the Monte Carlo (MC) and DO solutions. In order to maintain consistency between the DO and MC solutions, we also need to ensure consistency in how advection terms are evaluated in the two cases. This is difficult as the modes of velocity $\tilde{\mathbf{u}}_i$ do not contain any directional information. Adapting advection schemes used for Monte Carlo realizations then becomes a challenge for advection terms of the form

$\nabla \cdot (\tilde{u}_j \tilde{u}_i)$ and $\nabla \cdot (\tilde{u}_i \bar{u})$ i.e. when the physical quantities are being advected by the modes of velocity. One solution is to evaluate these terms in a Monte Carlo fashion. This maintains consistency but is computationally expensive. Another approach is to use an upwinding scheme considering the DO mean $\bar{u}$ for directional information [69] but this is only justified for small uncertainties. There also exists Taylor series approaches [16] but these become inaccurate when the PDFs are skewed and also when uncertainties in the field variables are high. Another approach which has been quite successful is to average numerical fluxes according to the PDFs of velocity direction [124]. The idea is since stochastic coefficients Y_i have zero mean, an upwinding scheme [68] could be used to evaluate the advection terms considering both directions and then average the results. The advection scheme chosen in [124] was the total variation diminishing (TVD) scheme with a monotonically centered (MC) symmetric flux limiter [126]. We will refer to this resulting scheme as the TVD* scheme in the rest of the work.

The TVD* scheme however can lead to significant errors after long time-integration times [24, 23]. It can work well if for half the realizations $Y_i < 0$ and for the other half $Y_i > 0$. However, this is not always guaranteed. One solution could be to carry out an averaged-upwinding according to the PDF of Y_i but this would still not help us in achieving consistency. In this work, we will utilize linear centered advection schemes which ensure consistency between advection in the DO and MC setting. They have already been applied to the stochastic tracer advection equation in [23, 24]. Here, we extend their application to the unsteady stochastic DO Navier-Stokes equations.

However, it is well known that centered advection schemes introduce numerical spurious oscillations which need to be removed so as to not corrupt the solution to the dynamical equations. This is accomplished by implementing spatial filters [48, 56] which are discussed in the next section.

In addition to ensuring stability through filtering, stability and high-order accuracy of the DO solution can be ensured by adopting higher order time marching schemes. In prior numerical studies [95, 124], a first order implicit-explicit (IMEX) scheme was used. Disadvantages of using lower-order time-marching schemes in-

clude sacrificing stability and accuracy but particularly the loss of coupling between the mean and modal evolution equations over the time-step. While linear multi-step IMEX schemes can be used to tackle the former problems, IMEX Runge-Kutta schemes can be used to tackle all of these problems. We thus develop and discuss IMEX schemes for DO equations in section 2.3.

The resulting aggregate IMEX scheme for the mean and mode of velocity will include pressure gradient terms. In our system of equations for incompressible flow (eq. (2.14)), there is no evolution equation for pressure. One approach to resolve this is to consider that the flow is weakly compressible and introduce an equation of state. Other approaches [26] such as the pressure-correction methods (e.g. SIMPLE, SIMPLER, PISO, etc.) rely on decoupling pressure and velocity, e.g. [2]. Here, we use projection methods [32].

Another consequence of using numerical discretizations of the DO equations is that the DO modes are guaranteed to be orthonormal only up to numerical error. Using high-order numerical schemes helps in ensuring that the error is low over one time-step but the modes may become very far from being orthonormal over a large number of time-steps. It thus becomes important to come up with an approach to ensure orthonormality of the DO modes during time-integration and this will be discussed in section 2.4.

In order to track the true Monte Carlo realizations perfectly using the DO methodology, it would be necessary to retain all the modes in eq. (2.4) (possibly infinite) and evolve them through time. In this case, the DO methodology would become as expensive as the MC approach. This is why truncating the number of DO modes to $n_s(t)$ allows us to approximate the MC solution well and at the same time gain large computational dividends. However, in order to ascertain the influence of the truncated modes (i.e. modes numbered $n_s(t) + 1$ to ∞) on the retained modes and to increase the overall accuracy and stability of the DO framework, a closure scheme is required to model the evolution of these truncated out modes and their influence on the dynamics of the retained modes. This forms both a modeling and numerical challenge. We do not investigate this problem here and leave it for future work.

2.2 Treatment of Advection: Numerical Filtering

In general, the following properties of the filter applied is desired [48, 103]:

1. completely remove waves of wavelength $2\Delta x$ (waves of smallest wavelength that can be resolved on a grid of uniform spacing Δx in any direction)

2. preserve physically meaningful waves of higher wavelengths

3. the filter is linear so that the filtering of the DO solution is equivalent to the filtering of the realizations reconstructed from the DO solution

4. minimizes the loss of conservation properties upon application such as conservation of mass

While there a variety of numerical filters [48, 88, 87, 104], many of them are implicit or nonlinear. We focus on the linear explicit Shapiro filter [101, 102, 103] which satisfies the above properties. It is a linear symmetrical operator which uses neighboring grid points for smoothing. In one dimension, the application of Shapiro filter of order $2n$ to a field of ϕ results in the filtered values $\mathcal{F}^{2n}(\phi_i)$ as follows:

$$\mathcal{F}^{2n}(\phi_i) = \phi_i + (-1)^{n-1}\frac{\delta^{2n}}{2^{2n}}\phi_i \qquad (2.32)$$

where $\delta^2\phi_i = \phi_{i+1} - 2\phi_i + \phi_{i-1}$. This corresponds to adding high-order linear diffusion of order $2n$

$$\mathcal{F}^{2n}(\phi) = \phi + (-1)^{n-1}\frac{\Delta x^{2n}}{2^{2n}}\frac{\partial^{2n}\phi}{\partial x^{2n}} + O(\Delta x^{2n+2}) \qquad (2.33)$$

The corresponding response function or effect of applying the Shapiro filter to waves of wave number k or wavelength λ on a 1D grid of uniform spacing Δx is

$$R_n(k) = 1 - \sin^{2n}\left(k\frac{\Delta x}{2}\right) = 1 - \sin^{2n}\left(\pi\frac{\Delta x}{\lambda}\right) \qquad (2.34)$$

From the above expression, it is clear that the second order Shapiro filter completely removes waves of wavelength $2\Delta x$ but also damps waves of higher wavelengths which is not desired. This is also illustrated in Fig. 2-1. In order to avoid this, one can

apply a higher order Shapiro filter and/or apply the Shapiro filter every few number of time-steps during time-marching. Using a higher order Shapiro filter increases the width of the numerical stencil and thereby the computational cost. In the case of two or three dimensional grids, one can take two approaches: (i) apply the 1D Shapiro filter in each direction or (ii) apply mutli-dimensional Shapiro filters [21].

So far, our discussion of the Shapiro filter assumed that we were deep in the interior where there isn't a limitation on how wide the numerical stencil can be. This is no longer true near boundaries. One approach is to introduce ghost cells [101, 22] so as to use the standard centered Shapiro filter. However, this involves extrapolating values from the interior to the ghost cells while respecting boundary conditions. This introduces noisy values into the ghost cells and thus degrades the overall smoothing. Another approach is to reduce the order of the Shapiro filter which requires a smaller stencil [22, 83]. While this is robust and easy to implement, this may lead to severe damping of physically relevant waves propagating from the boundaries and hence corrupting the solution.

Another approach is to use high order decentered Shapiro filters [27, 22] where the numerical stencil is decentered by b points. This however introduces dispersion and may be anti-dissipative for high values of decentering (b). In order to obtain better dispersion and dissipation behavior, [11] and [129] suggested alternate explicit and implicit generalized decentered Shapiro filters respectively. A more effective solution is the uneven-order decentered Shapiro filters [22] which does not suffer from any instability attributed to anti-dissipative behavior. In one dimension, if the boundary cell is on the left, the expression for the filtered values $\mathcal{F}^{2n+1}(\phi_i)$ upon application of the Shapiro filter to ϕ is given by

$$\mathcal{F}^{2n+1}(\phi_i) = \phi_i + (-1)^n \frac{\delta^{2n}}{2^{2n+1}}(\phi_{i+1} - \phi_i)$$ (2.35)

The corresponding response function is

$$R_{2n+1}(k) = 1 - \sin^{2n+2}\left(k\frac{\Delta x}{2}\right) + i\cos\left(k\frac{\Delta x}{2}\right)\sin^{2n+2}\left(k\frac{\Delta x}{2}\right)$$ (2.36)

31

which corresponds to a high order diffusion term and a low order dispersion term. The response function for different orders against wavelength is plotted in Fig.2-2. As in the case of the standard centered Shapiro filter, it is desirable to use the highest possible decentered Shapiro filter in order to preserve the waves of longer wavelengths. This also helps in minimizing the amount of dispersion introduced.

The different parameters of the Shapiro filter are: (i) order of accuracy ($2n$), (ii) number of applications at a given time-step (n_{times}) and (iii) frequency at which the Shapiro filter is applied during time-marching (n_{freq}). There is no general principle in deciding these parameters. They may change from one application to another. When describing the Shapiro filter parameters in the rest of the work, we will use the minimized notation of ($2n, n_{\text{freq}}, n_{\text{times}}$).
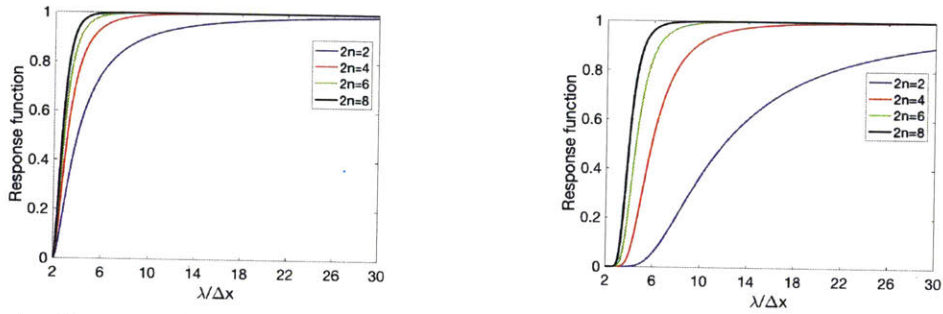
(a) Application of Shapiro Filter 1 Time   (b) Application of Shapiro Filter 100 times

Figure 2-1: Response function of the standard centered Shapiro Filter used in the interior considering 1D grid of uniform spacing Δx (Adapted from [48])
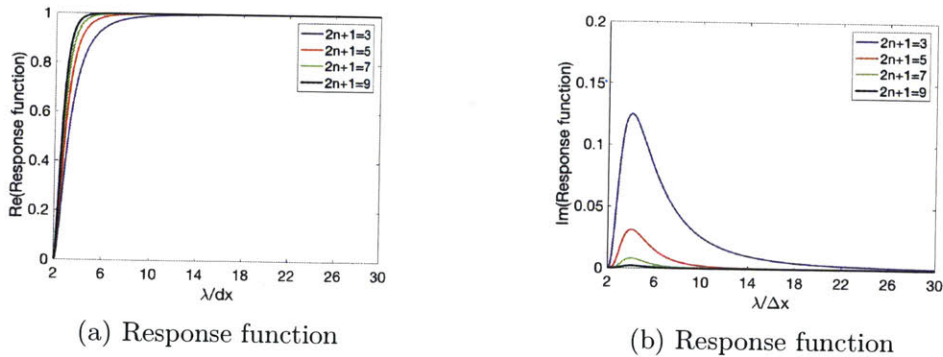
(a) Response function   (b) Response function

Figure 2-2: Response function of the un-even decentered Shapiro Filter used near boundaries considering 1D grid of uniform spacing Δx

2.3 Implicit-Explicit (IMEX) Schemes

The equations for the mean and mode in the stochastic DO Navier-Stokes equations are of the form

$$\frac{\partial \phi}{\partial t} = \mathbf{F}^{ex} + \mathbf{F}^{im} - \nabla \hat{p} \tag{2.37}$$

where $\mathbf{F}^{ex}$ are nonlinear terms such as advection which we want to evaluate explicitly, $\mathbf{F}^{im}$ are stiff terms such as diffusion which we want to evaluate implicitly and $\nabla \hat{p}$ is the gradient of mean or mode of pressure which is usually evaluated in a similar manner to the diffusion like terms. There are two categories of IMEX schemes: (i) linear multi-step IMEX schemes where information from previous timesteps is used in time-marching and (ii) IMEX Runge-Kutta schemes where one time-step is divided into multiple stages. In this section, we will describe how these IMEX schemes can be applied to the stochastic DO Navier-Stokes equations. Further, we will describe how projection methods may be used to decouple pressure and velocity.

To simplify our upcoming discussion on the application of IMEX schemes to the stochastic DO Navier-Stokes equations, we will introduce some notation here. The governing equations for the mean, modes and coefficients of velocity can be alternatively written as

$$\begin{cases} \dfrac{\partial \bar{\mathbf{u}}}{\partial t} = \mathbf{F}^{im}_{\bar{\mathbf{u}}} + \mathbf{F}^{ex}_{\bar{\mathbf{u}}} - \nabla \bar{p} \\[2mm] \dfrac{\partial \tilde{\mathbf{u}}_i}{\partial t} = \mathbf{F}^{im}_{\tilde{\mathbf{u}}_i} + \mathbf{F}^{ex}_{\tilde{\mathbf{u}}_i} - \nabla \tilde{p}_i \\[2mm] \dfrac{dY_i}{dt} = F^{ex}_{Y_i} \end{cases} \tag{2.38}$$

where the superscript of the $\mathbf{F}$ term indicates if is to be evaluated explicitly or implicitly numerically, and the subscript denotes if the term contributes to the evolution of mean, mode or coefficients. For the stochastic DO Navier-Stokes equations, these terms are as follows

$$\begin{cases} \mathbf{F}^{im}_{\bar{\mathbf{u}}} = \nu \nabla^2 \bar{\mathbf{u}} \\[2mm] \mathbf{F}^{ex}_{\bar{\mathbf{u}}} = -\nabla \cdot (\bar{\mathbf{u}}\bar{\mathbf{u}}) - \mathbb{C}_{Y_i Y_j} \nabla \cdot (\tilde{\mathbf{u}}_j \tilde{\mathbf{u}}_i) \end{cases} \tag{2.39}$$

33

$$
\begin{cases}
\mathbf{F}^{im}_{\tilde{\mathbf{u}}_i} = \nu\nabla^2\tilde{\mathbf{u}}_i \\
\mathbf{F}^{ex}_{\tilde{\mathbf{u}}_i} = -\nabla\cdot(\bar{\mathbf{u}}\tilde{\mathbf{u}}_i) - \nabla\cdot(\tilde{\mathbf{u}}_i\bar{\mathbf{u}}) - \mathbb{C}^{-1}_{Y_iY_j}\mathbb{M}_{Y_jY_mY_n}\nabla\cdot(\tilde{\mathbf{u}}_n\tilde{\mathbf{u}}_m) - \langle\mathbf{Q}_i,\tilde{\mathbf{u}}_j\rangle\tilde{\mathbf{u}}_j
\end{cases}
\qquad (2.40)
$$

where $\mathbf{Q}_i$ is as defined in eq. (2.24). This is to ensure that the diffusion terms are solved implicitly and the advection terms or inner product terms are computed explicitly. This approach is also followed in [124]. The evolution of the coefficients is computed explicitly and thus $F^{ex}_{Y_i}$ corresponds to the entire right hand side in eq. (2.29).

2.3.1 Linear Multi-step IMEX Schemes

The general linear multi-step IMEX scheme applied to the stochastic DO Navier-Stokes equations can be written in the form

$$
\begin{cases}
\dfrac{1}{m\Delta t}\bar{\mathbf{u}}^{k+1} + \dfrac{1}{\Delta t}\sum_{j=0}^{s-1}a_j\bar{\mathbf{u}}^{k-j} = -\sum_{j=0}^{s-1}b_j\{\mathbf{F}^{ex}_{\bar{\mathbf{u}}}\}^{k-j} + \sum_{j=-1}^{s-1}c_j\left[\{\mathbf{F}^{im}_{\bar{\mathbf{u}}}\}^{k-j} + \{-\nabla\bar{p}\}^{s-j}\right] \\[2ex]
\dfrac{1}{m\Delta t}\tilde{\mathbf{u}}^{k+1}_i + \dfrac{1}{\Delta t}\sum_{j=0}^{s-1}a_j\tilde{\mathbf{u}}^{k-j}_i = -\sum_{j=0}^{s-1}b_j\{\mathbf{F}^{ex}_{\tilde{\mathbf{u}}_i}\}^{k-j} + \sum_{j=-1}^{s-1}c_j\left[\{\mathbf{F}^{im}_{\tilde{\mathbf{u}}_i}\}^{k-j} + \{-\nabla\tilde{p}_i\}^{s-j}\right] \\[2ex]
\dfrac{1}{m\Delta t}Y^{k+1}_i + \dfrac{1}{\Delta t}\sum_{j=0}^{s-1}a_jY^{k-j}_i = -\sum_{j=0}^{s-1}b_j\{F^{ex}_{Y_i}\}^{k-j}
\end{cases}
$$

$$(2.41)$$

with boundary conditions as given in eq. (2.22) and eq. (2.27). The parameter s in the above equation represents the number of prior timesteps from which data needs to be stored. The superscript on the terms $\mathbf{F}^{im}$ and $\mathbf{F}^{ex}$ indicate the time-step from which these terms are being used with respect to the current time-step (i.e. k). The values of parameters a_j, b_j and c_j for which the above IMEX scheme is consistent and of order s can be found in [9]. The above scheme can be rewritten as a parametric family of schemes of order s (c.f. [9]). We want our projection method [32] to obtain the above aggregate scheme. The projection method with incremental pressure correction in rotational form can be written as

Projection scheme for the mean

$$\frac{\hat{\bar{\mathbf{u}}}^{k+1}}{m\Delta t} - c_{-1}\{\mathbf{F}_{\hat{\bar{\mathbf{u}}}}^{im}\}^{k+1} = \left(\frac{\mathbf{I}}{m\Delta t} - c_{-1}\nu\nabla^2\right)\hat{\bar{\mathbf{u}}}^{k+1}$$

$$= -\frac{1}{\Delta t}\sum_{j=0}^{s-1}a_j\mathbf{u}^{k-j} - \sum_{j=0}^{s-1}b_j\{\mathbf{F}_{\bar{\mathbf{u}}}^{ex}\}^{k-j} + \sum_{j=0}^{s-1}c_j\{\mathbf{F}_{\bar{\mathbf{u}}}^{im}\}^{k-j} - \nabla\bar{p}^k$$

$$(2.42\text{a})$$

$$\frac{\nabla\cdot\hat{\bar{\mathbf{u}}}^{k+1}}{m\Delta t} = \nabla^2\bar{q}^k \tag{2.42b}$$

$$\bar{\mathbf{u}}^{k+1} = \hat{\bar{\mathbf{u}}}^{k+1} - m\Delta t\nabla\bar{q}^k \tag{2.42c}$$

$$\bar{p}^{k+1} = \frac{\bar{q}^k}{c_{-1}} + \frac{1+c_0}{c_{-1}}\bar{p}^k - \sum_{j=1}^{s-1}\bar{p}^{k-j} - \nu\nabla\cdot\hat{\bar{\mathbf{u}}}^{k+1} \tag{2.42d}$$

with boundary conditions

$$\begin{cases} \hat{\bar{\mathbf{u}}}^{k+1} = \bar{\mathbf{h}}_D, & \dfrac{\partial\bar{q}}{\partial\mathbf{n}} = 0, \quad \mathbf{r}\in\partial\mathcal{D}_D \\[2mm] \dfrac{\partial\hat{\bar{\mathbf{u}}}^{k+1}}{\partial\mathbf{n}} = \bar{\mathbf{h}}_N, & \mathbf{r}\in\partial\mathcal{D}_N \end{cases} \tag{2.43}$$

where $\hat{\bar{\mathbf{u}}}^{k+1}$ is the predicted mean velocity, and $\bar{\mathbf{u}}^{k+1}$ is the corrected mean velocity which is also considered to be the mean velocity at time t_{k+1}. Eq. (2.42a) corresponds to the prediction step, eq. (2.42b) to the Poisson equation solve, eq. (2.42c) to the velocity update, and eq. (2.42d) to the pressure update. The last three equations collectively form the correction step.

Projection scheme for the modes

$$\frac{\hat{\tilde{\mathbf{u}}}_i^{k+1}}{m\Delta t} - c_{-1}\{\mathbf{F}_{\hat{\tilde{\mathbf{u}}}_i}^{im}\}^{k+1} = \left(\frac{\mathbf{I}}{m\Delta t} - c_{-1}\nu\nabla^2\right)\hat{\tilde{\mathbf{u}}}_i^{k+1}$$

$$= -\frac{1}{\Delta t}\sum_{j=0}^{s-1}a_j\tilde{\mathbf{u}}_i^{k-j} - \sum_{j=0}^{s-1}b_j\{\mathbf{F}_{\tilde{\mathbf{u}}_i}^{ex}\}^{k-j} + \sum_{j=0}^{s-1}c_j\{\mathbf{F}_{\tilde{\mathbf{u}}_i}^{im}\}^{k-j} - \nabla\tilde{p}_i^k$$

$$(2.44\text{a})$$

$$\frac{\nabla \cdot \hat{\tilde{\mathbf{u}}}_i^{k+1}}{m\Delta t} = \nabla^2 \tilde{q}_i^k \tag{2.44b}$$

$$\tilde{\mathbf{u}}_i^{k+1} = \hat{\tilde{\mathbf{u}}}_i^{k+1} - m\Delta t \nabla \tilde{q}_i^k \tag{2.44c}$$

$$\tilde{p}_i^{k+1} = \frac{\tilde{q}_i^k}{c_{-1}} + \frac{1+c_0}{c_{-1}}\tilde{p}_i^k - \sum_{j=1}^{s-1}\tilde{p}_i^{k-j} - \nu\nabla \cdot \hat{\tilde{\mathbf{u}}}_i^{k+1} \tag{2.44d}$$

with boundary conditions

$$\begin{cases} \hat{\tilde{\mathbf{u}}}_i^{k+1} = \tilde{\mathbf{h}}_{i,D}, & \dfrac{\partial \tilde{q}_i}{\partial \mathbf{n}} = 0, \quad \mathbf{r} \in \partial\mathcal{D}_D \\[4mm] \dfrac{\partial \hat{\tilde{\mathbf{u}}}_i^{k+1}}{\partial \mathbf{n}} = \tilde{\mathbf{h}}_{i,N}, & \mathbf{r} \in \partial\mathcal{D}_N \end{cases} \tag{2.45}$$

where $\hat{\tilde{\mathbf{u}}}_i^{k+1}$ is the predicted velocity for mode i, and $\tilde{\mathbf{u}}_i^{k+1}$ is the corrected velocity for mode i which is also considered to be the modal velocity at time t_{k+1}.

Summary of the complete time-integration scheme from time t_k to t_{k+1} is given in Algorithm 1. Details of how $\mathbb{C}_{Y_i Y_j}$ is computed when the covariance matrix is close to singular is discussed in [124]. Reorthonormalization and selection of the time-step size will be discussed in section 2.4. Algorithm 1 describes the time-integration followed after the starting time because second and higher order linear multi-step IMEX schemes require special starting. For example, the third-order IMEX Semi-implicit Backward Difference (IMEX-SBDF3) is typically started by one step of IMEX-SBDF1 followed by one step of IMEX-SBDF2. These schemes are described in Table 2.1. This is another motivation to look at IMEX Runge-Kutta (IMEX-RK) schemes which do not require any special starting. This is discussed in the next section.

2.3.2 IMEX Runge-Kutta Schemes

We closely follow the notation in [123] for the following discussion on IMEX-RK schemes. An implicit scheme with s_{im} stages is combined with a compatible explicit scheme with s_{ex} stages to obtain consistent IMEX-RK schemes [8] of order s_{imex} ($\leq s_{im}$). We consider IMEX-RK schemes [123] which have Butcher Tableaus of the

Algorithm 1 Linear Multi-step IMEX Time-Integration for Stochastic DO Navier-Stokes Equations

Input: $\bar{\mathbf{u}}^k \in \mathbb{R}^{(N_u+N_v)\times 1}$, $\tilde{\mathbf{u}}_i^k \in \mathbb{R}^{(N_u+N_v)\times n_s}$, $\bar{p}^k \in \mathbb{R}^{N_p\times 1}$, $\tilde{p}_i^k \in \mathbb{R}^{N_p\times n_s}$, Y_i^k, k, Δt, $2n$, n_{times}, n_{freq}

Output: $\bar{\mathbf{u}}^{k+1} \in \mathbb{R}^{(N_u+N_v)\times 1}$, $\tilde{\mathbf{u}}_i^{k+1} \in \mathbb{R}^{(N_u+N_v)\times n_s}$, $\bar{p}^{k+1} \in \mathbb{R}^{N_p\times 1}$, $\tilde{p}_i^{k+1} \in \mathbb{R}^{N_p\times n_s}$, Y_i^{k+1}

1: **procedure** TIME-INTEGRATION(Inputs)
2:     Compute statistics $\{\mathbb{C}_{Y_iY_j}\}^k$ (and it's inverse), $\{\mathbb{M}_{Y_jY_mY_n}\}^k$
3:     Compute explicit terms (advection and inner product terms) $\{\mathbf{F}_{\bar{\mathbf{u}}}^{ex}\}^k$ and $\{\mathbf{F}_{\tilde{\mathbf{u}}_i}^{ex}\}^k$
4:     Obtain Y_i^{k+1} using eq. (2.41)
5:     Obtain $\bar{\mathbf{u}}^{k+1}$ and $\bar{p}^{k+1}$ using eq. (2.42)
6:     Obtain $\tilde{\mathbf{u}}_i^{k+1}$ and $\tilde{p}_i^{k+1}$ using eq. (2.44)
7:     **if** $(k \bmod n_{\text{freq}}) == 0$ **then**
8:         Perform shapiro filtering
9:     **end if**
10:    Re-orthonormalize modes $\tilde{\mathbf{u}}_i^{k+1}$ and $\tilde{p}_i^{k+1}$
11:    **return** Outputs
12: **end procedure**

Name	$\mathcal{O}$	Scheme
Crank-Nicholson Leapfrog (CNLF)	2	$\dfrac{\phi^{k+1} - \phi^{k-1}}{2\Delta t} = \{\mathbf{F}^{ex}\}^k + \dfrac{1}{2}\left[\{\mathbf{F}^{im}\}^{k+1} + \{\mathbf{F}^{im}\}^{k-1}\right]$ $- \dfrac{1}{2}\left[\nabla p^{k+1} + \nabla p^{k-1}\right]$
Semi-Implicit Backward Difference 2nd order (SBDF2)	2	$\dfrac{3\phi^{k+1} - 4\phi^k + \phi^{k-1}}{2\Delta t} = 2\{\mathbf{F}^{ex}\}^k - \{\mathbf{F}^{ex}\}^{k-1}$ $+ \{\mathbf{F}^{im}\}^{k+1} - \nabla p^{k+1}$
Crank-Nicholson Adams-Bashforth 2nd order (CNAB2)	2	$\dfrac{\phi^{k+1} - \phi^{k-1}}{2\Delta t} = \dfrac{3}{2}\{\mathbf{F}^{ex}\}^k - \dfrac{1}{2}\{\mathbf{F}^{ex}\}^{k-1}$ $+ \dfrac{1}{2}\left[\{\mathbf{F}^{im}\}^{k+1} + \{\mathbf{F}^{im}\}^{k-1}\right] - \dfrac{1}{2}\left[\nabla p^{k+1} + \nabla p^{k-1}\right]$
Semi-Implicit Backward Difference 3rd order (SBDF3)	3	$\dfrac{1}{\Delta t}\left(\dfrac{11}{6}\phi^{k+1} - 3\phi^k + \dfrac{3}{2}\phi^{k-1} - \dfrac{1}{3}\phi^{k-2}\right) =$ $3\{\mathbf{F}^{ex}\}^k - 3\{\mathbf{F}^{ex}\}^{k-1} + \{\mathbf{F}^{ex}\}^{k-2} + \{\mathbf{F}^{im}\}^{k+1} - \nabla p^{k+1}$

Table 2.1: Examples of Linear Multi-step IMEX Schemes

form given in eq. (2.46).

$$
\begin{array}{c|cccccc}
0 & 0 & \cdots & \cdots & & 0 \\
c_1 & a^{ex}_{1,0} & 0 & \cdots & & 0 \\
\vdots & \vdots & \ddots & \ddots & & 0 \\
c_{s-1} & a^{ex}_{s-1,0} & \cdots & a^{ex}_{s-1,s-2} & & 0 \\
\hline
 & b_0 & \cdots & b_{s-2} & & a
\end{array}
\qquad
\begin{array}{c|ccccc}
0 & 0 & 0 & \cdots & \cdots & 0 \\
c_1 & a^{im}_{1,0} & a & 0 & \cdots & 0 \\
\vdots & \vdots & \ddots & \ddots & \cdots & 0 \\
c_{s-1} & a^{im}_{s-1,0} & \cdots & \cdots & a^{im}_{s-1,s-2} & a \\
\hline
 & b_0 & \cdots & \cdots & b_{s-2} & a
\end{array}
\qquad (2.46)
$$

The Butcher Tableaus for the implicit and explicit scheme are padded with zeros [8] such that they have the same number of stages i.e. s. The entries of the Butcher Tableau for the explicit scheme satisfy $a^{ex}_{\alpha,\beta} = 0 \quad \forall \beta \geq \alpha$. It can be noted from above that we limit ourselves to Diagonally Implicit Runge-Kutta (DIRK) schemes which have the property of $a^{im}_{\alpha,\beta} = 0 \quad \forall \beta > \alpha$ so that we can solve the different stages sequentially instead of simultaneously. Further considering that $a^{im}_{\alpha,\alpha} = a \quad \forall 1 < \alpha < s$ i.e. all the diagonal entries are same allow us to create a single matrix for the implicit solve. Additionally, we also prefer schemes with $b_\alpha = b^{ex}_\alpha = b^{im}_\alpha$.

The IMEX-RK scheme applied to the stochastic DO Navier-Stokes equations then can be written as

$$
\begin{cases}
\bar{\mathbf{u}}^{k+1} = \bar{\mathbf{u}}^k + \Delta t \displaystyle\sum_{\alpha=0}^{s-1} b^{ex}_\alpha \{\mathbf{F}^{ex}_{\bar{\mathbf{u}}}\}^\alpha + \Delta t \sum_{\alpha=0}^{s-1} b^{im}_\alpha \left[\{\mathbf{F}^{im}_{\bar{\mathbf{u}}}\}^\alpha + \{-\nabla \bar{p}\}^\alpha \right] \\[2mm]
\tilde{\mathbf{u}}_i^{k+1} = \tilde{\mathbf{u}}_i^k + \Delta t \displaystyle\sum_{\alpha=0}^{s-1} b^{ex}_\alpha \{\mathbf{F}^{ex}_{\tilde{\mathbf{u}}_i}\}^\alpha + \Delta t \sum_{\alpha=0}^{s-1} b^{im}_\alpha \left[\{\mathbf{F}^{im}_{\tilde{\mathbf{u}}_i}\}^\alpha + \{-\nabla \tilde{p}_i\}^\alpha \right] \\[2mm]
Y_i^{k+1} = Y_i^k + \Delta t \displaystyle\sum_{\alpha=0}^{s-1} b^{ex}_\alpha \{F^{ex}_{Y_i}\}^\alpha
\end{cases}
\qquad (2.47)
$$

where s is the number of stages. The superscript on the terms $\mathbf{F}^{im}$ and $\mathbf{F}^{ex}$ indicate the stage from which these terms are being used.

The intermediate variables of mean $\bar{\mathbf{u}}^\alpha$, modes $\tilde{\mathbf{u}}_i^\alpha$, and coefficients Y_i^α in stage α

are then solved using

$$
\begin{cases}
\bar{\mathbf{u}}^\alpha = \bar{\mathbf{u}}^k + \Delta t \sum_{\beta=0}^{\alpha-1} a_{\alpha,\beta}^{ex} \{\mathbf{F}_{\bar{\mathbf{u}}}^{ex}\}^\beta + \Delta t \sum_{\beta=0}^{\alpha} a_{\alpha,\beta}^{im} \left[\{\mathbf{F}_{\bar{\mathbf{u}}}^{im}\}^\beta + \{-\nabla \bar{p}\}^\beta \right] \\[2ex]
\tilde{\mathbf{u}}_i^\alpha = \tilde{\mathbf{u}}_i^k + \Delta t \sum_{\beta=0}^{\alpha-1} a_{\alpha,\beta}^{ex} \{\mathbf{F}_{\tilde{\mathbf{u}}_i}^{ex}\}^\beta + \Delta t \sum_{\beta=0}^{\alpha} a_{\alpha,\beta}^{im} \left[\{\mathbf{F}_{\tilde{\mathbf{u}}_i}^{im}\}^\beta + \{-\nabla \tilde{p}_i\}^\beta \right] \\[2ex]
Y_i^\alpha = Y_i^k + \Delta t \sum_{\beta=0}^{\alpha-1} a_{\alpha,\beta}^{ex} \{F_{Y_i}^{ex}\}^\beta
\end{cases}
\tag{2.48}
$$

The above aggregate schemes for the mean and mode are then solved using projection methods as discussed before. The following discussion closely follows the layout in [123].

Projection scheme for mean in stage α

$$
\frac{\hat{\bar{\mathbf{u}}}^\alpha}{\Delta t} - a_{\alpha,\alpha}^{im} \{\mathbf{F}_{\hat{\bar{\mathbf{u}}}}^{im}\}^\alpha = \left(\frac{\mathbf{I}}{\Delta t} - a_{\alpha,\alpha} \nu \nabla^2 \right) \hat{\bar{\mathbf{u}}}^\alpha
$$
$$
= \frac{\bar{\mathbf{u}}^k}{\Delta t} + \sum_{\beta=0}^{\alpha-1} a_{\alpha,\beta}^{ex} \{\mathbf{F}_{\bar{\mathbf{u}}}^{ex}\}^\beta
$$
$$
+ \sum_{\beta=0}^{\alpha-1} a_{\alpha,\beta}^{im} \left[\{\mathbf{F}_{\bar{\mathbf{u}}}^{im}\}^\beta + \{-\nabla \bar{p}\}^\beta \right] - a_{\alpha,\alpha}^{im} \nabla \bar{p}^{\alpha\star}
\tag{2.49a}
$$

$$
\frac{\nabla \cdot \hat{\bar{\mathbf{u}}}^\alpha}{a_{\alpha,\alpha}^{im} \Delta t} = \nabla^2 \bar{q}^\alpha
\tag{2.49b}
$$

$$
\bar{\mathbf{u}}^\alpha = \hat{\bar{\mathbf{u}}}^\alpha - a_{\alpha,\alpha}^{im} \Delta t \nabla \bar{q}^\alpha
\tag{2.49c}
$$

$$
\bar{p}^\alpha = \bar{p}^{\alpha\star} + \bar{q}^\alpha - \nu \nabla \cdot \hat{\bar{\mathbf{u}}}^\alpha
\tag{2.49d}
$$

with boundary conditions

$$
\begin{cases}
\hat{\bar{\mathbf{u}}}^\alpha = \bar{\mathbf{h}}_D, \quad \dfrac{\partial \bar{q}^\alpha}{\partial \mathbf{n}} = 0, \quad \mathbf{r} \in \partial \mathcal{D}_D \\[2ex]
\dfrac{\partial \hat{\bar{\mathbf{u}}}^\alpha}{\partial \mathbf{n}} = \bar{\mathbf{h}}_N, \quad \mathbf{r} \in \partial \mathcal{D}_N
\end{cases}
\tag{2.50}
$$

where $\hat{\bar{\mathbf{u}}}^{\alpha}$ is the predicted mean velocity for stage α, and $\bar{\mathbf{u}}^{\alpha}$ is the corrected mean velocity which is also considered to be the mean velocity at stage α. The variable $\bar{p}^{\alpha\star}$ is the estimated pressure at stage α which is usually a function of previously calculated pressures at different stages. For the projection method with incremental pressure correction in rotational form, it is considered to be the pressure from end of the previous stage i.e. at end of stage $(\alpha - 1)$. Eq. (2.49a) corresponds to the prediction step, eq. (2.49b) to the Poisson equation solve, eq. 2.49c to the velocity update, and eq. 2.49d to the pressure update within the stage. The last three equations collectively form the correction step.

After the updated mean velocity and pressure at the end of stage α are computed, the implicit predicted diffusion term of $\{\mathbf{F}_{\hat{\bar{\mathbf{u}}}}^{im}\}^{\alpha}$ must be replaced by the implicit corrected diffusion term $\{\mathbf{F}_{\bar{\mathbf{u}}}^{im}\}^{\alpha}$. This can be done by recomputing these terms with the corrected values of mean velocity and pressure. Another equivalent approach is from the aggregate scheme at stage α given by eq. (2.48).

$$\{\mathbf{F}_{\bar{\mathbf{u}}}^{im}\}^{\alpha} = \frac{\bar{\mathbf{u}}^{\alpha} - \bar{\mathbf{u}}^{k}}{a_{\alpha,\alpha}^{im}\Delta t} - \frac{1}{a_{\alpha,\alpha}^{im}} \left[\sum_{\beta=0}^{\alpha-1} a_{\alpha,\beta}^{ex}\{\mathbf{F}_{\bar{\mathbf{u}}}^{ex}\}^{\beta} + \sum_{\beta=0}^{\alpha-1} a_{\alpha,\beta}^{im}\{\mathbf{F}_{\bar{\mathbf{u}}}^{im}\}^{\beta} - \sum_{\beta=0}^{\alpha} a_{\alpha,\beta}^{im}\{\nabla\bar{p}\}^{\beta} \right]$$

$$(2.51)$$

Projection scheme for modes in stage α

$$\frac{\hat{\tilde{\mathbf{u}}}_{i}^{\alpha}}{\Delta t} - a_{\alpha,\alpha}^{im}\{\mathbf{F}_{\hat{\mathbf{u}}_i}^{im}\}^{\alpha} = \left(\frac{\mathbf{I}}{\Delta t} - a_{\alpha,\alpha}\nu\nabla^2 \right) \hat{\tilde{\mathbf{u}}}_{i}^{\alpha}$$

$$= \frac{\tilde{\mathbf{u}}_{i}^{k}}{\Delta t} + \sum_{\beta=0}^{\alpha-1} a_{\alpha,\beta}^{ex}\{\mathbf{F}_{\tilde{\mathbf{u}}_i}^{ex}\}^{\beta}$$

$$+ \sum_{\beta=0}^{\alpha-1} a_{\alpha,\beta}^{im} \left[\{\mathbf{F}_{\tilde{\mathbf{u}}_i}^{im}\}^{\beta} + \{-\nabla\tilde{p}_i\}^{\beta} \right] - a_{\alpha,\alpha}^{im}\nabla\tilde{p}_i^{\alpha\star} \qquad (2.52a)$$

$$\frac{\nabla \cdot \hat{\tilde{\mathbf{u}}}_{i}^{\alpha}}{a_{\alpha,\alpha}^{im}\Delta t} = \nabla^2\tilde{q}_{i}^{\alpha} \qquad (2.52b)$$

$$\tilde{\mathbf{u}}_{i}^{\alpha} = \hat{\tilde{\mathbf{u}}}_{i}^{\alpha} - a_{\alpha,\alpha}^{im}\Delta t\nabla\tilde{q}_{i}^{\alpha} \qquad (2.52c)$$

$$\tilde{p}_{i}^{\alpha} = \tilde{p}_{i}^{\alpha\star} + \tilde{q}_{i}^{\alpha} - \nu\nabla \cdot \hat{\tilde{\mathbf{u}}}_{i}^{\alpha} \qquad (2.52d)$$

with boundary conditions

$$
\begin{cases}
\hat{\tilde{\mathbf{u}}}_i^\alpha = \tilde{\mathbf{h}}_{i,D}, \quad \dfrac{\partial \tilde{q}_i^\alpha}{\partial \mathbf{n}} = 0, \quad \mathbf{r} \in \partial \mathcal{D}_D \\[4mm]
\dfrac{\partial \hat{\tilde{\mathbf{u}}}_i^\alpha}{\partial \mathbf{n}} = \tilde{\mathbf{h}}_{i,N}, \quad \mathbf{r} \in \partial \mathcal{D}_N
\end{cases}
\tag{2.53}
$$

where $\hat{\tilde{\mathbf{u}}}_i^\alpha$ is the predicted velocity of mode i for stage α, and $\tilde{\mathbf{u}}_i^\alpha$ is the corrected modal velocity which is also considered to be the modal velocity at stage α. The variable $\tilde{p}_i^{\alpha\star}$ is the estimated modal pressure at stage α which is usually a function of previously calculated modal pressures at different stages. For the projection method with incremental pressure correction in rotational form, it is considered to be the modal pressure from end of the previous stage i.e. at end of stage $(\alpha - 1)$. Eq. (2.52a) corresponds to the prediction step, eq. (2.52b) to the Poisson equation solve, eq. (2.52c) to the velocity update, and eq. (2.52d) to the modal pressure update within the stage. The last three equations collectively form the correction step.

After the updated velocity and pressure of mode i at the end of stage α are computed, the implicit predicted modal diffusion term of $\{\mathbf{F}_{\hat{\tilde{\mathbf{u}}}_i}^{im}\}^\alpha$ must be replaced by the implicit corrected modal diffusion term $\{\mathbf{F}_{\tilde{\mathbf{u}}_i}^{im}\}^\alpha$. This can be done by recomputing these terms with the corrected values of velocity and pressure of mode i. Another equivalent approach is from the aggregate scheme at stage α given by eq. (2.48).

$$
\{\mathbf{F}_{\tilde{\mathbf{u}}_i}^{im}\}^\alpha = \frac{\tilde{\mathbf{u}}_i^\alpha - \tilde{\mathbf{u}}_i^k}{a_{\alpha,\alpha}^{im}\Delta t} - \frac{1}{a_{\alpha,\alpha}^{im}}\left[\sum_{\beta=0}^{\alpha-1} a_{\alpha,\beta}^{ex}\{\mathbf{F}_{\tilde{\mathbf{u}}_i}^{ex}\}^\beta + \sum_{\beta=0}^{\alpha-1} a_{\alpha,\beta}^{im}\{\mathbf{F}_{\tilde{\mathbf{u}}_i}^{im}\}^\beta - \sum_{\beta=0}^{\alpha} a_{\alpha,\beta}^{im}\{\nabla\tilde{p}_i\}^\beta\right]
\tag{2.54}
$$

After all the stages are complete, the updated fields of the mean and modes of velocity at time t_{k+1} can be obtained from combining the mean and modal values of velocity from the different stages using eq. (2.47). However, this requires computing the explicit terms of $\{\mathbf{F}_{\bar{\mathbf{u}}}^{ex}\}^{s-1}$ and $\{\mathbf{F}_{\tilde{\mathbf{u}}_i}^{ex}\}^{s-1}$. These may be divergent and thus a final projection step must be taken to update the mean pressure $\bar{p}^{s-1}$ and modal pressures $\tilde{p}_i^{s-1}$ that will ensure divergence-free $\bar{\mathbf{u}}^{k+1}$ and $\tilde{\mathbf{u}}_i^{k+1}$. Expressions for the projection method for the mean and modes of velocity in final recombination step follow.

41

Projection scheme for mean in final recombination step

$$\frac{\hat{\bar{\mathbf{u}}}^{k+1}}{\Delta t} = \frac{\bar{\mathbf{u}}^k}{\Delta t} + \sum_{\beta=0}^{s-1} b_\beta^{ex} \{\mathbf{F}_{\bar{\mathbf{u}}}^{ex}\}^\beta + \sum_{\beta=0}^{s-1} b_\beta^{im} \left[\{\mathbf{F}_{\bar{\mathbf{u}}}^{im}\}^\beta + \{-\nabla \bar{p}\}^\beta\right] \qquad (2.55\text{a})$$

$$\frac{\nabla \cdot \hat{\bar{\mathbf{u}}}^{k+1}}{b_{s-1}^{im}\Delta t} = \nabla^2 \bar{q}^{k+1} \qquad (2.55\text{b})$$

$$\bar{\mathbf{u}}^{k+1} = \hat{\bar{\mathbf{u}}}^{k+1} - b_{s-1}^{im}\Delta t \nabla \bar{q}^{k+1} \qquad (2.55\text{c})$$

$$\bar{p}^{k+1} = \bar{p}^{s-1} + \bar{q}^{k+1} \qquad (2.55\text{d})$$

with boundary conditions

$$\frac{\partial \bar{q}^{k+1}}{\partial \mathbf{n}} = 0, \quad \mathbf{r} \in \partial \mathcal{D}_D \qquad (2.56)$$

where $\hat{\bar{\mathbf{u}}}^{k+1}$ is the predicted mean velocity for time t_{k+1} and $\bar{\mathbf{u}}^{k+1}$ is the corrected mean velocity for time t_{k+1}. Boundary conditions on the predicted velocity is not required as we only need to evaluate the variable in eq. (2.55a) and not carry out any solve.

Projection scheme for modes in final recombination step

$$\frac{\hat{\tilde{\mathbf{u}}}_i^{k+1}}{\Delta t} = \frac{\tilde{\mathbf{u}}_i^k}{\Delta t} + \sum_{\beta=0}^{s-1} b_\beta^{ex} \{\mathbf{F}_{\tilde{\mathbf{u}}_i}^{ex}\}^\beta + \sum_{\beta=0}^{s-1} b_\beta^{im} \left[\{\mathbf{F}_{\tilde{\mathbf{u}}_i}^{im}\}^\beta + \{-\nabla \tilde{p}_i\}^\beta\right] \qquad (2.57\text{a})$$

$$\frac{\nabla \cdot \hat{\tilde{\mathbf{u}}}_i^{k+1}}{b_{s-1}^{im}\Delta t} = \nabla^2 \tilde{q}_i^{k+1} \qquad (2.57\text{b})$$

$$\tilde{\mathbf{u}}_i^{k+1} = \hat{\tilde{\mathbf{u}}}_i^{k+1} - b_{s-1}^{im}\Delta t \nabla \tilde{q}_i^{k+1} \qquad (2.57\text{c})$$

$$\tilde{p}_i^{k+1} = \tilde{p}_i^{s-1} + \tilde{q}_i^{k+1} \qquad (2.57\text{d})$$

with boundary conditions

$$\frac{\partial \tilde{q}_i^{k+1}}{\partial \mathbf{n}} = 0, \quad \mathbf{r} \in \partial \mathcal{D}_D \qquad (2.58)$$

where $\hat{\tilde{\mathbf{u}}}_i^{k+1}$ is the predicted velocity of mode i for time t_{k+1} and $\tilde{\mathbf{u}}_i^{k+1}$ is the corrected velocity of mode i for time t_{k+1}. Boundary conditions on the predicted modal velocity is not required as we only need to evaluate the variable in eq. (2.57a) and not carry out any solve.

The details of the IMEX-RK scheme and the corresponding projection method applied to the stochastic DO Navier-Stokes equation is now complete. A summary of the complete time-integration scheme from time t_k to t_{k+1} is given in Algorithm 2. Lines 3 to 11 describes the projection schemes and solves carried out within each stage. Lines 12 to 16 describes the final recombination step. Post time-marching, Shapiro filtering and re-orthonormalization of the modes is carried out. One could also carry out further Shapiro filtering and/or re-orthonormalization after every stage in addition to at the end of the final recombination step.

We wrote a general routine for the IMEX-RK time-integration with additional inputs of Butcher tableaus satisfying properties described before. A particular example that we consider is the 3rd order combination of a two-stage 3rd order DIRK scheme and three-stage 3rd order explicit RK scheme (eq. (2.59) where $\gamma = (3 + \sqrt{3})/6$) [8]. We refer to this as the IMEX-RK (2,3,3) scheme in the rest of this work.

$$
\begin{array}{c|ccc}
0 & 0 & 0 & 0 \\
\gamma & \gamma & 0 & 0 \\
1-\gamma & \gamma-1 & 2(1-\gamma) & 0 \\
\hline
& 0 & 1/2 & 1/2
\end{array}
\qquad
\begin{array}{c|ccc}
0 & 0 & 0 & 0 \\
\gamma & 0 & \gamma & 0 \\
1-\gamma & 0 & 1-2\gamma & \gamma \\
\hline
& 0 & 1/2 & 1/2
\end{array}
\tag{2.59}
$$

Another example that we consider is the 2nd order L-stable combination of a two-stage 2nd order stiffly accurate DIRK scheme and three-stage 3rd order explicit RK scheme (eq. (2.60) where $\gamma = (2 - \sqrt{2})/2$ and $\delta = -2\sqrt{2}/3$) [8]. This will be referred to as the IMEX-RK (2,3,2) scheme from hereon.

$$
\begin{array}{c|ccc}
0 & 0 & 0 & 0 \\
\gamma & \gamma & 0 & 0 \\
1 & \delta & 1-\delta & 0 \\
\hline
& 0 & 1-\gamma & \gamma
\end{array}
\qquad
\begin{array}{c|ccc}
0 & 0 & 0 & 0 \\
\gamma & 0 & \gamma & 0 \\
1 & 0 & 1-\gamma & \gamma \\
\hline
& 0 & 1-\gamma & \gamma
\end{array}
\tag{2.60}
$$

43

Algorithm 2 IMEX Runge-Kutta Time-Integration for Stochastic DO Navier-Stokes Equations

---

Input: $\bar{\mathbf{u}}^k \in \mathbb{R}^{(N_u+N_v)\times 1}$, $\tilde{\mathbf{u}}_i^k \in \mathbb{R}^{(N_u+N_v)\times n_s}$, $\bar{p}^k \in \mathbb{R}^{N_p\times 1}$, $\tilde{p}_i^k \in \mathbb{R}^{N_p\times n_s}$, Y_i^k, k, Δt, $2n$, n_{times}, n_{freq}

Output: $\bar{\mathbf{u}}^{k+1} \in \mathbb{R}^{(N_u+N_v)\times 1}$, $\tilde{\mathbf{u}}_i^{k+1} \in \mathbb{R}^{(N_u+N_v)\times n_s}$, $\bar{p}^{k+1} \in \mathbb{R}^{N_p\times 1}$, $\tilde{p}_i^{k+1} \in \mathbb{R}^{N_p\times n_s}$, Y_i^{k+1}

1: **procedure** TIME-INTEGRATION(Inputs)
2:     Compute the implicit terms $\{\mathbf{F}_{\bar{\mathbf{u}}}^{im}\}^0$ and $\{\mathbf{F}_{\tilde{\mathbf{u}}_i}^{im}\}^0$ using information from t_k
3:     **for** $\alpha = 1$ to $(s-1)$ **do**
4:         Update time: $t = t_k + c_\alpha \Delta t$
5:         Compute statistics $\{\mathbb{C}_{Y_i Y_j}\}^{\alpha-1}$ (and it's inverse), $\{\mathbb{M}_{Y_j Y_m Y_n}\}^{\alpha-1}$
6:         Compute explicit terms (advection and inner product terms) $\{\mathbf{F}_{\bar{\mathbf{u}}}^{ex}\}^{\alpha-1}$ and $\{\mathbf{F}_{\tilde{\mathbf{u}}_i}^{ex}\}^{\alpha-1}$
7:         Obtain Y_i^α using eq. (2.48)
8:         Obtain $\bar{\mathbf{u}}^\alpha$ and $\bar{p}^\alpha$ using eq. (2.49)
9:         Obtain $\tilde{\mathbf{u}}_i^\alpha$ and $\tilde{p}_i^\alpha$ using eq. (2.52)
10:        Compute the implicit terms $\{\mathbf{F}_{\bar{\mathbf{u}}}^{im}\}^\alpha$ and $\{\mathbf{F}_{\tilde{\mathbf{u}}_i}^{im}\}^\alpha$ using eqs. 2.51 and 2.54 respectively
11:     **end for**
12:     Compute statistics $\{\mathbb{C}_{Y_i Y_j}\}^{s-1}$ (and it's inverse), $\{\mathbb{M}_{Y_j Y_m Y_n}\}^{s-1}$
13:     Compute explicit terms (advection and inner product terms) $\{\mathbf{F}_{\bar{\mathbf{u}}}^{ex}\}^{s-1}$ and $\{\mathbf{F}_{\tilde{\mathbf{u}}_i}^{ex}\}^{s-1}$
14:     Obtain Y_i^{k+1} using eq. (2.47)
15:     Obtain $\bar{\mathbf{u}}^{k+1}$ and $\bar{p}^{k+1}$ using eq. (2.55)
16:     Obtain $\tilde{\mathbf{u}}_i^{k+1}$ and $\tilde{p}_i^{k+1}$ using eq. (2.57)
17:     **if** $(k \bmod n_{\text{freq}}) == 0$ **then**
18:         Perform shapiro filtering
19:     **end if**
20:     Reorthonormalize modes $\tilde{\mathbf{u}}_i^{k+1}$ and $\tilde{p}_i^{k+1}$
21:     **return** Outputs
22: **end procedure**

2.3.3 Comparison of IMEX Schemes

Now that we have finished the discussion on how different types of IMEX schemes may be applied to the stochastic DO Navier-Stokes questions, we need to address when is one scheme more favorable than the other. We will discuss their differences on the criteria of starting, time-stepping, coupling, computational expense, storage and stability.

As we have noted earlier, the linear multi-step IMEX schemes require special starting. As one moves to higher order time-integration schemes, a hierarchy of lower order time-integrations must be first applied. This has the negative consequence of having to use a fixed time step size and thus a prior knowledge of the magnitudes of flow to be expected in the numerical simulation. Changing the time-step requires one to perform the special starting procedures again or restart from an earlier time. This is circumvented in the IMEX Runge-Kutta schemes which are self-starting and adaptive time-stepping can be easily applied [8].

Further, IMEX-RK time-integration respects that the stochastic DO NS equations are coupled even over one time-step which is neglected in the case of linear-multistep IMEX schemes. This however comes at the increased computational cost of having to perform multiple advection evaluations and pressure poisson equation (PPE) solves. For example, a second order IMEX-RK scheme requires two advection evaluations and two PPE solves whereas an IMEX-SBDF2 scheme requires only one advection evaluation and one PPE solve. The storage requirements of linear multi-step schemes are however higher as one needs to save the save information from previous time-steps.

As advection tends to be the most expensive operation during the numerical simulation, higher order IMEX-RK schemes may become more expensive to perform for the same time-step size. However, in most cases IMEX-RK schemes may still be preferred because of their broad stability regions. Higher order linear multi-step IMEX schemes have much smaller stability regions [9].

2.4 Re-orthonormalization and Time-stepping

We initialize the modes using the KL decomposition of eq. (2.4). The modes are then orthonormal with respect to the spatial inner product defined in eq. (2.6). Analytically, the modes would remain orthonormal in time when evolved with the DO equations

$$\frac{\partial \langle \tilde{\mathbf{u}}_i, \tilde{\mathbf{u}}_j \rangle}{\partial t} = \left\langle \frac{\partial \tilde{\mathbf{u}}_i}{\partial t}, \tilde{\mathbf{u}}_j \right\rangle + \left\langle \tilde{\mathbf{u}}_i, \frac{\partial \tilde{\mathbf{u}}_j}{\partial t} \right\rangle = 0 \qquad (2.61)$$

with the application of the DO condition (eq. (2.5)). Numerically, errors creep in due to truncation error and round-off error during time-integration due to which the modes no longer remain orthonormal. This motivates the need for re-orthonormalization.

Suppose that the matrix of modes is given by $\tilde{\mathbf{U}} = [\tilde{\mathbf{u}}_1, ..., \tilde{\mathbf{u}}_{n_s}]$ and the inner product is

$$\langle \tilde{\mathbf{u}}_i, \tilde{\mathbf{u}}_j \rangle = \tilde{\mathbf{u}}_i^T \Lambda_{IP} \tilde{\mathbf{u}}_j \qquad (2.62)$$

where Λ_{IP} is defined according to the variability in the different variables [53]. We want to then ensure that numerically $\tilde{\mathbf{U}}^T \Lambda_{IP} \tilde{\mathbf{U}} = \mathbf{I}$ through time. At the same time, we want to ensure we respect the various schemes for time-integration we have chosen. In the case of linear multi-step IMEX schemes, we need to ensure that there is a correspondence between the columns of $\tilde{\mathbf{U}}(t)$ and $\tilde{\mathbf{U}}(t + \Delta t)$. Suppose that the modes $\tilde{\mathbf{U}}(t)$ at time t are integrated over one time-step to obtain $\hat{\tilde{\mathbf{U}}}(t + \Delta t)$ which is not orthonormal up to round-off error. Any re-orthonormalization procedure that is applied to $\hat{\tilde{\mathbf{U}}}(t + \Delta t)$ to obtain $\tilde{\mathbf{U}}(t + \Delta t)$ should satisfy the following properties:

1. not reorder, rotate or mix the modes

2. retain the original DO solution and reconstructed realizations

One simple solution to the above is the Gram-Schmidt re-orthogonalization. It is known that the classical Gram-Schmidt procedure is backward unstable [122]. The modified Gram-Schmidt algorithm could be used in it's place but this also suffers from instabilities during long time-integrations [44] and an iterative procedure must be followed which may be expensive.

An SVD-based algorithm for re-orthonormalization was proposed in [124]. While this maintains realizations during the procedure, it suffers from multiple pitfalls. As the SVD of a matrix is non-unique, it introduces sign changes of the modes, reorders and also mixes the modes. While a fix was suggested to prevent sign changes in [125], fixes to the other problems were not. The reordering and mixing of modes did not effect the DO solution because a first order semi-implicit backward difference (IMEX-SBDF1) was used for time-integration. In effect, the scheme did not 'see' modes from earlier time-steps and continuity of modes was not required. However, this is required in the case of linear multi-step IMEX schemes and thus an alternate re-orthonormalization procedure must be selected. Moreover, it was suggested in [125] to introduce bi-orthogonality i.e. decorrelate the stochastic coefficients in addition to orthonormality of modes. While this would give us a KL expansion for the realizations at that time instance, this is not necessitated by the DO equations themselves. Moreover, the process of decorrelation destroys the continuation of modes and stochastic coefficients between different time instances and would prevent us from tracking the correct DO solution.

Another solution was proposed in [25, 24]. The idea is to find a linear transformation $\mathbf{A} \in \mathcal{R}^{n_s \times n_s}$ such that $\tilde{\mathbf{U}} = \hat{\mathbf{U}}\mathbf{A}$. In [24], this is framed as a solution to the following unconstrained optimization problem

$$\underset{\mathbf{A} \in \mathcal{R}^{n_s \times n_s}}{\arg\min} \; ||\mathbf{A}^T \mathbf{K} \mathbf{A} - \mathbf{I}||^2 \tag{2.63}$$

where $|| \cdot ||$ denotes the Frobenius norm and $\mathbf{K} = \hat{\mathbf{U}}^T \Lambda_{IP} \hat{\mathbf{U}}$ is the Gram matrix. This was solved using a gradient flow of the dynamical system

$$\frac{d\mathbf{A}}{dt} = -\frac{\partial G}{\partial \mathbf{A}} = -4\mathbf{K}\mathbf{A}(\mathbf{A}^T \mathbf{K}\mathbf{A} - \mathbf{I}) \tag{2.64}$$

where $G(A) = ||\mathbf{A}^T \mathbf{K}\mathbf{A} - \mathbf{I}||^2$ and $\mathbf{A}_0 = \mathbf{I}$ is used as the initial guess. This approach allows us to find $\mathbf{A}$ which orthonormalizes the modes but it is not necessarily close to $\mathbf{I}$. This is why the initial guess of $\mathbf{A}_0 = \mathbf{I}$ is chosen so that we may converge to $\mathbf{A}$ that orthonormalizes the modes and is close to $\mathbf{I}$. Moreover, the stopping criterion

and the step-size chosen for the time-marching will effect the rate of convergence and the overall cost of the approach.

Before we discuss the solution proposed in [70] which overcomes the problems of the above approaches, let us formalize the mathematical notions of the properties we would like the reothornmalization procedure to have. The first step is to introduce the scaled Frobenius norm:

$$||\mathbf{A}||^2_{F,\mathbf{K}} = tr(\mathbf{A}^T\mathbf{K}\mathbf{A}) \tag{2.65}$$

The optimization problem of eq. (2.63) then becomes

$$\underset{\mathbf{A}\in\mathcal{R}^{n_s\times n_s}}{\arg\min} ||\mathbf{A} - \mathbf{I}||^2_{F,\mathbf{K}} \tag{2.66}$$

This is useful as it is also equivalent to the deviation of the transformed modes $\tilde{\mathbf{U}}$ from the original modes $\hat{\tilde{\mathbf{U}}}$ [69]

$$||\mathbf{A} - \mathbf{I}||^2_{F,\mathbf{K}} = ||\hat{\tilde{\mathbf{U}}}\mathbf{A} - \hat{\tilde{\mathbf{U}}}||_{F,\Lambda_{IP}} = ||\tilde{\mathbf{U}} - \hat{\tilde{\mathbf{U}}}||_{F,\Lambda_{IP}} = \sum_{i=1}^{n_s} ||\tilde{\mathbf{u}}_i - \hat{\tilde{\mathbf{u}}}_i||^2_{\Lambda_{IP}} \tag{2.67}$$

Solving the optimization problem (eq. (2.66)) will then allow us to satisfy both the properties we desire from the re-orthonormalization procedure. An optimal SVD based reorthonormalization algorithm [70] is then given as

1. Perform eigendecomposition of the Gram matrix $\mathbf{K} = \mathbf{V}\mathbf{\Sigma}\mathbf{V}^T$

2. Compute the optimal linear transformation $\mathbf{A} = \mathbf{V}\mathbf{\Sigma}^{-1/2}\mathbf{V}^T$

3. Transform the modes so as to re-orthonormalize them $\tilde{\mathbf{U}} = \hat{\tilde{\mathbf{U}}}\mathbf{A}$

4. Transform the stochastic coefficients so as to maintain realizations $\mathbf{Y} = \hat{\mathbf{Y}}\mathbf{A}^{-T}$

The proof that the above procedure allows us to obtain the solution to the optimization problem (eq. (2.66)) can be found in [70]. This completes the discussion

48

on re-orthonormalization and only the criteria of choosing the time-step size Δt remains. In order to ensure stability in the IMEX schemes, Δt is selected according to the Courant-Friedrichs-Lewy (CFL) condition [9, 8]. Through the DO methodology, we are effectively evolving an ensemble of realizations. It is important to ensure that the CFL condition is satisfied for each of these realizations. Hence, we select the maximum velocity among all these realizations and set Δt as follows

$$\Delta t \leq C_{max} \left(\frac{\max |\mathbf{u}| + \sum_{i=1}^{n_s} \max |\tilde{u}_i| \max |Y_i|}{\Delta x} + \frac{\max |\mathbf{v}| + \sum_{i=1}^{n_s} \max |\tilde{v}_i| \max |Y_i|}{\Delta y} \right)^{-1}$$
(2.68)

where C_{max} marks the boundary of the stability region for the respective IMEX scheme.

2.5   Numerical Results

We showcase our results using three test cases: (i) stochastic passive tracer advection in a deterministic swirl flow, (ii) stochastic flow past a cylinder and (iii) stochastic lid driven cavity flow.

2.5.1   Stochastic Passive Tracer Advection in Deterministic Swirl Flow

We consider the test case of stochastic passive tracer advection in deterministic swirl flow with the same setup as in [75]. We introduce uncertainty here by considering stochastic initial conditions in the concentration of the tracer. The stochastic concentration of tracer is denoted by $\rho(\mathbf{r}, t; \omega) = \bar{\rho}(\mathbf{r}, t) + \sum_{j=1}^{s} \tilde{\rho}_j(\mathbf{r}, t)\Phi_j(t; \omega)$. The domain is a unit square basin. The background flow is a deterministic velocity flow field given by $\mathbf{u} = [u_x, u_y]^T$

$$u_x = \sin^2(\pi r_x) \sin(2\pi r_y)$$
(2.69)

$$u_y = -\sin^2(\pi r_y) \sin(2\pi r_x)$$
(2.70)

It is essentially a divergence-free counter-clockwise rotating flow (Fig. 2-3) which vanishes at the domain boundaries. Initial conditions of the tracer concentration are given by

$$\rho(\mathbf{r}, 0; \omega) = \frac{1}{2} \left[1 + \cos(\pi D(\mathbf{r}; \omega)) \right] \tag{2.71}$$

where,

$$D(\mathbf{r}; \omega) = \max 0, 1 - 4 \|\mathbf{r} - \mathbf{R}_c(\omega)\| \tag{2.72}$$

$$\mathbf{R}_c(\omega) \sim \mathcal{N}\left(\cdot; \begin{bmatrix} 0.5 \\ 0.5 \end{bmatrix}, \begin{bmatrix} 0.0625 & 0 \\ 0 & 0.0625 \end{bmatrix} \right) \tag{2.73}$$

The DO mean, modes and stochastic coefficients are initialized as was described in equations 2.23, 2.28 and 2.31. In the results presented here, we use $n_s = 9$ and $N_r = 10^4$ ensemble members in the DO decomposition.

The evolution of the stochastic tracer concentration is governed by the stochastic DO advection equations:

$$\frac{\partial \bar{\rho}(\mathbf{r}, t)}{\partial t} + \mathbf{u} \cdot \nabla_{\mathbf{r}} \bar{\rho} = 0 \tag{2.74}$$

$$\frac{\partial \tilde{\rho}_i(\mathbf{r}, t)}{\partial t} + \mathbf{u} \cdot \nabla_{\mathbf{r}} \tilde{\rho}_i - \sum_{j=1}^{s} \langle \mathbf{u} \cdot \nabla_{\mathbf{r}} \tilde{\rho}_i, \tilde{\rho}_j \rangle \tilde{\rho}_j = 0 \tag{2.75}$$

$$\frac{d\Phi_i(t; \omega)}{dt} + \sum_{j=1}^{s} \langle \mathbf{u} \cdot \nabla_{\mathbf{r}} \tilde{\rho}_j, \tilde{\rho}_i \rangle \Phi_j(t; \omega) = 0 \tag{2.76}$$
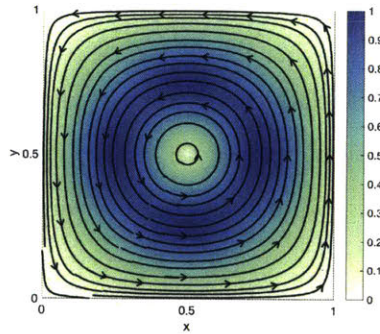
Figure 2-3: Deterministic velocity field of swirl flow. Magnitude of velocity field is plotted over the domain and is overlaid with streamlines.

50

We carry out the simulation within a time-interval of $[0, 10]$ using the 2nd order linear centered advection scheme with Shapiro filtering and various time-integration schemes. Figures 2-4 and 2-5 show the time evolution of the DO mean, first five DO modes and their corresponding coefficients. It should be noted we continuously track and show the first five DO modes and not the dominant modes. This is indicated also by the time-evolution of the variance of the stochastic coefficients in Fig. 2-8a where we see multiple criss-crossings of the coefficients. This shows that the re-orthonormalization technique described in section 2.4 allows us to maintain continuity in between modes.
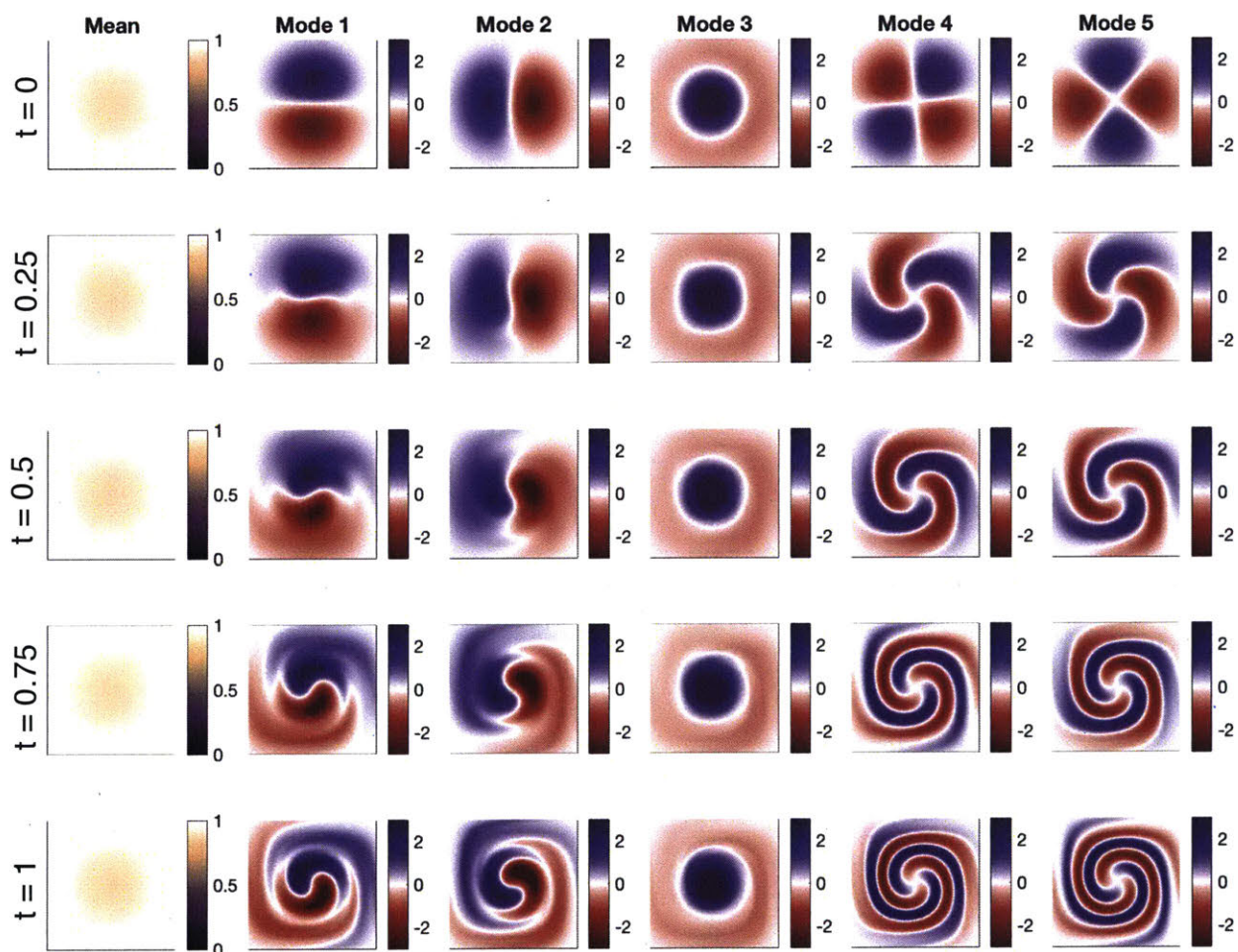
Figure 2-4: Stochastic tracer advection in a deterministic swirl flow: Time-evolution of the DO mean $\bar{\rho}(\mathbf{r}, t)$ and the first five DO modes $\tilde{\rho}_i(\mathbf{r}, t)$.

In order to assess the consistency of the advection evaluation, we look at the time-evolution of a randomly sampled DO realization and the corresponding MC realization that it is trying to track. The results of CDS advection scheme with Shapiro filtering are shown in Fig. 2-6 and those obtained considering a TVD advection scheme are shown in Fig. 2-7. Both were performed considering a second order Runge-Kutta (RK2) time-integration scheme. We clearly see that the error in between the DO and MC realizations is much lower (i.e. of nearly three orders) in the case of using a centered advection scheme as compared to using a TVD advection scheme. Moreover, the error field is much smoother than that obtained in the latter case. This test case was performed with other explicit multi-step and multi-stage time-integration schemes to verify the temporal order of convergence. The results are summarized in Fig. 2-8b.
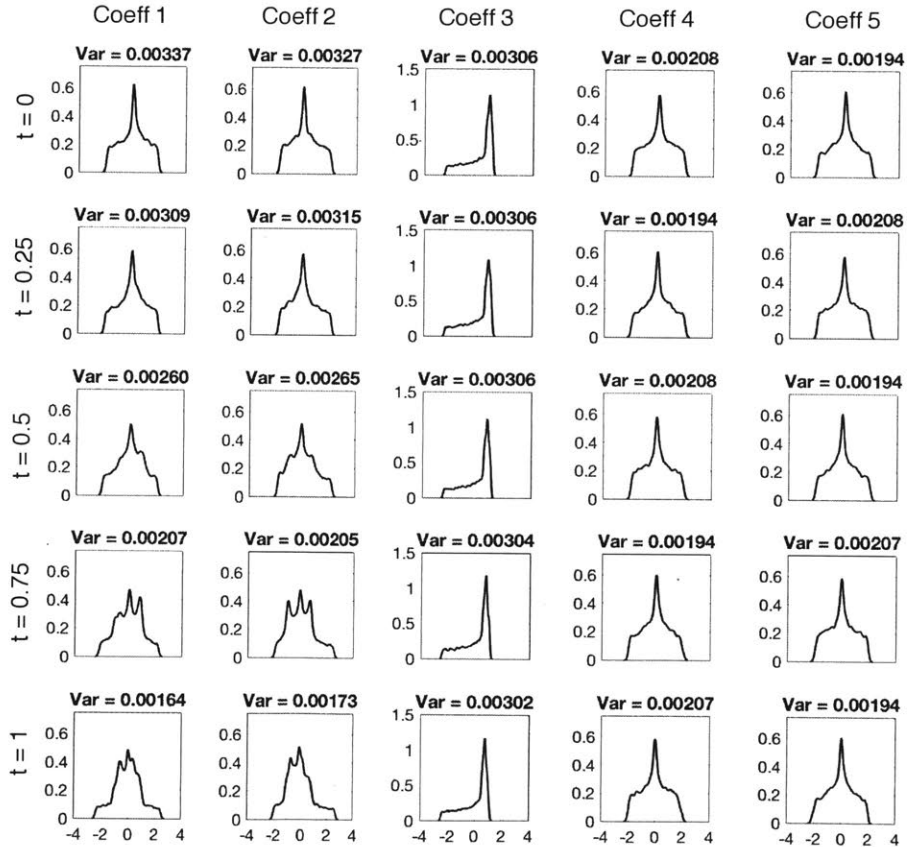
Figure 2-5: Stochastic tracer advection in a deterministic swirl flow: Time-evolution of the stochastic coefficients corresponding to the first five DO modes $\Phi_i(t;\omega)$.
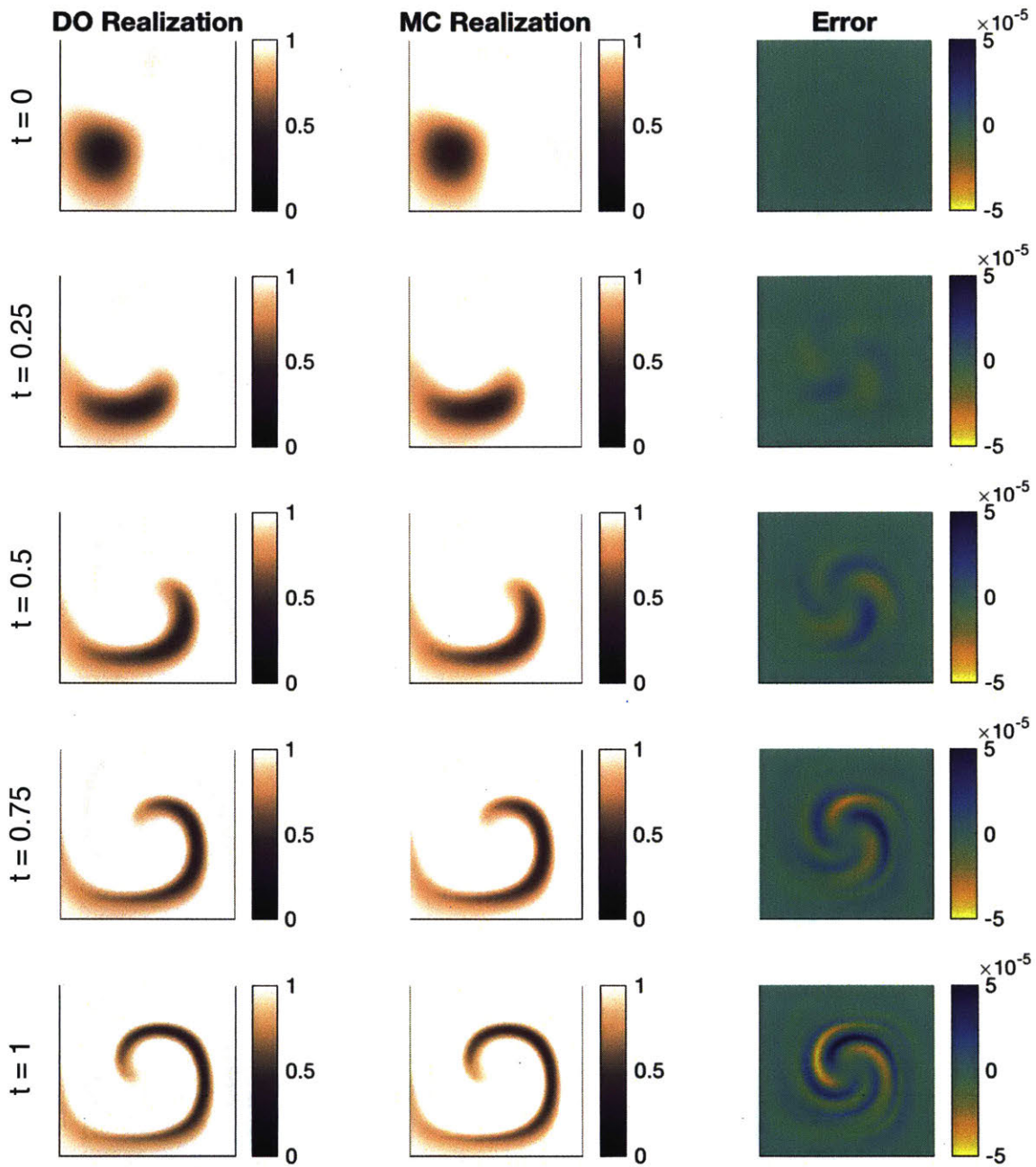
Figure 2-6: Stochastic tracer advection in deterministic swirl flow: Time-evolution of a selected DO realization (reconstructed) and the corresponding MC realization which it is trying to track considering CDS advection scheme, Shapiro filter with parameters $(8, 10, 1)$ and second order Runge-Kutta Scheme (RK2). Error in between the DO and MC realizations is also shown in the third column.
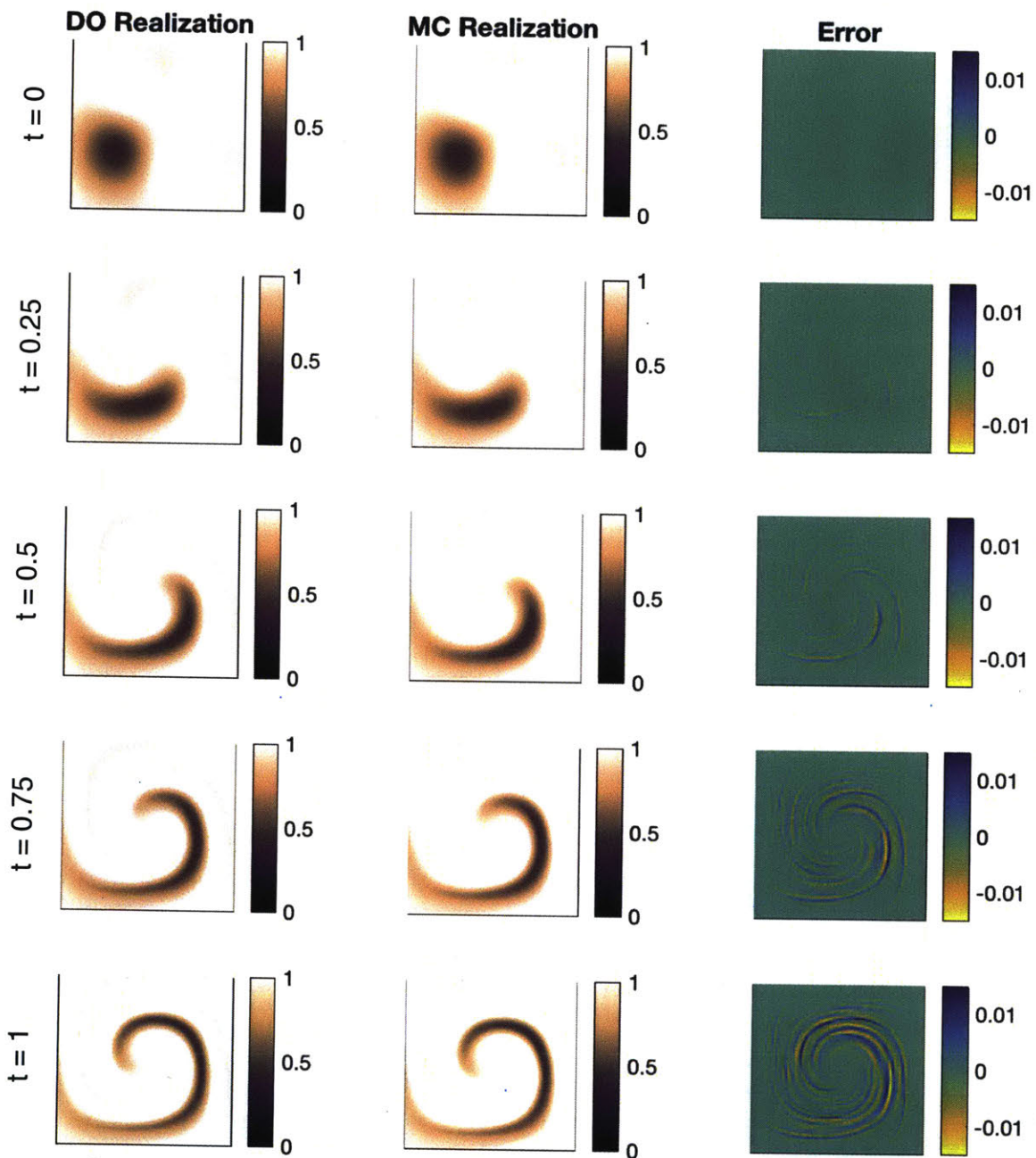
Figure 2-7: Stochastic tracer advection in a deterministic swirl flow: Time-evolution of a selected DO realization (reconstructed) and the corresponding MC realization which it is trying to track considering the TVD* advection scheme, and second order Runge-Kutta Scheme (RK2). Error in between the DO and MC realizations is also shown in the third column.
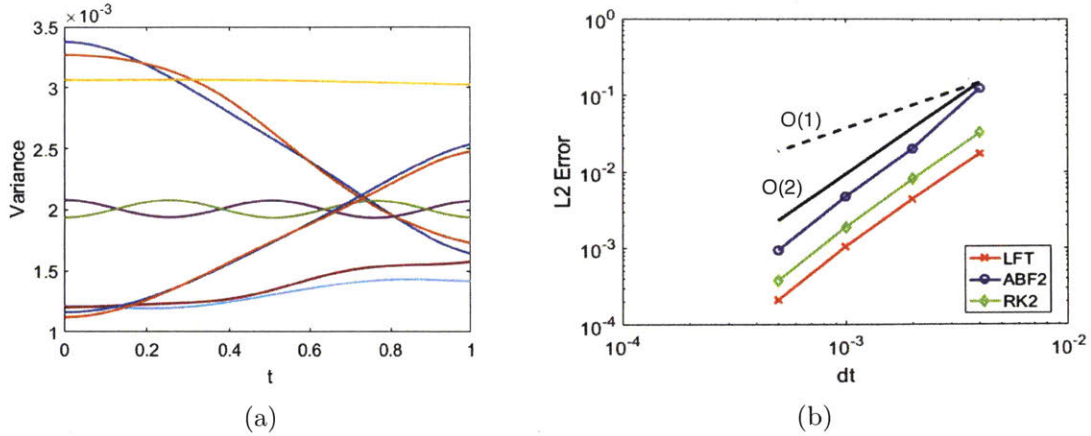
Figure 2-8: Stochastic tracer advection in a deterministic swirl flow: (left) Time-evolution of variances of the stochastic coefficients considering CDS advection scheme, Shapiro filter with parameters $(8, 10, 1)$ and second order Runge-Kutta Scheme (RK2). (right) Temporal convergence of modes considering CDS advection scheme, Shapiro filter with parameters $(8, 10, 1)$ and fixed control volume size of $\Delta x = 0.01$. Leapfrog-trapezoidal (LFT), 2nd order Adams-Bashforth (ABDF2) and second order Runge-Kutta (RK2) time-marching schemes are considered. Optimal convergence of order 2 is obtained.

2.5.2 Stochastic Flow Past a Cylinder

In the second test case, we consider the stochastic flow past a cylinder in a channel. This forms the basis of multiple natural phenomena in geophysical fluid applications [115, 99]. The flow is governed by the stochastic Navier-Stokes equations 2.14 which we will study here using the DO methodology. We consider a domain of size 16×6 with a circular disk of radius 1 located along the centerline at a distance of 4.5 from the inlet and boundary conditions on velocity as shown in Fig. 2-9. A deterministic inlet velocity of $\mathbf{u} = [1, 0]^T$ m/s is considered on the western boundary. Free-slip boundary conditions are applied on the northern and southern boundaries, and open conditions at the outlet (eastern boundary). No-slip boundary conditions are applied on the circular disk. The flow was considered to have a kinematic viscosity of $0.01m^2/2$ corresponding to $Re = 100$.

$$\frac{\partial u}{\partial y} = 0, \ v = 0$$

$u = u_o$
$v = 0$

$u = 0$
$v = 0$

$\frac{\partial u}{\partial x} = 0$
$\frac{\partial v}{\partial x} = 0$

6

4.5

16

$$\frac{\partial u}{\partial y} = 0, \ v = 0$$
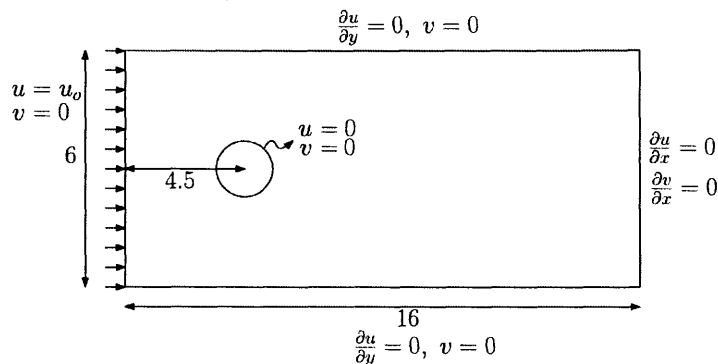
Figure 2-9: Stochastic flow past a cylinder: Schematic of the domain and boundary conditions on velocity.

Uncertainty is introduced into the system by considering uncertainty in the initial condition of velocity. Covariance matrices were constructed using the boundary-mollified spatial covariance approach described in [124]. We consider $n_s = 8$ modes to capture 99.9% of the uncertainty and use $N_r = 10^4$ DO realizations. In order to induce vortex shedding quicker, a divergence-free exponentially decaying perturbation is added to the DO mean field upstream of the disk. The results shown here were obtained by considering the second order centered advection scheme with Shapiro filtering, second order centered discretization for diffusion and second order IMEX-SBDF2 time-integration scheme. Similar results were obtained using the other time-integration schemes discussed before. A resolution of 240 × 90 was chosen along with a fixed time-step Δt such that $CFL = 0.4$.

We show the time-evolution of the DO mean and the dominant three modes of the flow field in 2-10 after vortex-shedding starts in all the realizations. The stochastic initial conditions leads to uncertainty in the time when vortex shedding starts, the face of the cylinder (north/south) from which the first vortex is shed, eddy strength and the shedding frequency (Strouhal number). The dominant modes along with the stochastic coefficients allows to us in capture all these different realizations. The marginal PDFs of the stochastic coefficients corresponding to the dominant three modes as a function of time are shown in Fig. 2-11. The markers on the alphabet of the stochastic coefficients are those of the selected DO realizations which we re-

constructed in Fig. 2-12 and compared against the corresponding MC realizations. We see that the DO realizations match very well with the corresponding MC realizations through time and the different vortex shedding patterns are captured as well. The relative error between the DO and MC solutions remain within 1% even after 2500 time-steps 2-13 Further, high-order time-marching allows us to capture the non-Gaussian statistics (Fig 2-14).

Figure 2-10: Stochastic flow past a cylinder: Time-evolution of the DO mean and the first three dominant modes of velocity are shown by plotting vorticity overlaid with streamlines. CDS advection scheme, Shapiro filter with parameters $(8, 3, 1)$ and IMEX-SBDF2 time-integration was used.

Figure 2-11: Stochastic flow past a cylinder: Time-evolution of the stochastic coefficients corresponding to the first three dominant modes of velocity are shown. The red and blue markers on the alphabet of the coefficients correspond to the selected reconstructed DO realizations 1000 and 9000 which are compared against their corresponding MC realizations in Fig. 2-12. CDS advection scheme, Shapiro filter with parameters $(8, 3, 1)$ and IMEX-SBDF2 time-integration was used.
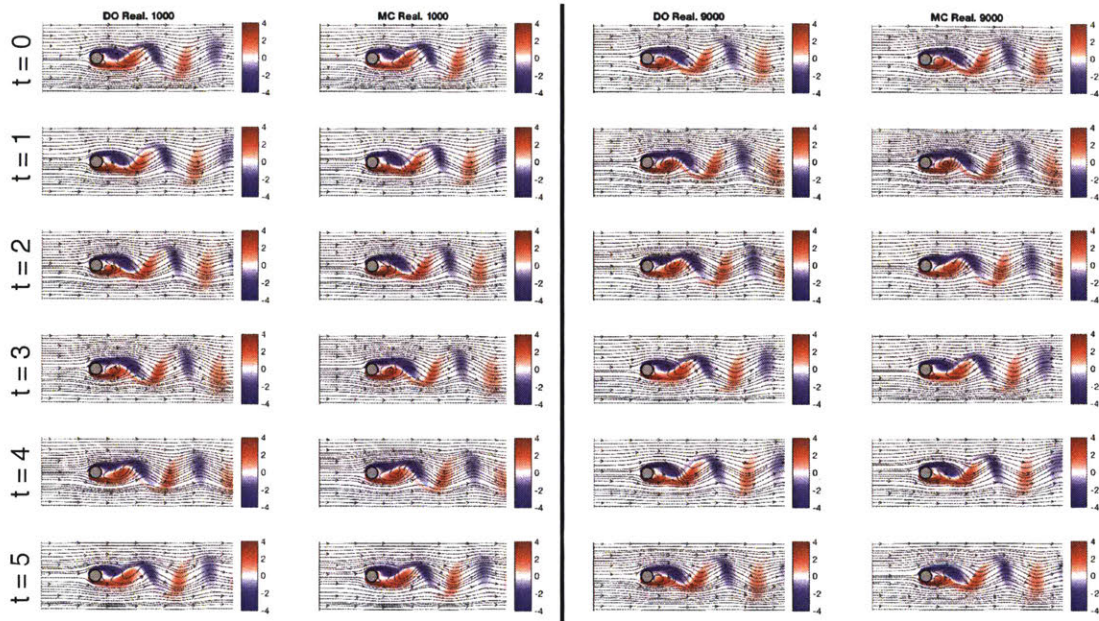
Figure 2-12: Stochastic flow past a cylinder: Time-evolution of the selected DO realizations and corresponding MC realization. Vorticity of the realization is plotted overlaid with streamlines. CDS advection scheme, Shapiro filter with parameters $(8, 3, 1)$ and IMEX-SBDF2 time-integration was used.
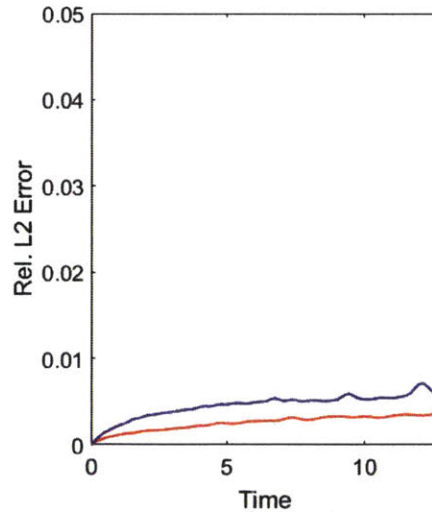
Figure 2-13: Stochastic flow past a cylinder: Relative error between the DO and MC realizations shown in Fig. 2-12 is plotted considering second order CDS advection scheme with Shapiro filtering and IMEX-SBDF2 time-integration. Red and blue lines are the trends for realizations 1000 and 9000 respectively.

59

Figure 2-14: Stochastic flow past a cylinder: Joint second marginal PDF of the stochastic coefficients corresponding to the first six dominant DO modes at $t = 5$.

2.5.3 Stochastic Lid Driven Cavity Flow

The final test case that we study is the stochastic lid driven cavity flow which is also governed by the stochastic Navier-Stokes equations 2.14. This test case will be used to check consistency between the DO and MC solution, and verify the order of accuracy of the implemented schemes by performing numerical convergence studies.

The domain of interest is a square cavity of length 1 with a lid at the top which is used to drive the flow. The flow configuration is illustrated in Fig. 2-15. No-slip boundary conditions are applied at all the boundaries except for at the top where a Dirichlet boundary condition of u_b in the x-direction is set according to the velocity of the lid. We consider the fluid to have a kinematic viscosity of $10^{-3} m^2/s$ and thus $Re = 1000$.

Uncertainty is introduced through the initial conditions and the mollified-boundary

approach is followed again [125, 97]. We retain $n_s = 10$ modes to capture 99.9% of the uncertainty. The DO mean of the flow field, the three most dominant modes and their corresponding coefficients are plotted in Fig. 2-16. The mean velocity and pressure are initialized to zero. These are evolved over a time interval of $[0, 15]$.
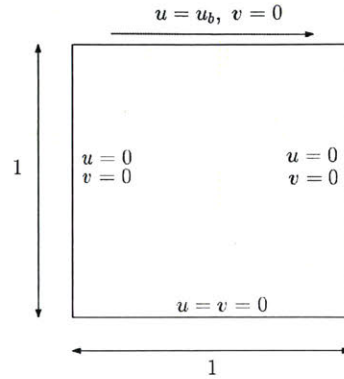
Figure 2-15: Stochastic lid-driven cavity flow: Schematic of the domain and boundary conditions on velocity.
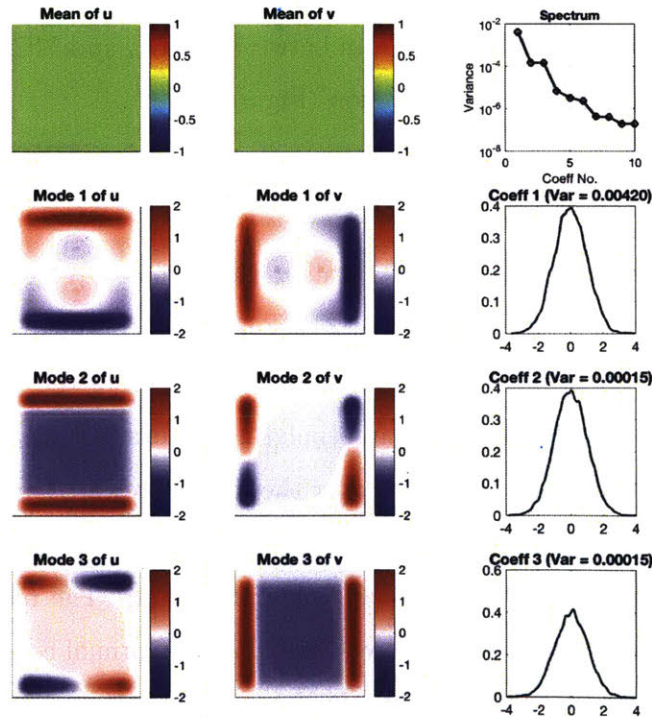
Figure 2-16: Stochastic lid-driven cavity flow: Initial conditions of the velocity mean, modes and stochastic coefficients.

We first look at the time-evolution of the mean, modes and coefficients considering a resolution of 80×80 to ensure that the flow is well resolved and a fixed time-step isuch that $CFL = 0.2$. Figure 2-17 shows the time-evolution of the mean flow along with the three most dominant modes considering 2nd order CDS advection scheme with Shapiro filtering and IMEX-SBDF2 for time-integration. Figure 2-18 shows the time-evolution of the corresponding stochastic coefficients and a randomly sampled DO realization which is compared against the corresponding MC realization. We observe that after a transient phase, the variance of the stochastic coefficients become very low. This can be explained by the fact that after a transient phase, the solution converges to a stable deterministic attractor. However, all the different realizations follow a different route and this is captured using the DO methodology. The sampled DO realization is but one example of such a route. Figure 2-19 is an illustration of the non-Gaussian statistics that is observed during the transient phase. Consistent advection evaluation combined with high-order time-integration allows us to effectively track the MC solution and hence ensure consistency. This is further evident by comparing the relative error in between the DO and MC solutions against the case when TVD* is used for advection (Figure 2-21).

Numerical Convergence Studies

For spatial convergence analysis, we considered the time-step to be fixed at $\Delta t = 1/4096$. The finest spatial resolution of 512×512 was considered to be the exact solution and used for obtaining error estimates. We obtain the error between the coarser solution and exact solution by interpolating the exact solution onto the coarse grid and then calculating the L^2 norm over the interior of the domain $[0.25, 0.75] \times [0.25, 0.75]$. This is to avoid the singularities which occur at the boundaries of the top two corners. A similar strategy was also followed in [124]. The results for the case of IMEX-SBDF2 time-marching is shown in Fig. 2-22. Optimal convergence of order 2 is obtained. Similar results were obtained for IMEX-RK (2,3,2) (eq. (2.60)) and IMEX-RK (2,3,3) (eq. (2.59)) time-integration schemes which are not shown here.

For temporal convergence analysis, the control volume size was fixed at $\Delta x =$

$\Delta y = 1/256$. The finest temporal resolution of $\Delta t = 1/4096$ was considered to be the exact solution and used for obtaining error estimates. The error is calculated over the interior as was done for spatial convergence analysis. The results for the IMEX-SBDF2, IMEX-RK (2,3,2) and IMEX-RK (2,3,3) time-integration schemes are shown in Fig. 2-23. The order of convergence for the mean and modes of velocity, and stochastic coefficients matches with the theoretical optimal order of convergence i.e. 2. Using a higher order time-marching scheme such as IMEX-RK (2,3,3) (Fig. 2-23c) does not help in improving order of convergence due to the projection method's time-splitting [32] but does help in obtaining more accurate results than IMEX-SBDF2 (Fig. 2-23a). Due to the time-splitting error, the optimal order of convergence obtained for mean and modes of pressure is also 3/2 in most general cases [33] and this is observed here as well. To recover the order of convergence of the time-integration scheme used, reiterations may be performed [2].
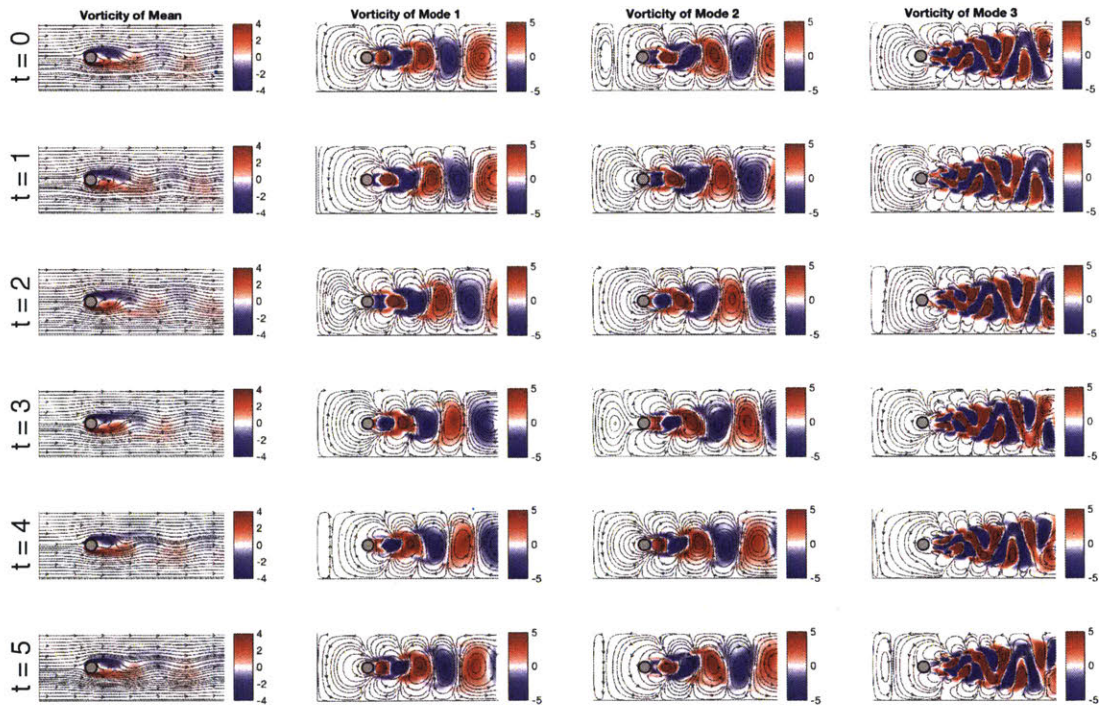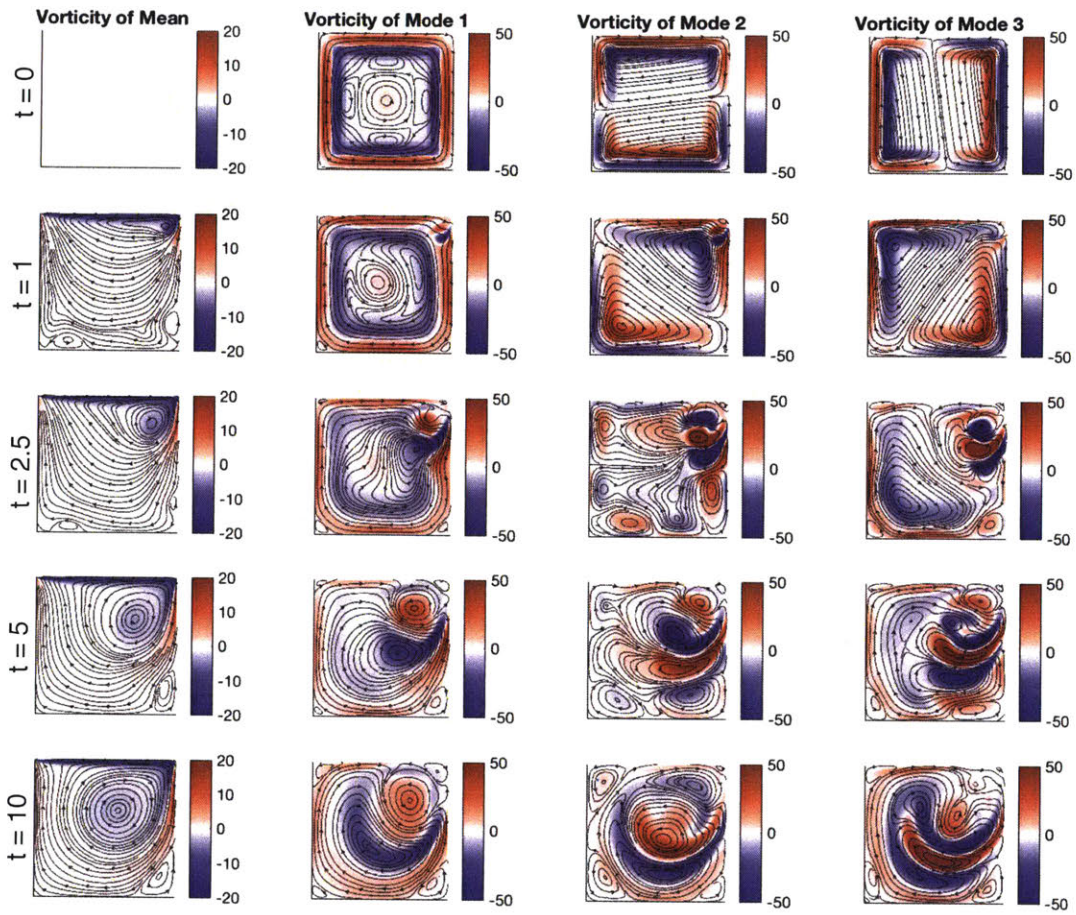
Figure 2-17: Stochastic lid-driven cavity flow: Time-evolution of the DO mean and the first three DO modes of velocity are shown by plotting vorticity overlaid with streamlines. CDS advection scheme, Shapiro filter with parameters $(8, 10, 1)$ and IMEX-SBDF2 time-integration was used.
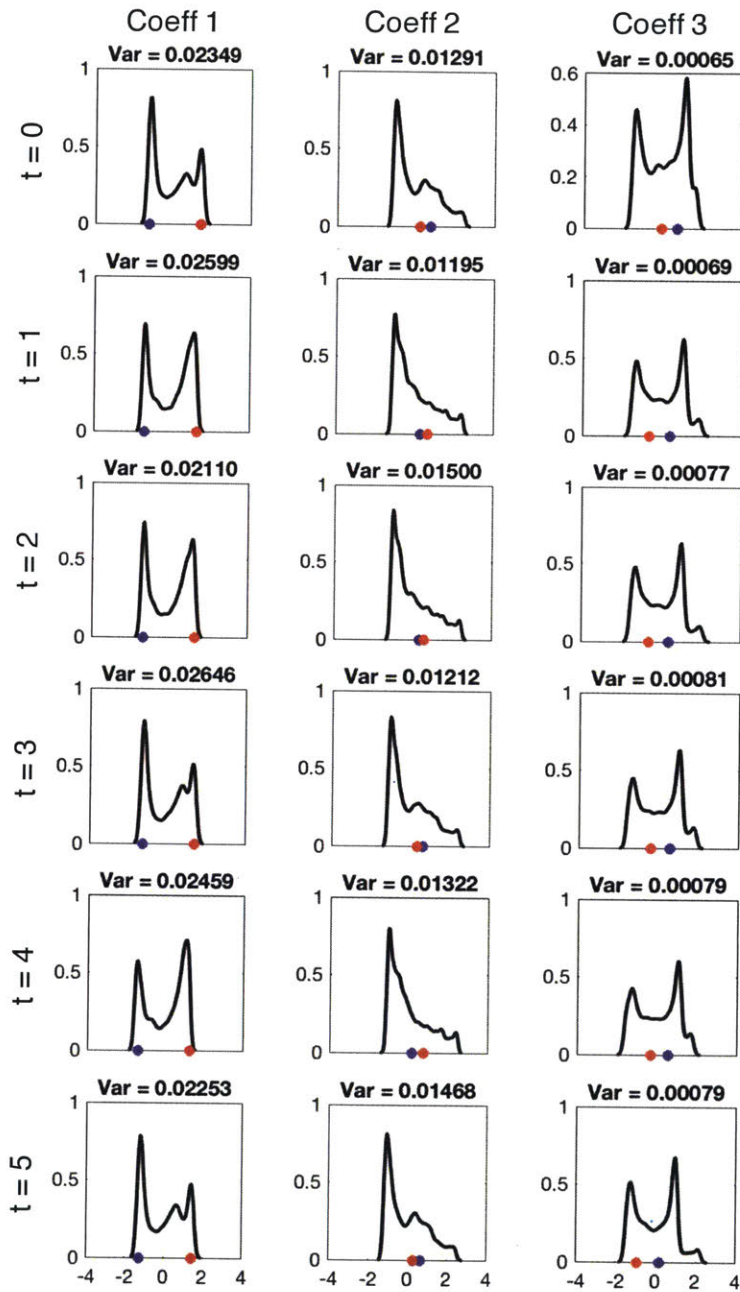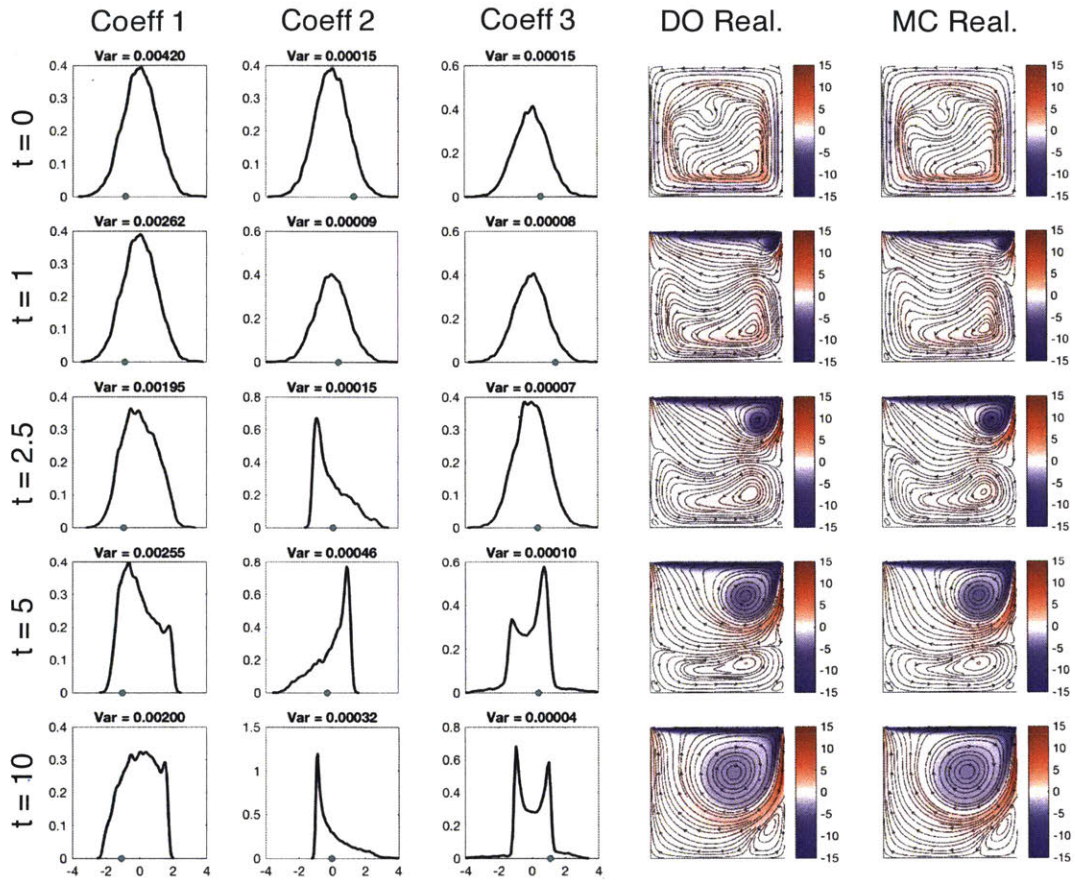
Figure 2-18: Stochastic lid-driven cavity flow: Time-evolution of the stochastic coefficients corresponding to the first three dominant modes of velocity are shown along with a selected DO realization and corresponding MC realization. Vorticity of the realization is plotted overlaid with streamlines. The marker on the alphabet of the coefficients correspond to the reconstructed DO realization. CDS advection scheme, Shapiro filter with parameters (8, 10, 1) and IMEX-SBDF2 time-integration was used.
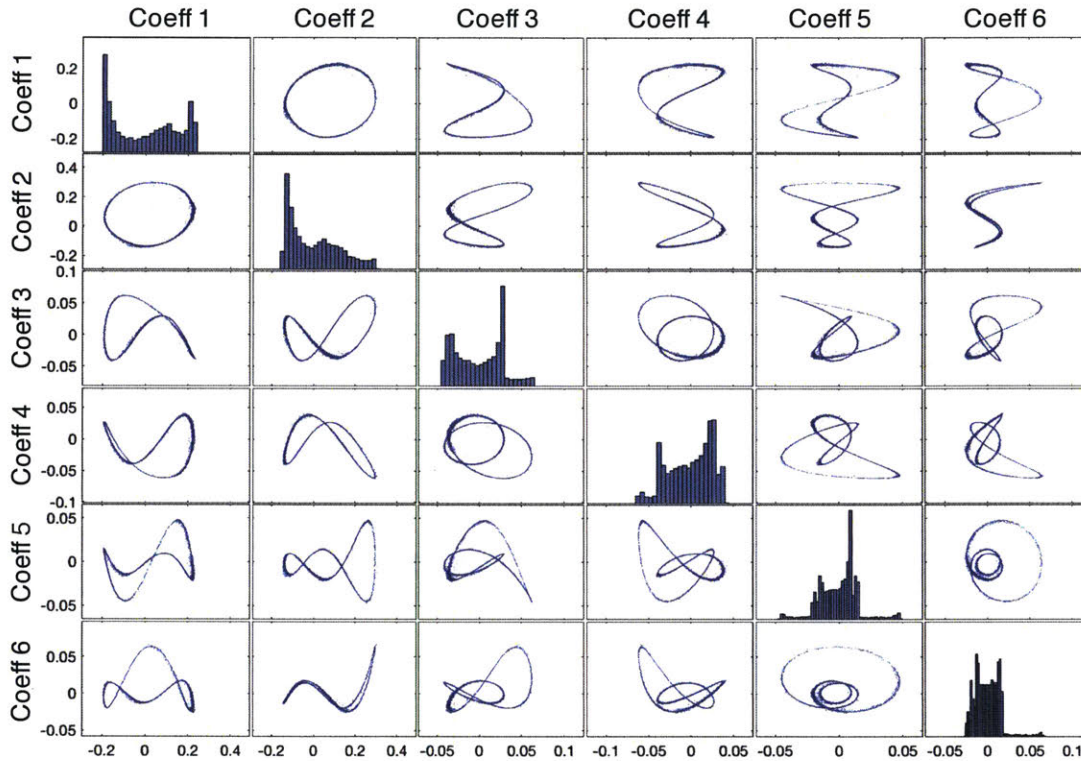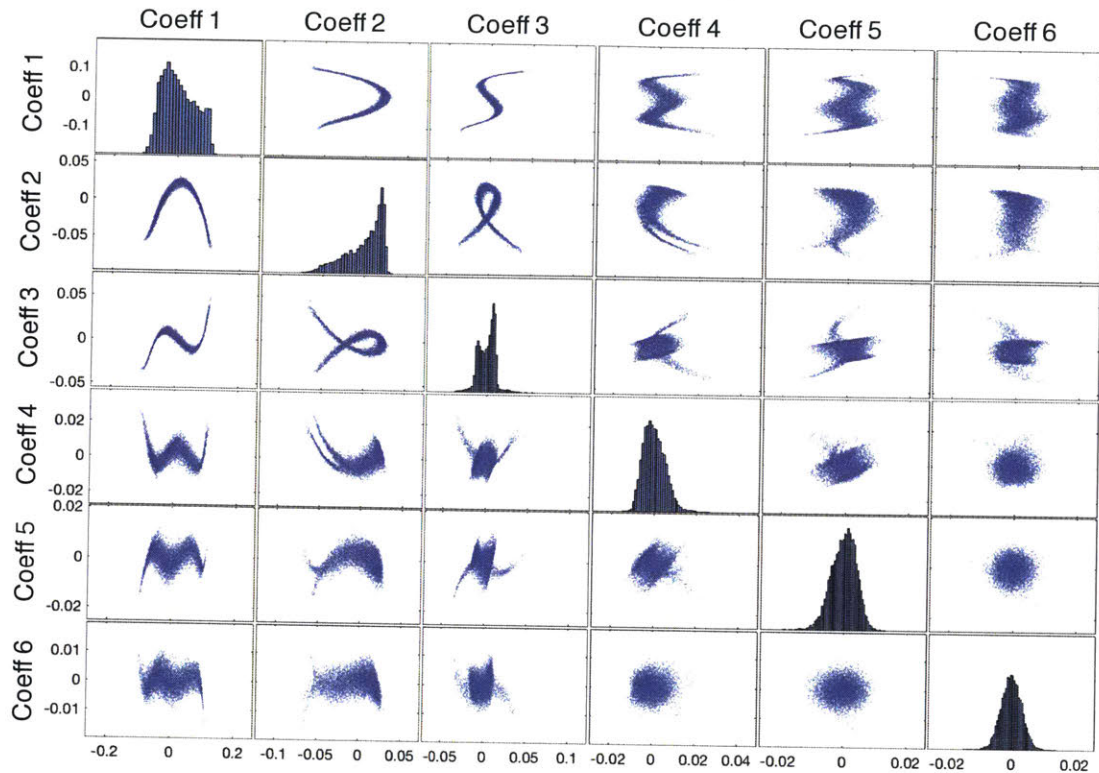
Figure 2-19: Stochastic lid-driven cavity flow: Joint second marginal PDF of the stochastic coefficients corresponding to the first six dominant DO modes at $t = 5$.
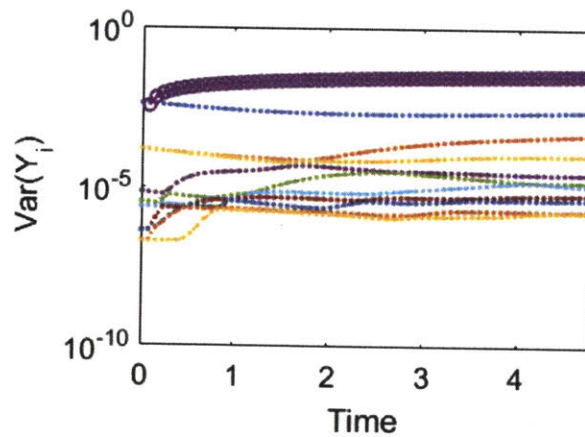
Figure 2-20: Stochastic lid-driven cavity flow: Time-evolution of the variance of stochastic coefficients considering CDS advection scheme, Shapiro filter with parameters $(8, 10, 1)$ and IMEX-SBDF2 time-integration.

66
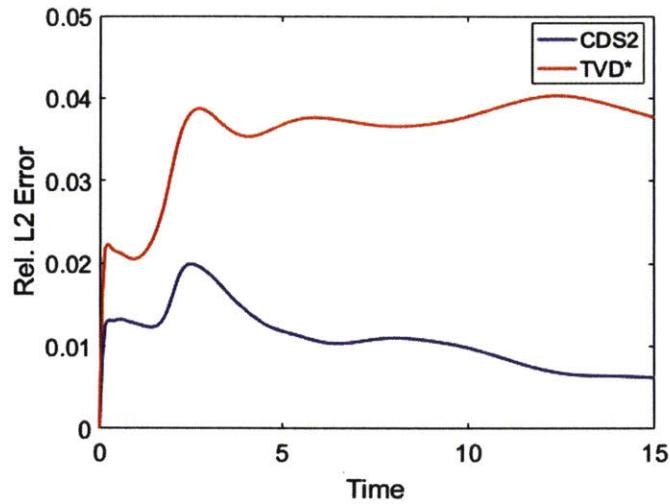
Figure 2-21: The relative error between the DO and MC realization shown in Fig. 2-18 is plotted against that obtained using a TVD* advection scheme with IMEX-SBDF2 time-integration.
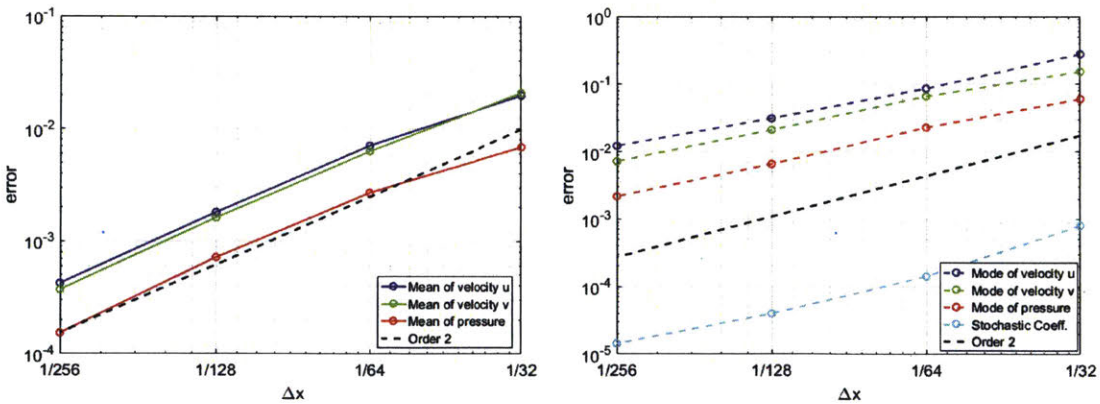
Figure 2-22: Spatial convergence (L^2 norm) of mean (left) with modes and stochastic coefficients (right) of pressure and velocity. The trend for the first mode and the corresponding coefficient is shown. The time-step size is held fixed at $\Delta t = 1/4096$. A second order CDS scheme with Shapiro filtering and IMEX-SBDF2 time-integration was used. Convergence is near optimal i.e. order 2.
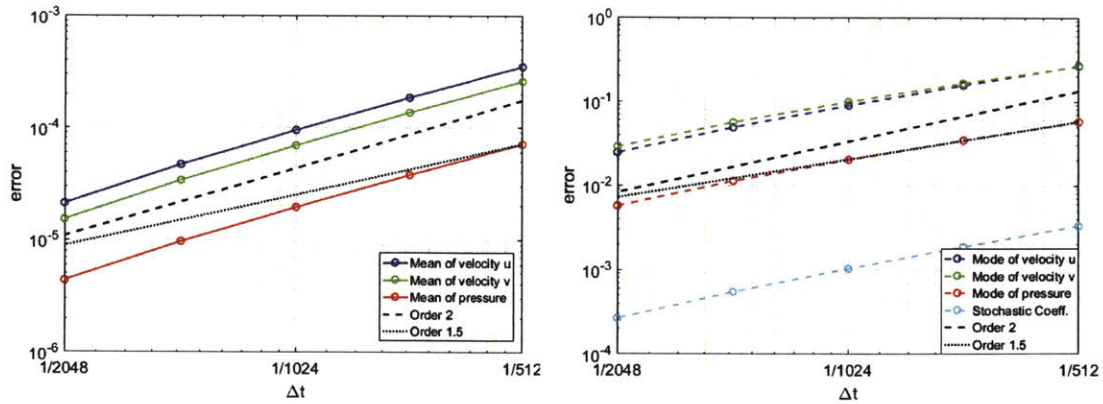
(a) IMEX-SBDF2
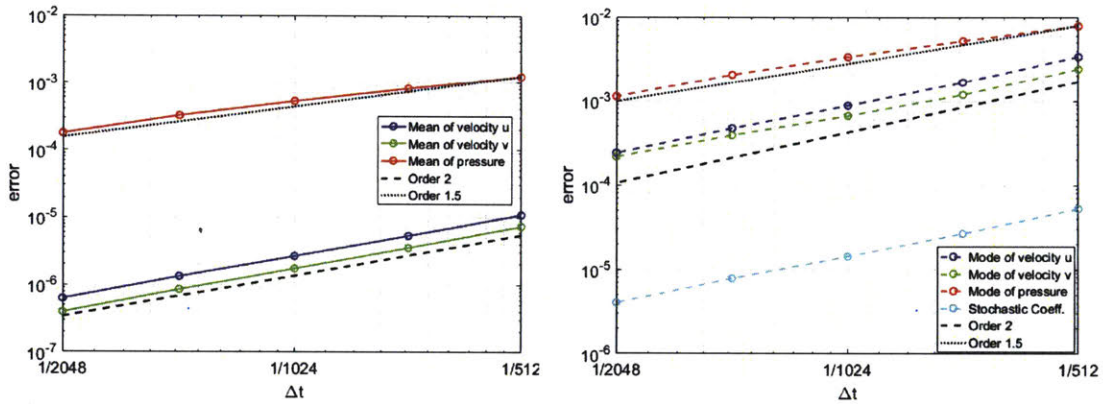
(b) IMEX-RK (2,3,2) (Eq. 2.60)
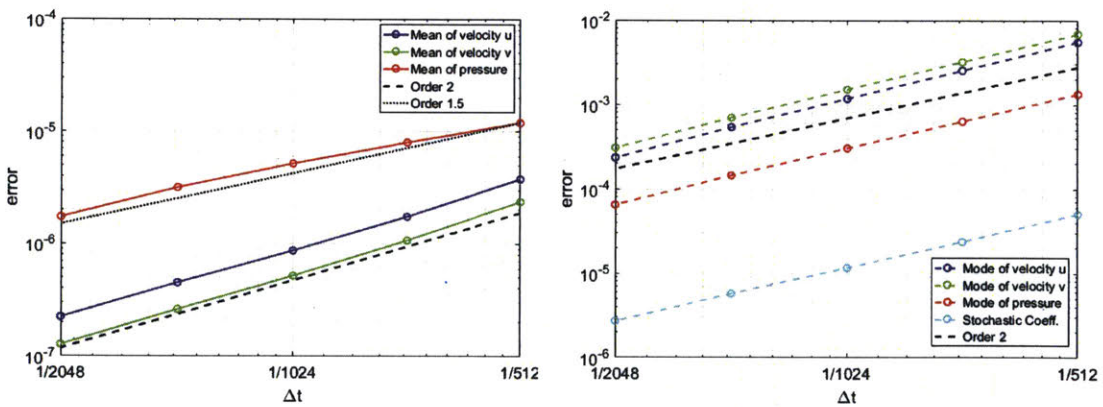
(c) IMEX-RK (2,3,3) (Eq. 2.59)

Figure 2-23: Temporal convergence (L^2 norm) of mean (left column) with modes and stochastic coefficients (right column) of pressure and velocity. The different rows indicate the different time-integration schemes used. The trend for the first mode and the corresponding coefficient is shown. The control volume size is held fixed at $\Delta x = \Delta y = 1/256$. A second order CDS scheme with Shapiro filtering was used.

2.6 Summary

In this chapter, we have presented how centered advection schemes with filtering can be combined with high-order IMEX schemes to achieve consistency, accuracy and stability in the DO solution. These allow us to make accurate probabilistic predictions for stochastic velocity fields which can then be used to obtain accurate PDFs of Lagrangian variables. This will be described in the next chapter. Finally, we will describe how assimilation may be carried out to combine observations in Eulerian and Lagrangian variables with predictions.

Chapter 3

Lagrangian Data Assimilation

3.1 Background

3.1.1 Lagrangian Instruments

There are two main platforms in the ocean which provide measurements: (i) Eulerian instruments whose positions are fixed in time (e.g. fixed sensors, moorings, tide gauges, etc.), and (ii) Lagrangian instruments whose positions are time-dependent (e.g. drifters, floats, etc.). The assimilation of data from these Lagrangian instruments forms the topic of Lagrangian Data Assimilation and has become an active area of research in the last two decades [13, 51, 46, 82, 84, 5, 4]. One of the main reasons for this interest is the spatial coverage provided by this platform as indicated by the ever expanding data produced by the World Drifter Program [79]. The main Lagrangian instrument used for sampling the ocean surface has been drifters while floats (e.g. SOFAR, RAFOS, Argo floats) [89] have been used for sampling the ocean interior. Data collected from drifters primarily include their positions (trajectory information) using on-board satellite-tracked transmitters or GPS. Subsurface instruments collect measurements (salinity, temperature, pressure, biology, etc.) from a variety of sensors [91, 90].

Secondly, it allows us to gather information regarding ocean currents that dictate material transport [30] at the surface and in the ocean interior. Pathways for material

transport can be linked to trajectories of drifters which are modeled as passive tracer particles advected by the ocean current

$$\frac{d\mathbf{x}_P}{dt} = \mathbf{u}(\mathbf{x}_P, t) \tag{3.1}$$

where $\mathbf{x}_P$ is the position of the drifter and $\mathbf{u}$ is the velocity field. It should be noted that this equation is highly nonlinear and leads to chaotic behavior [6, 7]. Drifter trajectories are thus sensitive to initial conditions i.e. release locations and two particles (or drifters) which are released very close to each other may not follow similar paths. This chaotic behavior is further aggravated by the high spatial and temporal variability of ocean currents. The consequences are twofold.

Firstly, this indicates that it is useful to look at clusters of trajectories and relative dispersion of drifters to understand material transport. Lagrangian Coherent Structures (LCSs) which were first formalized in [39, 42, 40] are the most persistent material surfaces over a time interval that act as transport barriers. Most popular ways of extracting LCSs in flow rely on first computing measures of relative dispersion such as the finite-time Lyapunov exponent (FTLE) or the finite-size Lyapunov exponent (FTLE). In this work, we consider FTLE fields as a measure of dispersion and will be described in section 3.1.2.

Secondly, this shows that uncertainty in velocity fields due to incomplete knowledge of small scale resolved processes, forcing, topography, coastline, etc. may lead to significant uncertainty in trajectories. This is why we want to use drifter positions as observational data to improve our knowledge of the system through data assimilation. From another perspective, the trajectories will be organized differently from one flow realization to another with change in location and strength of hyperbolic, parabolic and elliptic LCSs. In the next section, we review how FTLE fields can be computed in deterministic and stochastic settings.

3.1.2 Lagrangian Variables: Trajectories, Flow-Maps and LCS

Nearly all approaches for computing and extracting LCS rely on the flow-map. Suppose that we are given a divergence free velocity field $\mathbf{u}(\mathbf{r}, t)$, the flow-map [41] is given by

$$\phi_{t_0}^t(\mathbf{r}_0) = \mathbf{r}(t; t_0, \mathbf{r}_0), \quad \mathbf{r} \in \mathcal{D}, \quad t \in [t_0, t_1] \tag{3.2}$$

where $\mathcal{D}$ is the domain of interest and $[t_0, t_1]$ is the finite time interval of interest. This can be easily obtained by integrating the advection ODE for trajectories in the domain

$$\begin{cases} \dot{\mathbf{r}} = \mathbf{u}(\mathbf{r}, t) \\ \mathbf{r}(0) = \mathbf{r}_0, \end{cases} \tag{3.3}$$

So far we have actually defined the forward flow-map which tells us given the initial position of a particle at time t_0, what will it's position be at time t. It is important to make a distinction between this and the backward flow-map which tell us given the final position of a particle at time t_1, what was it's position at time t. The backward flow-map is simply the inverse of the forward flow-map $(\phi_t^{t_1})^{-1}$. A popular method for obtaining LCS is through the computation of the finite-time Lyapunov exponent (FTLE) field. The forward FTLE is given by

$$\lambda_{t0}^{t1}(\mathbf{r}_0) = \frac{1}{|t_1 - t_0|} \log \sqrt{\lambda_{max}[C(\mathbf{r}; t_0, t_1)]} \tag{3.4}$$

where $C(\mathbf{r}; t_0, t_1)$ is the right Cauchy-Green strain tensor and $\lambda_{max}(\cdot)$ represents the operation of extracting the largest eigenvalue of the operand. The Cauchy-Green strain tensor is calculated from the flow-map as

$$C(\mathbf{r}; t_0, t_1) = [\nabla \phi_{t_0}^{t_1}]^T \nabla \phi_{t_0}^{t_1} \tag{3.5}$$

The backward FTLE field can be calculated using eq. (3.4) but using the backward flow-map. The ridges of the forward FTLE field correspond to repelling LCS or unstable manifolds and the ridges of the backward FTLE field correspond to the attracting LCS or stable manifolds.

An alternate approach to obtain the flow-maps and thus the FTLE fields [66, 67, 24] is to solve the PDE whose characteristics are the trajectories (eq. (3.1)) with initial conditions set to positions,

$$\begin{cases} \dfrac{\partial \psi(\mathbf{r},t)}{\partial t} + \mathbf{u}(\mathbf{r},t) \cdot \nabla \psi(\mathbf{r},t) = 0, \quad \mathbf{r} \in \mathcal{D}, t \in \mathcal{T} = [t_0, t_1] \\[2mm] \psi(\mathbf{r},0) = \psi_0(\mathbf{r}), \end{cases} \tag{3.6}$$

where ψ is actually the inverse flow-map $(\phi_{t_0}^{t_1})^{-1}$. So now in contrast to the ODE approach, forward time advection yields the backward flow-map whereas the advection backward in time yields the forward flow-map.

This approach (eq. (3.6)) is a more attractive option for computing the flow-map and the FTLE field than the trajectory approach (eq. (3.3)) because

1. the PDE can be solved using a finite-difference/finite-volume/finite-element method on a grid and hence the same resolution is obtained everywhere. (When using an ODE approach, the resolution is not uniform and depends on the particle density at the location. A higher resolution is obtained where particle density is high and a lower resolution where particle density is low.)

2. the PDE approach can be easily extended to the stochastic case and the DO methodology can be applied for a reduction in computational cost

In the stochastic case, we are given an ensemble of velocity fields $\mathbf{u}(\mathbf{r},t;\omega)$ and we wish to find the corresponding ensemble of flow-maps $\phi_{t_0}^t(\mathbf{r}_0;\omega)$. This could be obtained by solving the stochastic ODE

$$\begin{cases} \dot{\mathbf{r}} = \mathbf{u}(\mathbf{r},t;\omega) \\[2mm] \mathbf{r}(0) = \mathbf{r}_0, \end{cases} \tag{3.7}$$

or the stochastic PDE

$$\begin{cases} \dfrac{\partial \psi(\mathbf{r},t;\omega)}{\partial t} + \mathbf{u}(\mathbf{r},t;\omega) \cdot \nabla \psi(\mathbf{r},t;\omega) = 0, \quad \omega \in \Omega, \mathbf{r} \in \mathcal{D}, t \in \mathcal{T} = [t_0, t_1] \\[2mm] \psi(\mathbf{r},0;\omega) = \psi_0(\mathbf{r}) \end{cases} \tag{3.8}$$

using the Monte Carlo approach. However, it is more computationally amenable to solve the stochastic PDE using the DO methodology. The DO decomposition of the velocity field is denoted as

$$\mathbf{u}(\mathbf{r}, t; \omega) = \bar{\mathbf{u}}(\mathbf{r}, t) + \sum_{i=1}^{n_{s,u}} \tilde{\mathbf{u}}_i(\mathbf{r}, t) Y_i(t; \omega) \tag{3.9}$$

where $\bar{\mathbf{u}}$ is the velocity mean, $\tilde{\mathbf{u}}_i$ is the velocity of mode i, Y_i are the corresponding stochastic coefficients and $n_{s,u}$ is the number of modes retained in the DO decomposition. The DO decomposition of $\psi(\mathbf{r}, t; \omega)$ is denoted as

$$\psi(\mathbf{r}, t; \omega) = \bar{\psi}(\mathbf{r}, t) + \sum_{i=1}^{n_{s,\psi}} \tilde{\psi}_i(\mathbf{r}, t) Z_i(t; \omega) \tag{3.10}$$

where $\bar{\psi}$ is the mean, $\tilde{\psi}_i$ are the modes, ξ_i are the corresponding stochastic coefficients and $n_{s,\psi}$ is the number of modes retained. The resulting DO equations [23] are then

$$\begin{cases} \dfrac{\partial \bar{\psi}(\mathbf{r}, t)}{\partial t} = -\bar{\mathbf{u}} \cdot \nabla \bar{\psi} - \mathbb{C}_{Y_j Z_i} \tilde{\mathbf{u}}_j \cdot \nabla \tilde{\psi}_i \\[2mm] \dfrac{dZ_i(t; \omega)}{dt} = -\left\langle \tilde{\mathbf{u}}_j \cdot \nabla \tilde{\psi}_k (Y_j Z_k - \mathbb{C}_{Y_j Z_k}) + Y_j \tilde{\mathbf{u}}_j \cdot \nabla \bar{\psi} + Z_k \bar{\mathbf{u}} \cdot \nabla \tilde{\psi}_k, \tilde{\psi}_i \right\rangle \\[2mm] \dfrac{\partial \tilde{\psi}_i(\mathbf{r}, t)}{\partial t} = Q_i - \langle Q_i, \tilde{\psi}_m \rangle \tilde{\psi}_m \end{cases} \tag{3.11}$$

where

$$Q_i = -\mathbb{C}_{Z_j Z_i} \left[\mathbb{C}_{Z_j Y_k} \tilde{\mathbf{u}}_k \cdot \nabla \bar{\psi} + \mathbb{M}_{Z_j Y_k Z_i} \tilde{\mathbf{u}}_k \cdot \nabla \tilde{\psi}_i \right] - \bar{\mathbf{u}} \cdot \nabla \tilde{\psi}_i \tag{3.12}$$

with $\mathbb{C}_{a,b} = \mathbb{E}[ab]$ is the covariance between random variables a and b, and $\mathbb{M}_{abc} = \mathbb{E}[abc]$ is the third moment of the random variables a, b and c.

The above equations are a subset of the stochastic Hamilton Jacobi equation which have been previously solved by [113, 114] for optimal path planning in uncertain flow. Details of an efficient implementation of the DO methodology for solving the above system can be found in [24].

3.2 Problem Statement

Variables and Dynamical Models

The variables of interest can be categorized as *Eulerian* (e.g. velocity, temperature, salinity, density, pressure, etc.) and *Lagrangian* (e.g. drifter trajectories, flow-map, LCS, etc.). Many of these are prognostic variables i.e. we know how to evolve them through time using dynamical models. For example, velocity can be evolved using the Navier-Stokes equations. In ocean models, velocity, temperature, salinity, density and pressure may be evolved using primitive equations [37]. Other variables such as FTLE fields are diagnostic in nature as they are obtained from time-integrated information (eq. (3.4)) and not evolved through time. It should also be noted that unlike variables defined at a certain time t, the FTLE field is defined over a time interval. Suppose that $\mathbf{X}$ denotes the set of all prognostic and diagnostic variables we are interested in. In our work, this will primarily include velocity fields, flow-maps, drifter trajectories, and LCS.

Observations

Noisy observations of a subset of the Eulerian and/or Lagrangian variables are made available to us at times t_k, for $k = 1, 2, ..., K$. The variables in which observations are made may change from one time instance to another. For example, we may obtain observations in velocity at time t_1 and observations in temperature at time t_2. The noisy observations of a continuous stochastic field $X(\mathbf{r}, t; \omega)$ may be obtained through a linear (or linearized) observation model

$$\mathbf{Y}(t; \omega) = \mathbf{H}(t)\mathbf{X}(t; \omega) + \mathbf{\Gamma}(t; \omega), \quad \mathbf{\Gamma}(t; \omega) \sim \mathcal{N}(\cdot; \mathbf{0}, \mathbf{R}) \tag{3.13}$$

where $\mathbf{X}(t; \omega)$ is the spatially discretized vector of $X(\mathbf{r}, t; \omega)$, $\mathbf{Y}(t; \omega)$ are the noisy observations, $\mathbf{H}(t) \in \mathbb{R}^{N_{obs}(t) \times N_g(t)}$ denotes the observation matrix at time t, $\mathbf{\Gamma}$ is the zero-mean uncorrelated Gaussian measurement noise with covariance matrix $\mathbf{R}$, N_{obs} is the total number of observations made, and N_g is the total number of spatial grid points/cells. The argument t indicates that these parameters or matrices may change

with time. For brevity in notation, we will denote the variables in which we make observations at or after time t_k as $\mathbf{X}_k$ and the corresponding sparse noisy observations as $\mathbf{Y}_k$. In the case where the forward or backward FTLE field is observed at some locations, the observations can be associated to a time t_k but they actually correspond to FTLE data over a time interval, and they should be treated this way. That time interval would be $[t, t_k]$ with $t < t_k$ for forward FTLE data and $[t_k, t]$ with $t > t_k$ for backward FTLE data (observations are actually given available after t_k in that case).

Objective

Consider $\mathcal{T} = [t_0, t_N]$ as the time-interval of interest and let the observation times be t_k for $k = 1, 2, ..., K$ such that $t_0 < t_1 < t_2 < ... < t_K < t_N$. We aim to determine the posterior probability distribution function $p_{\mathbf{X}_k | \mathbf{Y}_{1:l}}$ i.e. the set of all prognostic (at time t_k) and diagnostic variables (e.g. FTLE over a time interval $[t, t_k]$) denoted by $\mathbf{X}_k$ conditioned on the observations $\mathbf{Y}_1, \mathbf{Y}_2, ..., \mathbf{Y}_k$. The filtering problem consists of computing $p_{\mathbf{X}_k | \mathbf{Y}_{1:k}}$ and the smoothing problem of computing $p_{\mathbf{X}_k | \mathbf{Y}_{1:l}}$ where $l > k$.

Having defined the problem that we are interested in solving, let us review some of the prior results and literature which looked at the problem of Lagrangian data assimilation.

3.3   Existing Methodologies and Challenges

Pseudo-Lagrangian schemes [1] [43, 47] were the first approaches to the problem of Lagrangian data assimilation. They use a finite difference approach to obtain a sequence of *Eulerian* velocity measurements which are then assimilated to improve the state variable of velocity fields. This approach becomes inaccurate when the time interval between subsequent measurements of drifter positions is comparable to the Lagrangian integral time-scale. However, the main disadvantage of this approach is that it ignores that the time series of drifter position measurements comes from a single trajectory.

---

[1] term coined by [82]

This issue can be circumvented by adopting a state-augmentation approach as in [46, 51] where drifter positions are augmented with velocity field. The augmented state is predicted using the evolution equations for velocity (e.g. Euler's, Navier-Stokes, linear shallow water equations, etc.) and the advection equation for drifter positions (eq. (3.7)). Drifter position observations (eq. (3.13)) can be directly assimilated to obtain the posterior PDF of the augmented state and hence, velocity fields are also updated according to the correlations of the drifter's movement with the velocity fields. The implementation in [51] which uses the extended Kalman filter for assimilation fails when observed trajectories pass too close to a saddle point of the flow. The same implementation [51] also uses the linear tangential model for uncertainty propagation which is not capable of capturing non-Gaussian PDFs of the state and requires the computationally expensive operation of evolving the error covariance matrix. The Ensemble Kalman Filter (EnKF) [20] has been combined with the state augmentation approach in [94] for the unsteady double-gyre flow setup with shallow water equations and in [128] to compare the assimilation of fixed *Eulerian* velocity measurements against assimilation of *Lagrangian* drifter positions for capturing the eddy-shedding process in the Gulf of Mexico.

Numerical experiments in [5, 4] indicate that variants of the Kalman filter such as EnKF are unsuitable for assimilation and a linearized dynamical model can not be used for prediction as they fail to capture non-Gaussian statistics of the state. This is apparent for the nonlinear equations of velocity 2.14) and advection equation for drifter positions (eq. (3.7)) where the variables quickly become non-Gaussian even when the initial PDF is a Gaussian. One solution would be to use the Particle Filter (PF) which is capable of capturing non-Gaussian PDFs but the required ensemble size grows exponentially with the size of the system and thus quickly becomes intractable for high-dimensional problems. A suggested remedy to these issues are hybrid filters such as the hybrid grid/particle filter (HGPF) [92, 93] and the hybrid particle-ensemble Kalman filter (HPEKF) [106]. The former (HGPF) uses an advection-diffusion equation to solve the Fokker-Planck equation associated with the augmented state vector which is computationally expensive for multiple drifters and

requires an application of a particle filter update to the flow variables (i.e. velocity) which becomes intractable for high-dimensional problems. The latter (HPEKF) overcomes this issues by resorting to a Monte Carlo approach for evolving the ensemble members and uses an EnKF for the usually high-dimensional flow (velocity) variables and a PF for the usually low-dimensional variables of drifter positions. For large ensemble sizes, a Monte Carlo approach for propagating uncertainty is inefficient and particle filters suffer from sampling impoverishment [107] which requires resampling procedures (e.g. Metropolis-Hastings method [19, 127], Gaussian resampling method [130]).

On the other hand, variational methods [50, 81, 116] minimize a cost function which measures the distance between model drifter and observed drifter trajectories. Variational methods have also been combined with the pseudo-Lagrangian scheme as in [117] where Argo float trajectories in the Mediterranean Sea were assimilated. Variational methods also propagate uncertainty using a linear forward model and hence cannot capture non-Gaussian statistics. Moreover, they typically provide a single estimate and not a description of the uncertainty (PDF) of the state.

Observation operator based approaches try to construct observation models that relate Lagrangian data to Eulerian variables. The observation models are not necessarily local in time and could be nonlinear. The pseudo-Lagrangian schemes which were discussed in the beginning of this section is an example of this approach as it tries to relate Lagrangian drifter positions to Eulerian gridded velocity field. The assimilation of subsurface Lagrangian data collected by periodically surfacing Lagrangian instruments (gliders) was carried out in [111] by constructing an observation operator for subsurface measurements made en route between surfacings. This allows for the correction of drifter paths as well when only subsurface measurements are available. The augmentation approach could not be used here for assimilating subsurface measurements because the measurement locations are unknown. [119] constructs adapted observation operators exploiting properties of the finite-time Lyapunov exponenet (FTLE) and finite-time Lyapunov vector (FTLV for direct assimilation of high-resolution satellite ocean tracers. The FTLE/FTLV realizations are obtained

from the satellite images using a binarization technique [120] and assimilation is used to improve velocity fields. In this work, we do not focus on assimilation of subsurface measurements and tracer images. This will be considered in the future.

In summary, any approach for Lagrangian data assimilation must overcome the following: (i) nonlinearity of the evolution equations which requires a method of uncertainty propagation and assimilation that is capable of capturing non-Gaussian statistics (ii) high dimensionality of flow variables (e.g. velocity), and (iii) spatial and temporal variability of the systems. Additionally, we would want the approach to be general and capable of joint assimilation of Eulerian and Lagrangian information content of observations.

3.4   State Augmentation Approach

For uncertainty propagation in the flow variables such as velocity or flow-map, we use the DO methodology which was described in Chapter 2. It has been shown to be capable of handling nonlinearities in dynamical equations and an efficient reduced order approach for high-dimensional problems. We combine the assimilation strategy of the state augmentation approach with the DO equations for forward evolution of the prognostic variables. The GMM-DO filter [109, 110] is used for assimilation. We review the filter in section 3.4.1 and explain how the Bayesian problem is solved during assimilation and how the non-Gaussian PDF of the posterior is accurately captured. It has been used previously for filtering [109, 110] and smoothing [76, 75] of velocity fields in idealized flow test cases. It has also been extended to model learning [77, 71] and simultaneous estimation of states, parameters and model equations with applications to coupled biogeochemical-physical flows [34]. Here, in this work we extend the GMM-DO filter for simultaneous estimation of Eulerian and Lagrangian variables which we will describe in section 3.4.2.

3.4.1 Gaussian Mixture Model (GMM)-DO Filter

From a Bayesian perspective, the goal of assimilation [98] is to obtain the posterior distribution $p(\mathbf{x}|\mathbf{y})$ of the state $\mathbf{x}$ given a prior distribution $p(\mathbf{x})$ on $\mathbf{x}$ which reflects the current knowledge of the state, and a likelihood distribution $p(\mathbf{y}|\mathbf{x})$ of the observations $\mathbf{y}$ given the state $\mathbf{x}$ based on our knowledge of noise in the observations. This is referred to as filtering if the observations $\mathbf{y}$ at time t_k are used to improve the knowledge of the state $\mathbf{x}$ at time t_k and is referred to as smoothing if they are used to improve the knowledge of state $\mathbf{x}$ at time $t < t_k$. The true posterior distribution is then given by Baye's rule:

$$p(\mathbf{x}|\mathbf{y}) = \frac{p(\mathbf{y}|\mathbf{x})p(\mathbf{x})}{p(\mathbf{y})} \tag{3.14}$$

In the GMM-DO filter [109, 110] and the GMM-DO smoother [76, 75], the PDF of the state of interest is evolved forward in time using the DO methodology. The prior state vector (also called forecast during filtering) can be written as

$$\mathbf{X}^f(\omega) = \bar{\mathbf{x}}^f + \tilde{\boldsymbol{\mathcal{X}}}^f \boldsymbol{\Phi}^f(\omega) \tag{3.15}$$

where $\bar{\mathbf{x}}^f$ is the mean of $\mathbf{X}^f(\omega)$, $\tilde{\boldsymbol{\mathcal{X}}}^f \in \mathbb{R}^{N_\mathbf{x} \times n_s}$ is the matrix containing the orthonormal modes, and $\boldsymbol{\Phi}^f(\omega) \in \mathbb{R}^{n_s \times 1}$ is a time-dependent vector of zero-mean stochastic coefficients. Assimilation is then carried out in the dominant stochastic subspace. The stochastic coefficients are represented using samples and thus the realizations in the state space can be obtained using the affine transformation (Eq. 3.15). The first step of the GMM-DO filter involves fitting a Gaussian Mixture Model (GMM) [80] to the samples of the stochastic coefficients.

$$p_{\boldsymbol{\Phi}}(\boldsymbol{\phi}) = \sum_{j=1}^{M} \pi_j^f \times \mathcal{N}(\boldsymbol{\phi}; \boldsymbol{\mu}_j^f, \boldsymbol{\Sigma}_j^f) \tag{3.16}$$

where the GMM parameters $\pi_j^f \in [0,1]$ is the weight of GMM component j and satisfies $\sum_{j=1}^{M} \pi_j^f = 1$, $\boldsymbol{\mu}_j^f \in \mathbb{R}^{n_s}$ is the mean of GMM component j, $\boldsymbol{\Sigma}_j^f$ is the covariance

matrix of GMM component j, and M is the the number of components in the GMM (also called complexity of the GMM). The GMM is fit to the realizations using the Expectation-Maximization algorithm [12] for a given complexity M. The Bayesian Information Criterion (BIC) is used to determine the most suitable value for M. Details regarding the application of the EM algorithm and BIC to obtain the GMM for a given set of realizations can be found in [109]. Combining eq. (3.16) and eq. (3.15), the PDF in the state space can be determined which is also a GMM

$$p_{\mathbf{X}}(\mathbf{x}) = \sum_{j=1}^{M} \pi_j^f \times \mathcal{N}(\mathbf{x}; \bar{\mathbf{x}}_j^f, \boldsymbol{P}_j^f) \tag{3.17}$$

where the corresponding GMM parameters are given by

$$\begin{cases} \bar{\mathbf{x}}_j^f = \bar{\mathbf{x}}^f + \tilde{\boldsymbol{\mathcal{X}}}^f \boldsymbol{\mu}_j^f \\ \boldsymbol{P}_j^f = \tilde{\boldsymbol{\mathcal{X}}}^f \Sigma_j^f (\tilde{\boldsymbol{\mathcal{X}}}^f)^T \end{cases} \tag{3.18}$$

The GMM is an attractive option for describing the PDF of the state vector as it is capable of capturing non-Gaussian statistics unlike the parameteric Gaussian PDF and does not require to retain the n_{MC} realizations unlike a kernel density estimator [105] which is computationally expensive for assimilation. Moreover, GMMs are conjugate priors [14, 108] to Gaussian observation models (eq. (3.13)). When solving eq. (3.14) during the assimilation to obtain the posterior distribution, the modes of the prior state vector (eq. (3.15)) are assumed to remain constant. Computing the posterior state vector then becomes equivalent to obtaining the parameters of GMM describing the posterior state. It was shown in [109] that this can be done in the stochastic subspace by finding the posterior distribution (GMM) over the stochastic coefficients which is much more computationally cheaper. We denote the parameters of the posterior state vector as

$$\mathbf{X}^a(\omega) = \bar{\mathbf{x}}^a + \tilde{\boldsymbol{\mathcal{X}}} \boldsymbol{\Phi}^a(\omega) \tag{3.19}$$

where the modes satisfy $\tilde{\mathcal{X}}^f = \tilde{\mathcal{X}}^a = \tilde{\mathcal{X}}$ and the corresponding GMM over $\Phi^a(\omega)$ as

$$\pi_j^a, \boldsymbol{\mu}_j^a, \Sigma_j^a, \quad j = 1, ..., M \tag{3.20}$$

The update equations [109] are as follows:

$$
\begin{cases}
\bar{\mathbf{x}}_j^a = \bar{\mathbf{x}}^f + \tilde{\mathcal{X}}^f \sum_{j=1}^{M} \pi_j^a \times \hat{\boldsymbol{\mu}}_j^a \\[2mm]
\pi_j^a = \dfrac{\pi_j^f \times \mathcal{N}(\tilde{\mathbf{y}}; \tilde{\mathbf{H}}\boldsymbol{\mu}_j^f, \tilde{\mathbf{H}}\Sigma_j^f \tilde{\mathbf{H}}^T + \mathbf{R})}{\sum\limits_{m=1}^{M} \pi_m^f \times \mathcal{N}(\tilde{\mathbf{y}}; \tilde{\mathbf{H}}\boldsymbol{\mu}_j^f, \tilde{\mathbf{H}}\Sigma_j^f \tilde{\mathbf{H}}^T + \mathbf{R})} \\[4mm]
\boldsymbol{\mu}_j^a = \hat{\boldsymbol{\mu}}_j^a - \sum\limits_{j=1}^{M} \pi_j^a \times \hat{\boldsymbol{\mu}}_j^a \\[2mm]
\Sigma_j^a = (\mathbf{I} - \tilde{\mathbf{K}}_j \tilde{\mathbf{H}})\Sigma_j^f
\end{cases}
\tag{3.21}
$$

with the following definitions

$$\tilde{\mathbf{H}} \equiv \mathbf{H}\tilde{\mathcal{X}} \tag{3.22a}$$

$$\tilde{\mathbf{y}} \equiv \mathbf{y} - \mathbf{H}\bar{\mathbf{x}}^f \tag{3.22b}$$

$$\hat{\boldsymbol{\mu}}_j^a \equiv \boldsymbol{\mu}_j^f + \tilde{\mathbf{K}}_j(\tilde{\mathbf{y}} - \tilde{\mathbf{H}}\boldsymbol{\mu}_j^f) \tag{3.22c}$$

$$\tilde{\mathbf{K}}_j \equiv \Sigma_j^f \tilde{\mathbf{H}}^T \left(\tilde{\mathbf{H}}\Sigma_j^f \tilde{\mathbf{H}}^T + \mathbf{R}\right)^{-1} \equiv \tilde{\mathcal{X}}\mathbf{K}_j \tag{3.22d}$$

where $\mathbf{K}_j$ is the Kalman gain matrix associated with GMM component j and $\hat{\boldsymbol{\mu}}_j^a$ is the intermediate mean vector of Φ^a. When eq. (3.14) is applied to the stochastic coefficients i.e. Φ^f, the intermediate posterior distribution of $\hat{\Phi}^a$ which is a GMM with parameters of π_j^a, $\hat{\boldsymbol{\mu}}_j^a$, and Σ_j^a for $j = 1, ..., M$ is obtained. The DO methodology requires that $\hat{\Phi}^a$ are zero-mean stochastic processes i.e. $\sum\limits_{j=1}^{M} \pi_j^a \boldsymbol{\mu}_j^a = 0$ which is not satisfied by $\hat{\boldsymbol{\mu}}_j^a$ in general.

After the posterior distribution of Φ^a is obtained, we can sample from the corresponding GMM to obtain the posterior set of realizations within the stochastic subspace. The procedure to obtain posterior state vector (eq. (3.19)) is then complete. Details regarding the derivation of the update equations (Eq. 3.21) can be

found in [109]. In the next section, we describe how the GMM-DO filter can be extended to include the assimilation of Lagrangian data.

3.4.2 Joint Eulerian-Lagrangian Data Assimilation

In general, we can augment the state as

$$\mathbf{X} = \begin{bmatrix} \text{Eulerian Variables} \\ \text{Lagrangian Variables} \end{bmatrix} \tag{3.23}$$

As explained earlier in section 3.2, some of these variables have dynamical equations attached to them which we referred to as prognostic variables. The state vector can then be rewritten also as

$$\mathbf{X} = \begin{bmatrix} \text{Prognostic Variables} \\ \text{Diagnostic Variables} \end{bmatrix} = \begin{bmatrix} \mathbf{X}_{PV} \\ \mathbf{X}_{DV} \end{bmatrix} \tag{3.24}$$

The prognostic variables are evolved using their corresponding dynamical equations and the diagnostic variables are usually determined from the time-integrated prognostic variables. Diagnostic variables include trajectories ($\mathcal{T} = \{\mathbf{x}_P(t;\omega)|t \in [t_0, t_1]\}$) which is set of all positions lying along the drifter path and FTLE Λ which are computed from the stochastic flow-maps. For example, if we consider the augmented state vector containing Eulerian velocity $\mathbf{u}$ and Lagrangian drifter positions $\mathbf{x}_P$, flow-maps Ψ, and FTLE Λ.

$$\mathbf{X} = \begin{bmatrix} \mathbf{u} \\ \mathbf{x}_P \\ \Psi \\ \Lambda \end{bmatrix} \tag{3.25}$$

The prognostic variables are velocity, drifter positions, and flow-maps which can be evolved with eq. (2.14), eq. (3.7), and eq. (3.8) respectively. Effectively, the dynamical

equations of $\mathbf{X}_{PV}$ are augmented together.

$$\mathcal{L}(\mathbf{X}_{PV}) = \begin{bmatrix} \mathcal{L}(\mathbf{u}) \\ \mathcal{L}(\mathbf{x}_P) \\ \mathcal{L}(\mathbf{\Psi}) \end{bmatrix} \tag{3.26}$$

The diagnostic variable of FTLE is calculated using eq. (3.4). Velocity and the flow-map can be computed efficiently using the DO methodology (equations in section 2.1.2 and eq. (3.11) respectively). The positions of the drifters are evolved in a Monte Carlo fashion using the ensemble realizations of the velocity

$$\frac{d\mathbf{x}_P(t;\omega)}{dt} = \mathbf{u}(\mathbf{x}_P(t;\omega), t;\omega) = \bar{\mathbf{u}}(\mathbf{x}_P(t;\omega), t) + \sum_{i=1}^{n_{s,u}} \tilde{\mathbf{u}}_i(\mathbf{x}_P(t;\omega), t)Y_i(t;\omega) \tag{3.27}$$

where we inserted the DO decomposition of the velocity (eq. (3.9)). The trajectories can also be obtained from the forward flow-map. For example, the ensemble of trajectories corresponding to a drifter released from $\mathbf{z}_P$ would be given by

$$\begin{cases} \mathbf{x}_P(t;\omega) = \bar{\phi}(\mathbf{z}_P, t) + \sum_{i=1}^{n_{s,\Psi}} \tilde{\phi}_i(\mathbf{z}_P, t)Z_i(t;\omega) \\ \mathbf{x}_P(t=0;\omega) = \mathbf{z}_P \end{cases} \tag{3.28}$$

where the DO decomposition of the forward flow-map in the above equation was obtained from backward time-integration of $\mathbf{\Psi}$ (or eq. (3.10)) in eq. (3.11). It should be noted that there may be slight differences in the trajectories obtained using eq. (3.27) and eq. (3.28) due to numerical errors. We decompose the drifter positions $\mathbf{x}_P$ into it's mean $\bar{\mathbf{x}}_P$ and deviation $\mathbf{E}_P$.

$$\mathbf{x}_P(t;\omega) = \bar{\mathbf{x}}_P(t) + \mathbf{E}_P(t;\omega) \tag{3.29}$$

Once all the prognostic variables have been computed, the diagnostic variable such as FTLE may be determined form the time integrated information. The DO decomposition of the FTLE is obtained by taking the SVD of the ensemble realizations of

85

FTLE determined from the ensemble realizations of flow-maps using eq. (3.4). The DO decomposition of the FTLE will be denoted by

$$\Lambda(\mathbf{r};\omega) = \bar{\Lambda}(\mathbf{r};\omega) + \sum_{i=1}^{n_{s,\Lambda}} \tilde{\Lambda}_i(\mathbf{r},t) B_i(t;\omega) \tag{3.30}$$

After all the prognostic variables available at the time of interest t_k and diagnostic variables at time of interest or time interval of interest, we augment the variables to obtain the augmented vector (eq. (3.25)) and the associated DO decomposition

$$\mathbf{X}(\omega) = \begin{bmatrix} \mathbf{u}(\omega) \\ \mathbf{x}_P(\omega) \\ \mathbf{\Psi}(\omega) \\ \Lambda(\omega) \end{bmatrix} = \underbrace{\begin{bmatrix} \bar{\mathbf{u}} \\ \bar{\mathbf{x}}_P \\ \bar{\mathbf{\Psi}} \\ \bar{\Lambda} \end{bmatrix}}_{:=\bar{\mathbf{X}}} + \underbrace{\begin{bmatrix} \tilde{\mathbf{u}} & 0 & 0 & 0 \\ 0 & \mathbf{I}_{N_P} & 0 & 0 \\ 0 & 0 & \tilde{\mathbf{\Psi}} & 0 \\ 0 & 0 & 0 & \tilde{\Lambda} \end{bmatrix}}_{:=\tilde{\mathcal{X}}} \times \underbrace{\begin{bmatrix} \mathbf{Y}(\omega) \\ \mathbf{E}_P(\omega) \\ \mathbf{Z}(\omega) \\ \mathbf{B}(\omega) \end{bmatrix}}_{:=\Phi(\omega)} \tag{3.31}$$

where $\mathbf{I}_{N_P}$ is an identity matrix of size $2N_P \times 2N_P$ when working in 2D with N_P denoting the number of drifters, and $\tilde{\mathbf{u}}$ is the modes' matrix for velocity where the ith column is the ith DO mode $\tilde{\mathbf{u}}_i$. The mode matrices of flow-map and FTLE are denoted by $\tilde{\mathbf{\Psi}}$ and $\tilde{\Lambda}$ respectively. The reduced order decomposition of $\mathbf{X}$ is a valid DO decomposition because the modes of the augmented state vector are orthonormal with respect to the inner product defined by $\tilde{\mathcal{X}}^T \Lambda_{IP} \tilde{\mathcal{X}} = \mathbf{I}$ (eq. (2.62)) and exactly reproduces the individual realizations of the variables in the state vector.

In eq. (3.31), the uncertainty is explained by $\tilde{\mathcal{X}}\Phi(\omega)$. If we consider the entire set of realizations, then the matrix can be denoted as $\tilde{\mathcal{X}}\Phi^T$. It is important to note two things at this stage. Firstly, $\tilde{\mathcal{X}}\Phi^T$ is the exact representation of the DO realizations but is a low-rank expansion of the entire set of MC realizations which are a part of the uncertainty. It may not necessarily be the best low-rank expansion. This brings us to the second point. If we were to take an SVD of the set of MC realizations, we would have obtained a matrix of modes $\hat{\mathcal{X}}$ that may be a better representation of the uncertainty as the modes would not only capture correlations in a single variable but also the cross-correlations between variables. The stochastic

86

coefficients $\hat{\Phi}$ would now be shared. A disadvantage may be that the sparsity in $\tilde{\mathcal{X}}$ may be lost. A particular advantage is that there is a possibility of having a lower rank modes matrix to describe the same uncertainty. Here, the DO realizations are available in place of the MC realizations. It may still be advantageous to obtain the best low-rank expansion of the DO solution as it ensures that the coefficients are shared between the different variables and $\hat{\mathcal{X}}$ may have a smaller rank than $\tilde{\mathcal{X}}$. It can also be truncated to have a smaller rank but still represent nearly all the uncertainty. Instead of taking an SVD of the reconstructed DO realizations to obtain the best low-rank expansion, we apply an alternate procedure.

It should be noted that $\tilde{\mathcal{X}}\Phi^T = \hat{\mathcal{X}}\hat{\Phi}^T$ as they represent the same realizations. Let us denote this resulting matrix as $\mathbf{A}$ and the eigendecomposition of $\mathbf{AA}^T = \mathbf{PQP}^T$. The matrices $\hat{\mathcal{X}}$ and $\hat{\Phi}$ can then be obtained through

$$\hat{\mathcal{X}} = \tilde{\mathcal{X}}\mathbf{P}; \quad \hat{\Phi}^T = \mathbf{P}^T\Phi^T \tag{3.32}$$

It can be checked that the resulting modes are orthonormal ($\mathbf{G} = \hat{\mathcal{X}}\Lambda_{IP}\hat{\mathcal{X}} = \mathbf{P}^T\tilde{\mathcal{X}}\Lambda_{IP}\tilde{\mathcal{X}}\mathbf{P} = \mathbf{I}$). Truncation is carried out by looking at $\mathbf{Q}$ according to the amount of uncertainty one wants to capture.

After the augmented state vector is created, the Baye's formula (eq. (3.14)) is solved using the GMM-DO filter as discussed in section 3.4.1 to obtain the posterior distribution of the state vector. The key thing here is that we fit a GMM to the stochastic coefficients Φ. In the case of eq. (3.31), we then obtain the joint prior distribution for the augmented stochastic coefficients and the prior distribution of the shared coefficients in eq. (3.32). In the observation model (eq. (3.13)),

$$\mathbf{Y}(t;\omega) = \mathbf{H}(t)\mathbf{X}(t;\omega) + \mathbf{\Gamma}(t;\omega), \quad \mathbf{\Gamma}(t;\omega) \sim \mathcal{N}(\cdot;\mathbf{0},\mathbf{R}) \tag{3.33}$$

the observation operator (measurement model) $\mathbf{H}(t)$ which projects the state space onto the observation space is a simple projection matrix. The elements of the matrix can only be 0 or 1. For example, if we only had observations in drifter trajectories, the observation operator would be given by $\mathbf{H}(t) = (\mathbf{0},\mathbf{I},\mathbf{0},\mathbf{0})$ where $\mathbf{I}$ is a unit matrix.

87

The posterior distribution can then be obtained using the GMM-DO update of Eq. 3.21.

To understand how observations in a Lagrangian (Eulerian) variable also helps in improving our knowledge in the Eulerian (Lagrangian) variable, let us consider a simpler example. Suppose that the augmented state vector contains only velocity and FTLE. The DO decomposition is then given by

$$\underbrace{\begin{bmatrix} \mathbf{u}(\omega) \\ \Lambda(\omega) \end{bmatrix}}_{:=\mathbf{X}(\omega)} = \underbrace{\begin{bmatrix} \bar{\mathbf{u}} \\ \bar{\Lambda} \end{bmatrix}}_{:=\bar{\mathbf{X}}} + \underbrace{\begin{bmatrix} \tilde{\mathbf{u}} & 0 \\ 0 & \tilde{\Lambda} \end{bmatrix}}_{:=\tilde{\mathcal{X}}} \times \underbrace{\begin{bmatrix} \mathbf{Y}(\omega) \\ \mathbf{B}(\omega) \end{bmatrix}}_{:=\hat{\Phi}(\omega)} \tag{3.34}$$

considering the first augmentation approach. The PDF of the GMM that is fit to the joint realizations of $[Y(\omega), B(\omega)]$ is

$$p_{\Phi}(\phi) = p_{\mathbf{Y},\mathbf{B}}(Y, B) = \sum_{j=1}^{M} \pi^j \times \mathcal{N}\left(\begin{bmatrix} Y \\ B \end{bmatrix} ; \begin{bmatrix} \bar{\mu}_{\mathbf{Y}}^j \\ \bar{\mu}_{\mathbf{B}}^j \end{bmatrix} , \begin{bmatrix} \Sigma_{\mathbf{Y},\mathbf{Y}}^j & \Sigma_{\mathbf{Y},\mathbf{B}}^j \\ \Sigma_{\mathbf{B},\mathbf{Y}}^j & \Sigma_{\mathbf{B},\mathbf{B}}^j \end{bmatrix} \right) \tag{3.35}$$

Using the above joint PDF $p_{\mathbf{Y},\mathbf{B}}$ and the joint affine transformation (eq. (3.34)), we can determine the joint state-space PDF $p_{\mathbf{u},\Lambda}$ which is also a GMM given by

$$p_{\mathbf{X}}(\mathbf{x}) := p_{\mathbf{u},\Lambda}(u, \lambda) = \sum_{j=1}^{M} \pi^j \times \mathcal{N}\left(\begin{bmatrix} u \\ \lambda \end{bmatrix} ; \begin{bmatrix} \bar{\mathbf{u}} + \tilde{\mathbf{u}}\bar{\mu}_{\mathbf{Y}}^j \\ \bar{\Lambda} + \tilde{\Lambda}\bar{\mu}_{\mathbf{B}}^j \end{bmatrix} , \begin{bmatrix} \tilde{\mathbf{u}}\Sigma_{\mathbf{Y},\mathbf{Y}}^j\tilde{\mathbf{u}}^{\mathsf{T}} & \tilde{\mathbf{u}}\Sigma_{\mathbf{Y},\mathbf{B}}^j\tilde{\Lambda}^{\mathsf{T}} \\ \tilde{\Lambda}\Sigma_{\mathbf{B},\mathbf{Y}}^j\tilde{\mathbf{u}}^{\mathsf{T}} & \tilde{\Lambda}\Sigma_{\mathbf{B},\mathbf{B}}^j\tilde{\Lambda}^{\mathsf{T}} \end{bmatrix} \right)$$
$$\tag{3.36}$$

If we now consider the case where only velocity measurements are made, the linear observation model can then be written as $\mathbf{H} = [\mathbf{I}_{\mathbf{u}}, \mathbf{0}]$ where $\mathbf{I}_{\mathbf{u}}$ is an unit matrix with entries of 1 according to the location where the observation in velocity is made. According to the GMM-DO update equations (eq. (3.21)), the Kalman gain matrix for each mixture component in the GMM (eq. (3.35) is given by

$$\tilde{K}^j = \begin{bmatrix} \Sigma_{\mathbf{Y},\mathbf{Y}}^j\tilde{\mathbf{u}}^{\mathsf{T}}\mathbf{I}_{\mathbf{u}}^{\mathsf{T}} \\ \Sigma_{\mathbf{B},\mathbf{Y}}^j\tilde{\mathbf{u}}^{\mathsf{T}}\mathbf{I}_{\mathbf{u}}^{\mathsf{T}} \end{bmatrix} \left(\mathbf{I}_{\mathbf{u}}^{\mathsf{T}}\tilde{\mathbf{u}}\Sigma_{\mathbf{Y},\mathbf{Y}}^j\tilde{\mathbf{u}}^{\mathsf{T}}\mathbf{I}_{\mathbf{u}}^{\mathsf{T}} + \mathbf{R} \right)^{-1} \tag{3.37}$$

where the mean, covariance matrix and weight for each component of the posterior GMM in the joint stochastic subspace are

$$\hat{\boldsymbol{\mu}}^j = \bar{\boldsymbol{\mu}}^j + \tilde{\mathbf{K}}^j \left(\tilde{\mathbf{y}} - \tilde{\mathbf{H}} \bar{\boldsymbol{\mu}}^j \right) \tag{3.38}$$

$$\hat{\boldsymbol{\Sigma}}^j = \left(\mathbf{I} - \tilde{\mathbf{K}}^j \tilde{\mathbf{H}} \right) \boldsymbol{\Sigma}^j \tag{3.39}$$

$$\hat{\pi}^j \propto \pi^j \times \mathcal{N}(\tilde{\mathbf{y}}; \bar{\boldsymbol{\mu}}^j, \mathbf{I}_{\mathbf{u}}^\mathsf{T} \tilde{\mathbf{u}} \boldsymbol{\Sigma}_{\mathbf{Y},\mathbf{Y}}^j \tilde{\mathbf{u}}^\mathsf{T} \mathbf{I}_{\mathbf{u}}^\mathsf{T} + \mathbf{R}), \quad \sum_{m=1}^{M} \hat{\pi}^m = 1 \tag{3.40}$$

From eq. (3.37), we see that our knowledge in the Lagrangian variable improves as a consequence of the cross-correlations in each GMM component. We can then generally say that the mutual information between the observational data and the variables in the augmented state allows us to improve our knowledge. We illustrate using the same augmented state through a simple application in the following section.

3.5   Application: Stochastic Double-Gyre Flow

Here, we consider the stochastic case of the periodically varying double-gyre flow [100] which was described in [23, 24]. The stream function of the stochastic flow is given by

$$\psi(x, y, t; \omega) = A \sin(\pi f(x, t; \omega)) \sin(\pi y) \tag{3.41}$$

where

$$\begin{cases} f(x, t; \omega) = a(t; \omega)x^2 + b(t; \omega)x \\ a(t; \omega) = \epsilon \sin(\omega t) \\ b(t; \omega) = 1 - 2\epsilon \sin(\omega t) \end{cases} \tag{3.42}$$

where the stochasticity is introduced through the variable ω which is the angular frequency of the oscillations. Here, we consider $\omega \sim \mathcal{U}[\pi/10, 8\pi/10]$. The parameter ϵ is approximately how far the line separating the two vortices moves left or right from the center line. The flow is divergence free (i.e. $\nabla \cdot \mathbf{u}$) for any value of ω or ϵ. It should however be noted that this is not a solution to the stochastic Navier-Stokes equations (eq. (2.14)). Velocity is already known as a function of time and thus does not need

89

to be dynamically evolved. The DO decomposition of velocity $\mathbf{u}$ is shown in Figure 3-1 at $T = 5$. We find that four modes is enough to explain 99.9% of the uncertainty at all time instances. This is reflected by the exponential decay of variance of the stochastic coefficients in Figure 3-1. The prognostic variable of flow-map is evolved using eq. (3.8). Here, we choose to evolve the backward flow-map from $T = 10$ to $T = 0$ which marks the temporal domain of interest. The DO decomposition of the stochastic backward flow-map is shown in Figure 3-2. The stochastic backward FTLE field is obtained using eq. (3.4) and the DO decomposition (Figure 3-3) using an SVD approach. We consider the augmented state vector as $(\mathbf{u}(\omega), \Lambda(\omega))^T$. It should be noted the stochastic backward flow-map is not included as a part of the augmented state vector but needs to be if we also want to update our knowledge in that variable as well.
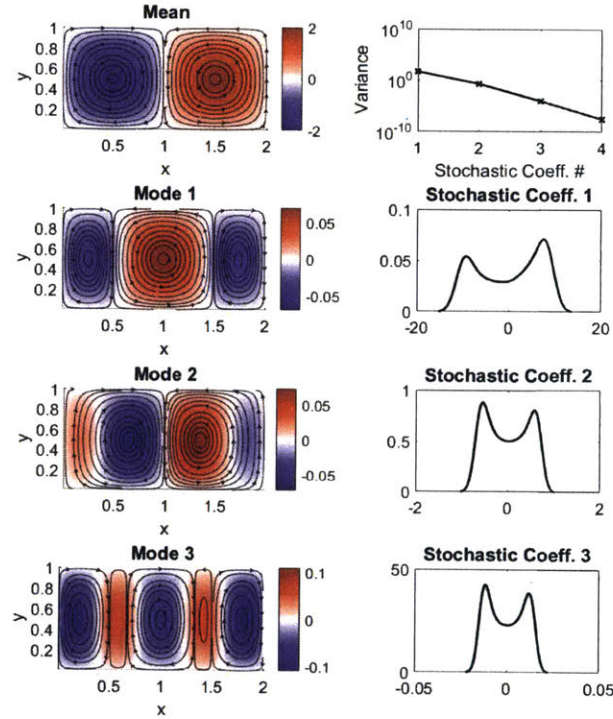
Figure 3-1: Stochastic double-gyre flow at $T = 5$. (left) Vorticity of DO mean and the first three modes of velocity depicted using streamslices with magnitude of the velocity in the background with (right) Spectrum of the stochastic coefficients (top row) followed by the kernel density estimates of the marginal PDFs of the stochastic coefficients

We consider two test cases: (i) observations in the Lagrangian FTLE is used to improve the knowledge in both $\mathbf{u}$ and Λ, and (ii) observations in the Eulerian velocity is used to improve the knowledge in both $\mathbf{u}$ and Λ.
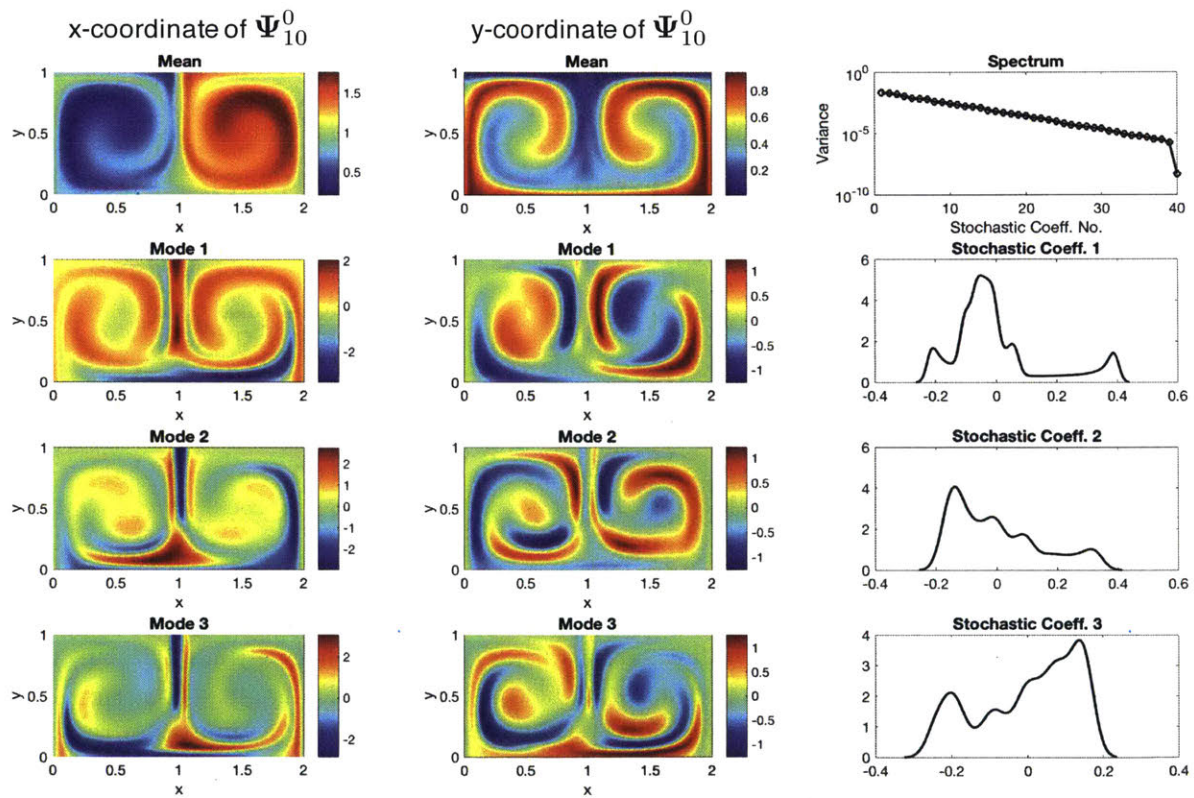
Figure 3-2: Stochastic double-gyre flow: Stochastic backward flow-map between $T = 10$ and $T = 0$. (first two columns) DO mean and the first three dominant modes of backward flow-map with (third column) Spectrum of the stochastic coefficients (top row) followed by the kernel density estimates of the marginal PDFs of the stochastic coefficients
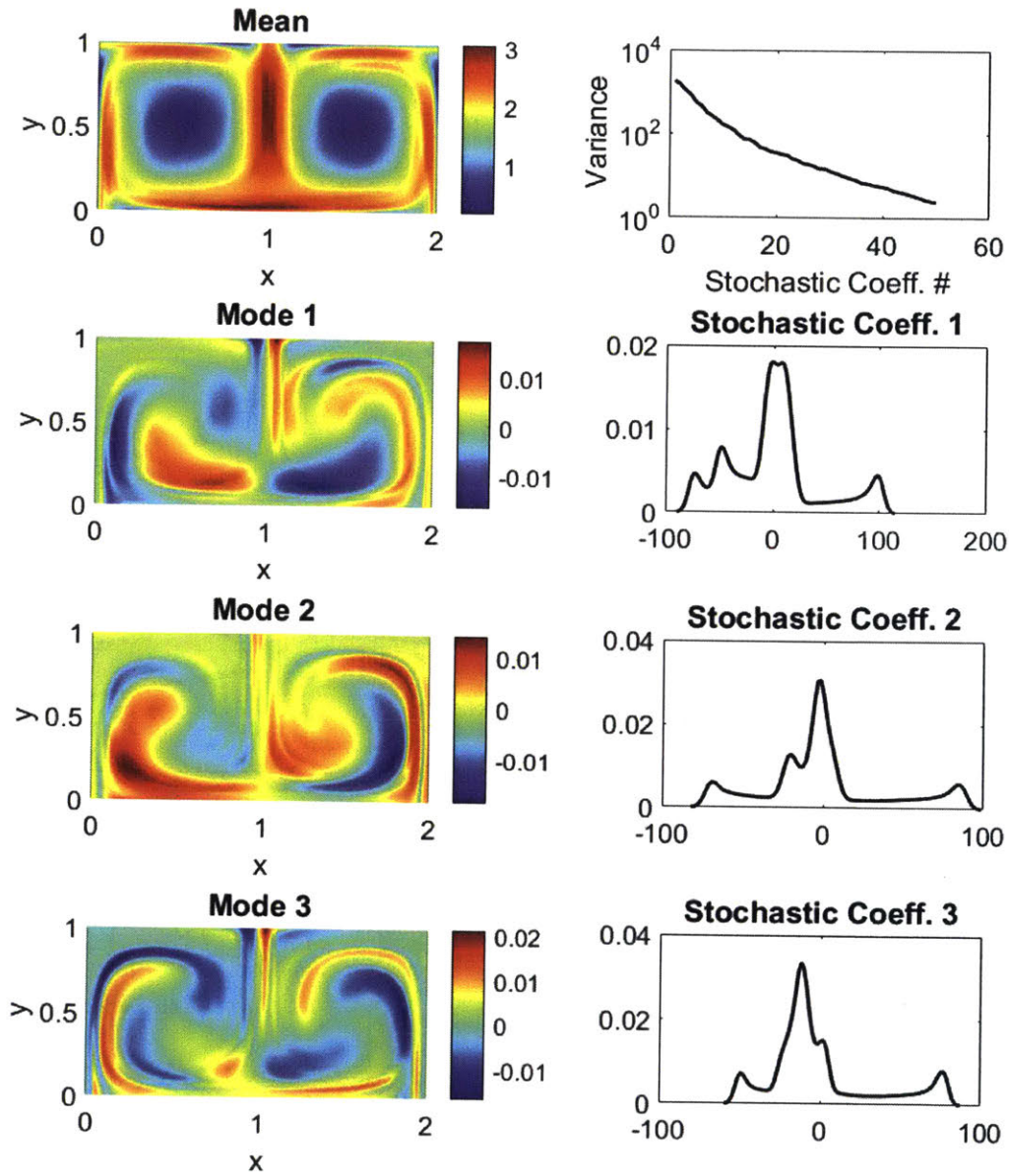
Figure 3-3: Stochastic double-gyre flow: backward FTLE between $T = 10$ and $T = 0$. (left) DO mean and the first three modes of backward FTLE with (right) Spectrum of the stochastic coefficients (top row) followed by the kernel density estimates of the marginal PDFs of the stochastic coefficients

Test Case 1: Observations in Lagrangian FTLE

We follow a twin experiment approach where the truth is selected to be one of the realizations belonging to the statistics of the DO decomposition of FTLE. We start

off with the test case where only observations in FTLE are made at four locations marked by stars in Figure 3-4. Velocity is not observed. The measurement noise in eq. (3.33) corresponding to the FTLE observations is set to zero-mean Gaussian with variance of $2\sigma_\Lambda^2$ where σ_Λ^2 is the global average variance of the FTLE field.

(a) Backward FTLE   (b) Velocity   (c) Distribution of Stochastic Coefficients

Figure 3-4: Stochastic double-gyre flow: Observations in backward FTLE are used to update the knowledge of both the Lagrangian FTLE and the Eulerian velocity. (left) Prior DO mean, true realization of FTLE (with observation locations marked by stars) and the posterior DO mean of FTLE; (center) Prior DO mean, true realization of velocity (no observations were made in this variable) and the posterior DO mean of velocity; (right) Prior and posterior distributions of the corresponding stochastic coefficients with the coefficient of the truth marked.

In Figure 3-4, we have plotted the prior DO means of the FTLE field and the velocity. Results of the assimilation are shown by plotting the posterior DO means of the FTLE field and velocity in Figure 3-4, the marginal distributions of the stochastic coefficients corresponding to the first three modes in the same Figure, and the marginal distributions (in one and two dimensions) of the stochastic coefficients in Figure 3-5. The posterior distributions of the first three coefficients show improvements with modes in the PDFs centered at the coefficient of the true solution. This is

93

more clear in Figure 3-5 where we can see that Gaussian components of the posterior GMM with high weights are closer to the true solution. Further, we plot the PDFs of the variables at the observations locations in Figure 3-6. There were no observations made in velocity but we are still able to improve our knowledge in this variable through the state augmentation approach as reflected in the posterior distributions. This shows how information in one variable can be captured to improve knowledge of another variable.

Figure 3-5: Joint GMM fits considering observations in Lagrangian FTLE. In the four boxes, we show pairwise joint distributions of two stochastic coefficients. Ensemble members representing the prior are shown in blue along with the prior and posterior GMM fits. One standard-deviation contours of the different Gaussian components are displayed and colored by the weight of the component i.e. π_j^f for the prior GMM (see colorbar on the left) and π_j^a for the posterior GMM (see colorbar on the right). The 1D marginal densities of the prior are computed by a kernel dressing scheme and are shown in blue. The marginal prior and posterior PDFs of each stochastic coefficient as obtained through the GMM fits are also plotted (see legend for color association).

94

(a) u velocity   (b) v velocity   (c) FTLE

Figure 3-6: Distributions of the different variables at the observation locations (left) Prior distribution, posterior distribution and true solution of u velocity which is not observed; (center) Prior distribution, posterior distribution and true solution of v velocity which is not observed; (right) Prior distribution, observation with it's associated Gaussian distribution, true solution and posterior distribution of FTLE

Test Case 2: Observations in Eulerian Velocity

As before, we follow a twin experiment approach where the truth is selected to be one of the realizations belonging to the statistics of the DO decomposition of FTLE. The observation locations which were selected in the last test case are considered again but now observations are made in Eulerian velocity. The measurement noise in eq. (3.33) corresponding to observations u_x and u_y is set to zero-mean Gaussian with variance of $2\sigma^2_{u_x}$ and $2\sigma^2_{u_y}$ respectively where $\sigma^2_{u_x}$ and $\sigma^2_{u_x}$ are the global average variances of u_x and u_y respectively.

We organize our results in a similar manner to that in the previous test case. In Figure 3-7, we have plotted the prior DO means of the FTLE field and the velocity. Results of the assimilation are shown by plotting the posterior DO means of the FTLE field and velocity in Figure 3-7, the marginal distributions of the stochastic coefficients corresponding to the first three modes in the same Figure, and the marginal

(a) Backward FTLE   (b) Velocity   (c) Distribution of Stochastic Coefficients
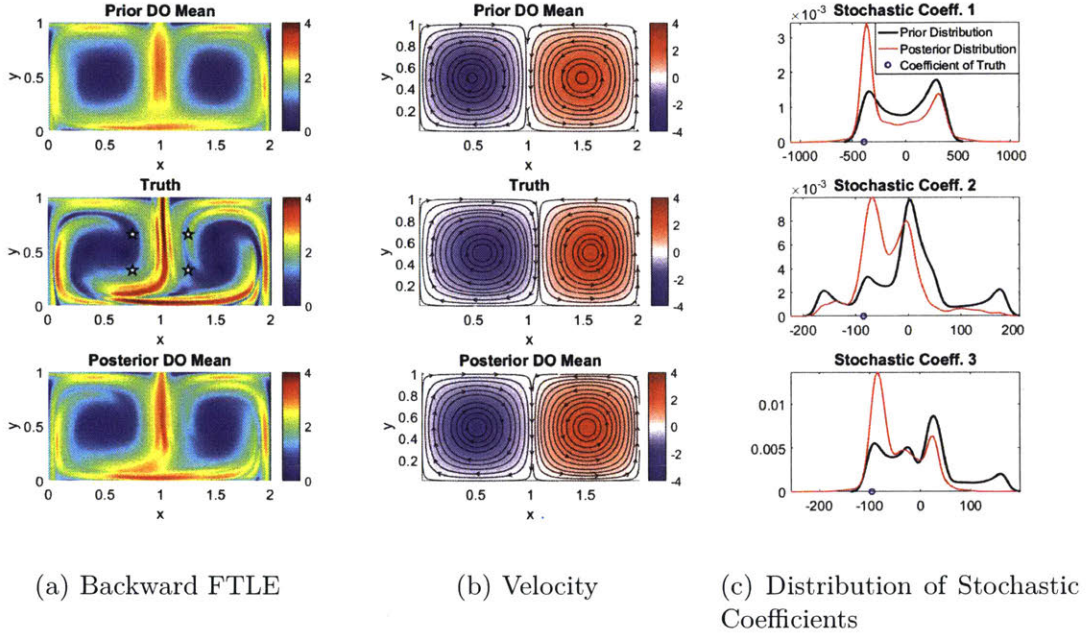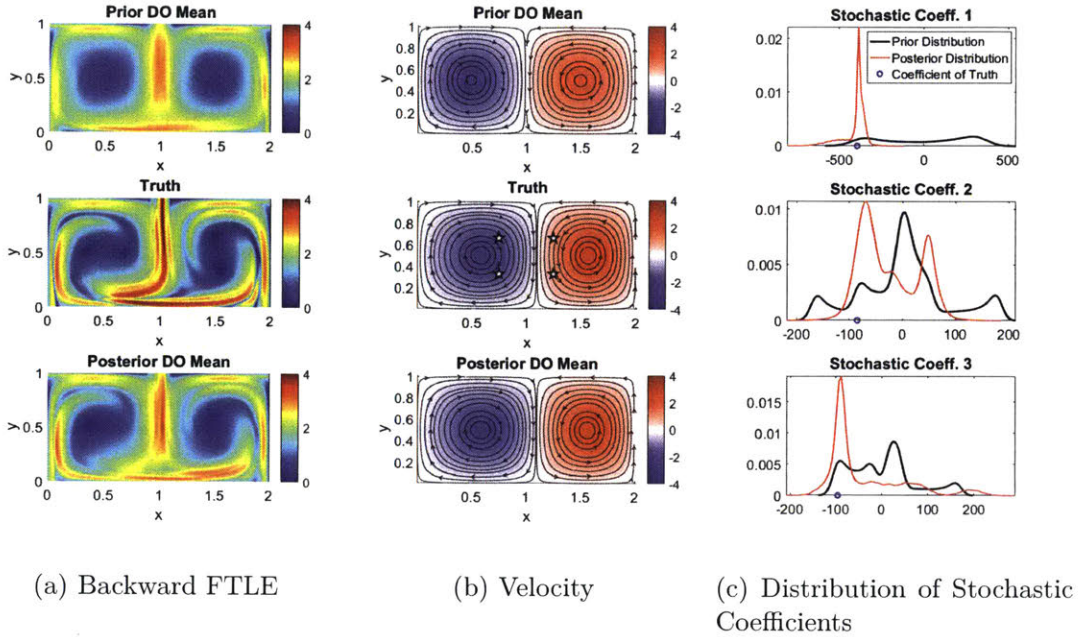
Figure 3-7: Stochastic double-gyre flow: Observations in velocity (both components) are used to update the knowledge of both the Lagrangian FTLE and the Eulerian velocity. (left) Prior DO mean, true realization of FTLE (no observations are made in this variable) and the posterior DO mean of FTLE; (center) Prior DO mean, true realization of velocity (observation locations are marked by stars) and the posterior DO mean of velocity; (right) Prior and posterior distributions of the corresponding stochastic coefficients with the coefficient of the truth. marked

distributions (in one and two dimensions) of the stochastic coefficients in Figure 3-8. The posterior distributions of the first three coefficients show improvements with modes in the PDFs centered at the coefficient of the true solution. We notice that the uncertainty in the stochastic coefficients is reduced to a greater degree compared to the previous case. This is more clear in Figure 3-8 where we can see that Gaussian components of the posterior GMM with high weights move towards the true solution. The prior and posterior PDFs of the velocity components are plotted in Figure 3-9 at the observation locations. Comparing this against the corresponding distributions in Figure 3-6 where FTLE observations were assimilated, we can conclude that velocity observations are more informative for the random variables of velocity at these locations. This is expected due to the higher mutual information between the PDFs

of the observation and verification variable in this case. FTLE observations could be more informative if the observation noise in velocity was much higher than the observation noise in FTLE.
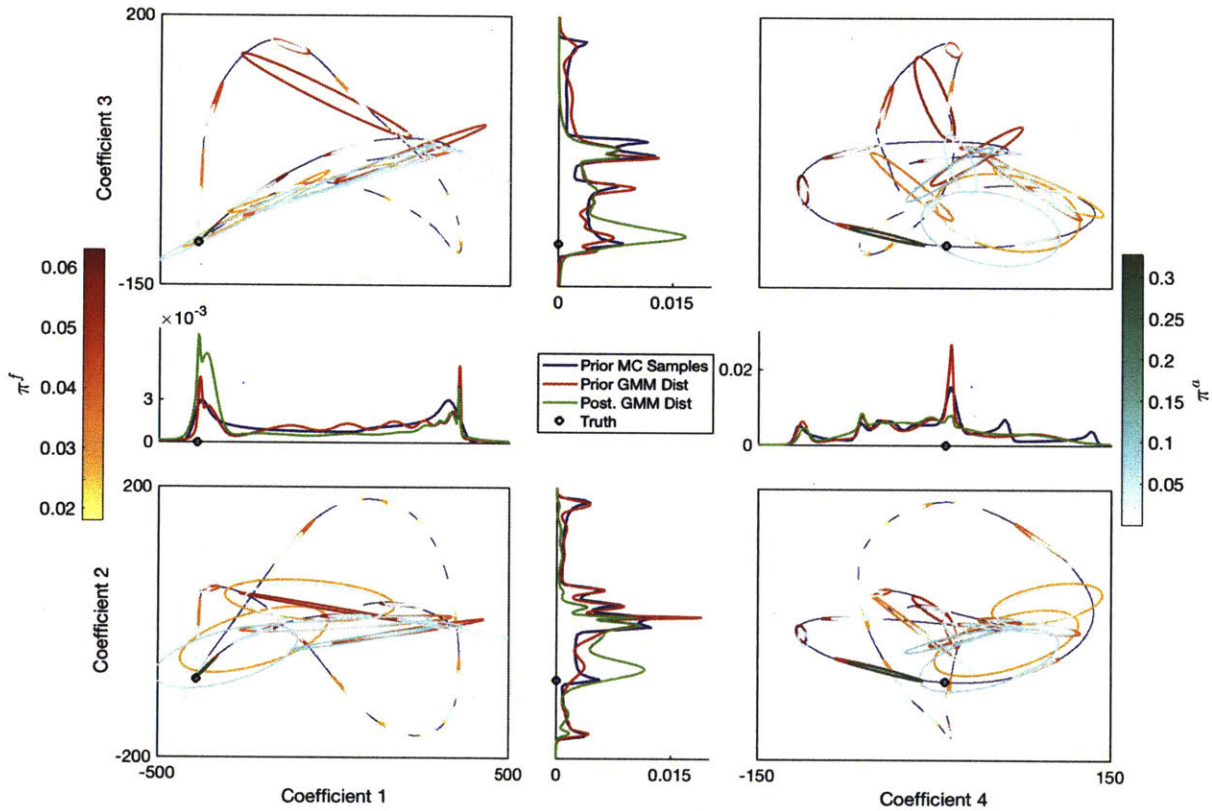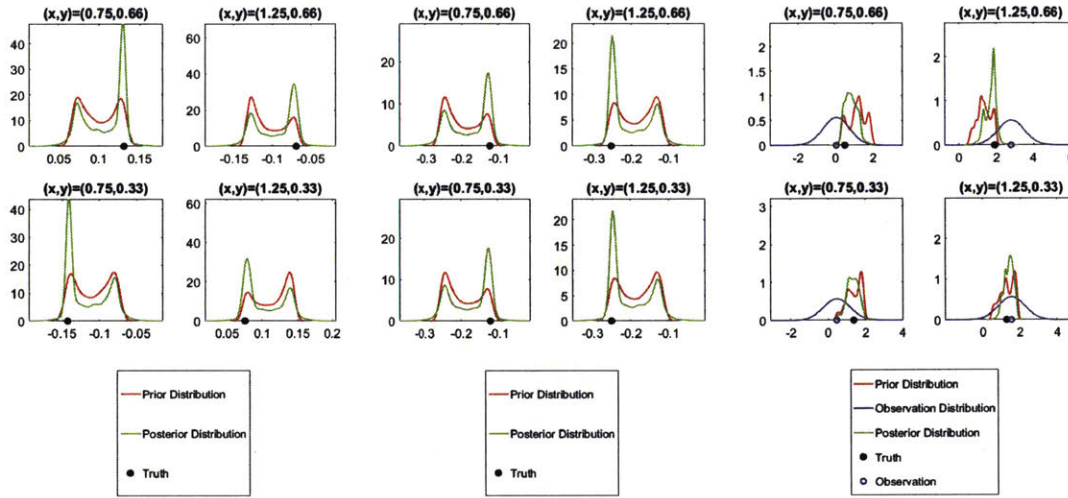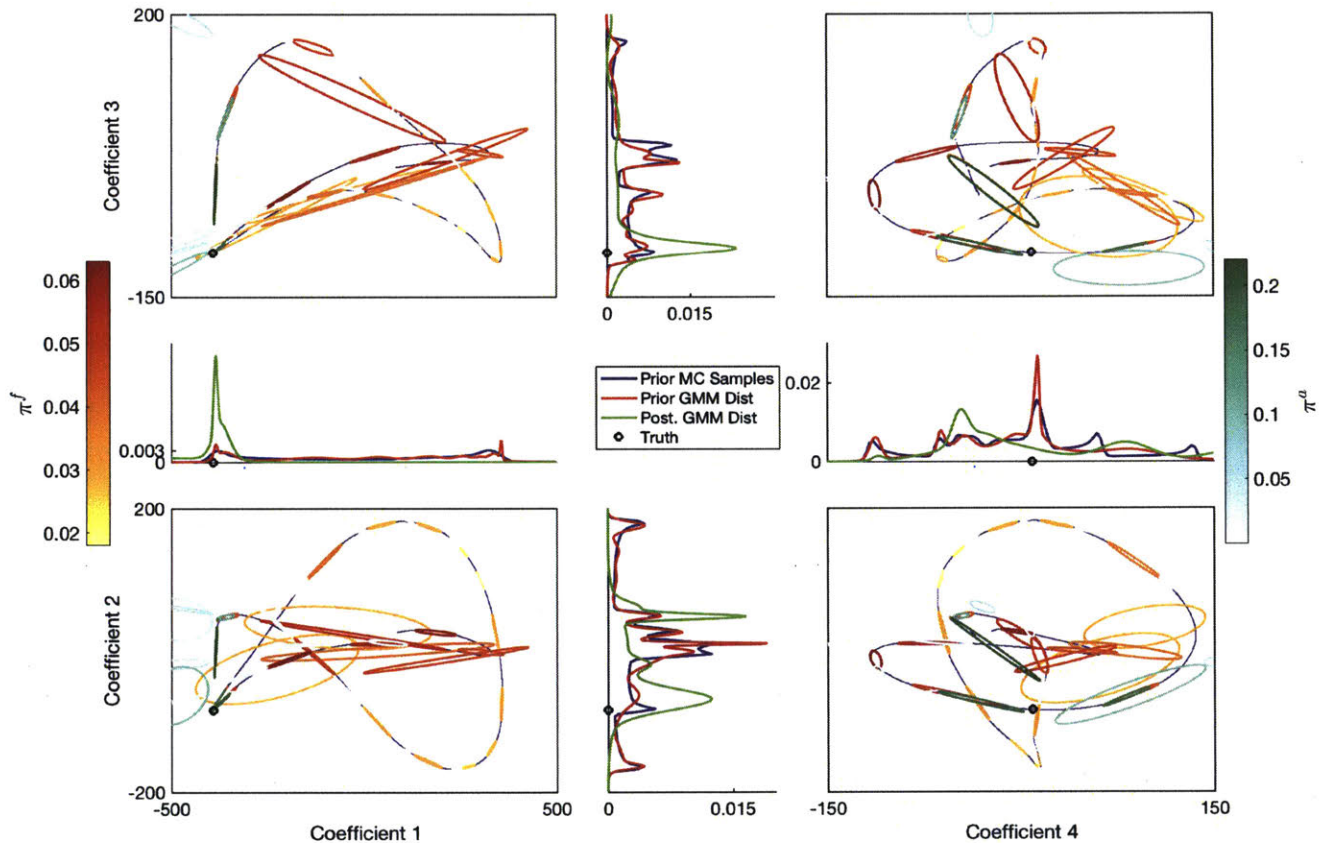

Figure 3-8: Joint GMM fits considering observations in Eulerian velocity. In the four boxes, we show pairwise joint distributions of two stochastic coefficients. Ensemble members representing the prior are shown in blue along with the prior and posterior GMM fits. One standard-deviation contours of the different Gaussian components are displayed and colored by the weight of the component i.e. π_j^f for the prior GMM (see colorbar on the left) and π_j^a for the posterior GMM (see colorbar on the right). The 1D marginal densities of the prior are computed by a kernel dressing scheme and are shown in blue. The marginal prior and posterior PDFs of each stochastic coefficient as obtained through the GMM fits are also plotted (see legend for color association).

(a) u velocity　　　　　　(b) v velocity

Figure 3-9: Distributions of velocity at the observation locations (left) Prior distribution, observation with it's associated Gaussian distribution, posterior distribution and true solution of u velocity; (right) Prior distribution, observation with it's associated Gaussian distribution, posterior distribution and true solution of v velocity

3.6　Summary

In this chapter, we extended the GMM-DO filter for the joint assimilation of Eulerian and Lagrangian variables using the augmentation approach. We illustrated the capability of this approach through two test cases based on the stochastic double-gyre flow considering observations in Eulerian or Lagrangian variables.

Chapter 4

Conclusions and Future Work

In this chapter, we summarize the work that was done in this thesis focusing on some of the key results obtained. This is followed by a discussion of the future directions.

4.1 Summary and Conclusions

In the past few decades, the role of data in making accurate predictions has increased drastically. This motivates the use of measurements from fixed Eulerian and non-stationary dynamic Lagrangian sensors in the ocean. One of the main contributions of this thesis is the formulation of a methodology that is capable of assimilating Eulerian and Lagrangian information while respecting non-linear dynamics and capturing non-Gaussian statistics. We were successful in doing this by using the Dynamically Orthogonal (DO) field equations for propagating uncertainty in the stochastic dynamical models and the GMM-DO filter for data assimilation.

First, numerical schemes were developed for the stochastic DO Navier-Stokes equations to improve the consistency, accuracy, efficiency and stability in the DO solution. A fundamental numerical challenge is maintaining consistency between MC and DO advection which involves the evaluation of advection by DO modes which don't contain any directional information. The issue of maintaining consistency between DO and MC advection was addressed by using centered advection schemes which do not require any directional information combined with the linear and explicit Shapiro

filter for suppressing oscillations. In order to further ensure accuracy and stability for long time-integrations, semi-implicit IMEX schemes were applied to the stochastic DO Navier-Stokes equations. Projection schemes for the linear multi-step IMEX and IMEX Runge-Kutta schemes were obtained. We also presented strategies for re-orthonormalization that ensure that DO modes remain orthonormal throughout the simulation time and allow us to continuously track the DO solution. Finally, the advantages posed by these numerical schemes were illustrated through the test cases of stochastic passive tracer advection in a deterministic swirl flow, stochastic flow past a cylinder, and stochastic lid-driven cavity flow. As a whole, for given uncertain initial conditions, these schemes provide ensemble of velocity fields that are comparable to the Monte Carlo (MC) solution at a fraction of the computational cost.

Second, the GMM-DO filter was extended to the joint assimilation of Eulerian variables and Lagrangian variables. The DO equations are used to obtain the ensemble of velocity fields which are in turn used as inputs for the different realizations of drifter/float trajectories, stochastic flow-map, and thus stochastic FTLE fields used for identifying Lagrangian Coherent Structures (LCS) in the flow. As new data becomes available, assimilation is carried out using a state augmentation approach. This has an immediate consequence. Irrespective of which variable is measured, the other variables describing the ocean state are updated through mutual information. This was illustrated for test cases based on the stochastic double gyre flow over one assimilation step.

4.2   Future Work

The two main areas that we worked on were (i) numerical schemes for uncertainty propagation in high-dimensional stochastic fluid flows and (ii) Bayesian state estimation when sparse observations in Eulerian and Lagrangian data are available. Next, we outline some possible future directions within these two areas.

To ensure consistency between the evaluation of advection in the Monte Carlo sense and in the stochastic DO Navier-Stokes equations, we currently use centered

advection schemes with Shapiro filtering to suppress oscillations. Other advection schemes such as essentially non-oscillatory scheme (ENO) or weighed essentially non-oscillatory schemes (WENO) using centered fluxes [121, 118] may be investigated or possibly update so that they do not require directional information. As these schemes are in general nonlinear and not bilinear like the centered schemes, direct consistency between MC and DO advection is not ensured but is a good approximation if these schemes are of low polynomial order. These schemes will be especially important in flows with very high velocity gradients or shocks where filtering may not prevent growth of spurious numerical oscillations introduced by centered schemes.

As part of the numerical schemes for the DO equations, we discussed projection schemes in the rotational form for IMEX linear multi-step and IMEX Runge-Kutta time marching schemes. Irrespective of the order of time-integration used, velocity and pressure [32] can be at most second order accurate. One way to increase accuracy is to carry out multiple reiterations of the projection step using the corrected pressure obtained. This has already been successfully implemented and validated in the case of the deterministic Navier-Stokes equations [3, 2]. Applying this approach to the stochastic DO Navier-Stokes equations would further increase the accuracy and consistency of the DO solution.

Additionally, the stability analysis of the IMEX schemes as applied to the DO equations needs to be better understood. Of utmost consequence is the understanding of how stability of the different schemes may vary with Reynolds number of the flow. This would give an insight into the conditions that need to be imposed on the size of the time-step during time-marching.

Finally in this work, we restricted ourselves to the case of constant number of modes n_s when integrating the DO equations through time. This limits the amount of uncertainty that can be captured. More modes may need to be introduced to capture the uncertainty that arises from the interactions of existing modes in time [24]. This motivates the need to look at combining adaptivity with the numerical schemes introduced here.

In Chapter 3, we presented the theory and methodology for joint Eulerian-Lagrangian

data assimilation. Applications of sequential filtering need to be investigated. This could be followed by smoothing, parameter estimation, and model learning [56, 77, 76, 75]. Finally, this would need to be applied to realistic ocean fields [37, 36]. A step in this direction would be to extend the numerical schemes presented for the stochastic DO Navier-Stokes equations, to the case of the stochastic ocean primitive equations [55, 112].

The methodology would also need to be extended to assimilate vertically-integrated or subsurface measurements more complex observation model may need to be created in addition to using the state augmentation approach. Lagrangian measurements of biological variables [64, 10, 60] and of acoustical variables [59, 57] would also need to be included.

An important to question to ask is where should I place sensors so as to maximize the information that I collect about the state variables that I am evolving? This forms the question of adaptive sampling [56]. A secondary question may be at a given observation location, making measurements in which variable is more informative? In the case of drifters, the question can be rephrased as "Where should I release drifters so as to maximize information about the state variables (prognostic variables and structures in the flow) through the observations of drifter trajectories?" This motivates the need to formulate a methodology for drifter deployment.

Finally, we note that several recent sea experiments involving gliders, floats, and drifters [15, 61, 31, 65] indicate that the present results will be very useful in a wide range of ocean science and engineering applications.

Bibliography

[1] ALEXANDERIAN, A. A brief note on the karhunen-lo\eve expansion. *arXiv preprint arXiv:1509.07526* (2015).

[2] AOUSSOU, J., LIN, J., AND LERMUSIAUX, P. F. J. Iterated pressure-correction projection methods for the unsteady incompressible Navier-Stokes equations. *Journal of Computational Physics* (2018). Sub-judice.

[3] AOUSSOU, J. P. An iterative pressure-correction method for the unsteady incompressible navier-stokes equation. Master's thesis, Massachusetts Institute of Technology, Department of Mechanical Engineering, Cambridge, Massachusetts, June 2016.

[4] APTE, A., AND JONES, C. K. The impact of nonlinearity in lagrangian data assimilation. *Nonlinear Processes in Geophysics 20*, 3 (2013), 329–341.

[5] APTE, A., JONES, C. K., AND STUART, A. A bayesian approach to lagrangian data assimilation. *Tellus A 60*, 2 (2008), 336–347.

[6] AREF, H. Stirring by chaotic advection. *Journal of fluid mechanics 143* (1984), 1–21.

[7] AREF, H. Chaotic advection of fluid particles. *Philosophical Transactions of the Royal Society of London A: Mathematical, Physical and Engineering Sciences 333*, 1631 (1990), 273–288.

[8] ASCHER, U. M., RUUTH, S. J., AND SPITERI, R. J. Implicit-explicit runge-kutta methods for time-dependent partial differential equations. *Applied Numerical Mathematics 25*, 2 (1997), 151–167.

[9] ASCHER, U. M., RUUTH, S. J., AND WETTON, B. T. Implicit-explicit methods for time-dependent partial differential equations. *SIAM Journal on Numerical Analysis 32*, 3 (1995), 797–823.

[10] BEŞIKTEPE, Ş. T., LERMUSIAUX, P. F. J., AND ROBINSON, A. R. Coupled physical and biogeochemical data-driven simulations of Massachusetts Bay in late summer: real-time and post-cruise data assimilation. *Journal of Marine Systems 40–41* (2003), 171–212.

[11] BERLAND, J., BOGEY, C., MARSDEN, O., AND BAILLY, C. High-order, low dispersive and low dissipative explicit schemes for multiple-scale and boundary problems. *Journal of Computational Physics 224*, 2 (2007), 637–662.

[12] BILMES, J. A., ET AL. A gentle tutorial of the em algorithm and its application to parameter estimation for gaussian mixture and hidden markov models. *International Computer Science Institute 4*, 510 (1998), 126.

[13] CARTER, E. F. Assimilation of lagrangian data into a numerical model. *Dynamics of atmospheres and oceans 13*, 3-4 (1989), 335–348.

[14] CASELLA, G., AND BERGER, R. L. *Statistical inference*, vol. 2. Duxbury Pacific Grove, CA, 2002.

[15] CENTURIONI, L. R., ET AL. Northern Arabian Sea circulation-autonomous research (NASCar): A research initiative based on autonomous sensors. *Oceanography 30*, 2 (June 2017), 74–87. Special issue on Autonomous and Lagrangian Platforms and Sensors (ALPS).

[16] DEBUSSCHERE, B. J., NAJM, H. N., PÉBAY, P. P., KNIO, O. M., GHANEM, R. G., AND LE MAIÂĄĄ TRE, O. P. Numerical challenges in the use of polynomial chaos representations for stochastic processes. *SIAM journal on scientific computing 26*, 2 (2004), 698–719.

[17] DEODATIS, G. Weighted integral method. i: stochastic stiffness matrix. *Journal of Engineering Mechanics 117*, 8 (1991), 1851–1864.

[18] DEODATIS, G., AND SHINOZUKA, M. Weighted integral method. ii: response variability and reliability. *Journal of Engineering Mechanics 117*, 8 (1991), 1865–1877.

[19] DOWD, M. Bayesian statistical data assimilation for ecosystem models using markov chain monte carlo. *Journal of Marine Systems 68*, 3 (2007), 439–456.

[20] EVENSEN, G. The ensemble kalman filter: Theoretical formulation and practical implementation. *Ocean dynamics 53*, 4 (2003), 343–367.

[21] FALISSARD, F. Genuinely multi-dimensional explicit and implicit generalized shapiro filters for weather forecasting, computational fluid dynamics and aeroacoustics. *Journal of Computational Physics 253* (2013), 344–367.

[22] FALISSARD, F. Uneven-order decentered shapiro filters for boundary filtering. *Journal of Computational Physics 292* (2015), 168–175.

[23] FEPPON, F. Riemannian geometry of matrix manifolds for Lagrangian uncertainty quantification of stochastic fluid flows. Master's thesis, Massachusetts Institute of Technology, Department of Mechanical Engineering, Cambridge, Massachusetts, Feb. 2017.

[24] FEPPON, F., AND LERMUSIAUX, P. F. J. Dynamically orthogonal numerical schemes for efficient stochastic advection and Lagrangian transport. *SIAM Review* (2018). In press.

[25] FEPPON, F., AND LERMUSIAUX, P. F. J. A geometric approach to dynamical model-order reduction. *SIAM Journal on Matrix Analysis and Applications* (2018). In press.

[26] FERZIGER, J. H., AND PERIC, M. *Computational methods for fluid dynamics.* Springer Science & Business Media, 2012.

[27] GAITONDE, D. V., AND VISBAL, M. R. Padé-type higher-order boundary filters for the navier-stokes equations. *AIAA journal 38*, 11 (2000), 2103–2112.

[28] GELB, A. *Applied Optimal Estimation.* MIT press, 1974.

[29] GHIL, M., AND MALANOTTE-RIZZOLI, P. Data assimilation in meteorology and oceanography. *Advances in geophysics 33* (1991), 141–266.

[30] GRIFFA, A., HAZA, A., ÖZGÖKMEN, T. M., MOLCARD, A., TAILLANDIER, V., SCHROEDER, K., CHANG, Y., AND POULAIN, P.-M. Investigating transport pathways in the ocean. *Deep Sea Research Part II: Topical Studies in Oceanography 85* (2013), 81–95.

[31] GROUP, M. NSF-ALPHA Sea Experiment 2017. `http://mseas.mit.edu/Sea_exercises/NSF_ALPHA/2017/index.html`, 2017.

[32] GUERMOND, J., MINEV, P., AND SHEN, J. An overview of projection methods for incompressible flows. *Computer methods in applied mechanics and engineering 195*, 44 (2006), 6011–6045.

[33] GUERMOND, J., AND SHEN, J. On the error estimates for the rotational pressure-correction projection methods. *Mathematics of Computation 73*, 248 (2004), 1719–1737.

[34] GUPTA, A. Bayesian inference of obstacle systems and coupled biogeochemical-physical models. Master's thesis, Indian Institute of Technology Kanpur, Department of Mechanical Engineering, Kanpur, India, June 2016.

[35] GUPTA, A., AND LERMUSIAUX, P. F. J. Boundary conditions for stochastic DO equations. MSEAS Report, Department of Mechanical Engineering, Massachusetts Institute of Technology, Cambridge, MA, 2016.

[36] HALEY, JR., P. J., AGARWAL, A., AND LERMUSIAUX, P. F. J. Optimizing velocities and transports for complex coastal regions and archipelagos. *Ocean Modeling 89* (2015), 1–28.

105

[37] HALEY, JR., P. J., AND LERMUSIAUX, P. F. J. Multiscale two-way embedding schemes for free-surface primitive equations in the "Multidisciplinary Simulation, Estimation and Assimilation System". *Ocean Dynamics 60*, 6 (Dec. 2010), 1497–1537.

[38] HALEY, JR., P. J., LERMUSIAUX, P. F. J., ROBINSON, A. R., LESLIE, W. G., LOGOUTOV, O., COSSARINI, G., LIANG, X. S., MORENO, P., RAMP, S. R., DOYLE, J. D., BELLINGHAM, J., CHAVEZ, F., AND JOHNSTON, S. Forecasting and reanalysis in the Monterey Bay/California Current region for the Autonomous Ocean Sampling Network-II experiment. *Deep Sea Research Part II: Topical Studies in Oceanography 56*, 3–5 (Feb. 2009), 127–148. doi:10.1016/j.dsr2.2008.08.010.

[39] HALLER, G. Finding finite-time invariant manifolds in two-dimensional velocity fields. *Chaos: An Interdisciplinary Journal of Nonlinear Science 10*, 1 (2000), 99–108.

[40] HALLER, G. Distinguished material surfaces and coherent structures in three-dimensional fluid flows. *Physica D: Nonlinear Phenomena 149*, 4 (2001), 248–277.

[41] HALLER, G. Lagrangian coherent structures. *Annual Review of Fluid Mechanics 47* (2015), 137–162.

[42] HALLER, G., AND YUAN, G. Lagrangian coherent structures and mixing in two-dimensional turbulence. *Physica D: Nonlinear Phenomena 147*, 3 (2000), 352–370.

[43] HERNANDEZ, F., TRAON, P.-Y. L., AND BARTH, N. H. Optimizing a drifter cast strategy with a genetic algorithm. *Journal of Atmospheric and Oceanic Technology 12*, 2 (1995), 330–345.

[44] HOFFMANN, W. Iterative algorithms for gram-schmidt orthogonalization. *Computing 41*, 4 (1989), 335–348.

[45] HOLMES, P. *Turbulence, coherent structures, dynamical systems and symmetry.* Cambridge university press, 2012.

[46] IDE, K., KUZNETSOV, L., AND JONES, C. K. Lagrangian data assimilation for point vortex systems*. *Journal of Turbulence 3*, 053 (2002).

[47] ISHIKAWA, Y., AWAJI, T., AKITOMO, K., AND QIU, B. Successive correction of the mean sea surface height by the simultaneous assimilation of drifting buoy and altimetric data. *Journal of Physical Oceanography 26*, 11 (1996), 2381–2397.

[48] JABLONOWSKI, C., AND WILLIAMSON, D. L. The pros and cons of diffusion, filters and fixers in atmospheric general circulation models. In *Numerical Techniques for Global Atmospheric Models.* Springer, 2011, pp. 381–493.

[49] JAZWINSKI, A. H. *Stochastic processes and filtering theory.* Courier Corporation, 2007.

[50] KAMACHI, M., AND O'BRIEN, J. Continuous data assimilation of drifting buoy trajectory into an equatorial pacific ocean model. *Journal of Marine Systems 6*, 1-2 (1995), 159–178.

[51] KUZNETSOV, L., IDE, K., AND JONES, C. K. A method for assimilation of lagrangian data. *Monthly Weather Review 131*, 10 (2003), 2247–2260.

[52] LE MAÎTRE, O. P., AND KNIO, O. M. *Introduction: Uncertainty Quantification and Propagation.* Springer, 2010.

[53] LERMUSIAUX, P., ANDERSON, D., AND LOZANO, C. On the mapping of multivariate geophysical fields: Error and variability subspace estimates. *Quarterly Journal of the Royal Meteorological Society 126*, 565 (2000), 1387–1429.

[54] LERMUSIAUX, P. F. J. Data assimilation via Error Subspace Statistical Estimation, part II: Mid-Atlantic Bight shelfbreak front simulations, and ESSE validation. *Monthly Weather Review 127*, 7 (July 1999), 1408–1432.

[55] LERMUSIAUX, P. F. J. Uncertainty estimation and prediction for interdisciplinary ocean dynamics. *Journal of Computational Physics 217*, 1 (2006), 176–199.

[56] LERMUSIAUX, P. F. J. Adaptive modeling, adaptive data assimilation and adaptive sampling. *Physica D: Nonlinear Phenomena 230*, 1 (2007), 172–196.

[57] LERMUSIAUX, P. F. J., AND CHIU, C.-S. Four-dimensional data assimilation for coupled physical-acoustical fields. In *Acoustic Variability, 2002* (Saclantcen, 2002), N. G. Pace and F. B. Jensen, Eds., Kluwer Academic Press, pp. 417–424.

[58] LERMUSIAUX, P. F. J., CHIU, C.-S., GAWARKIEWICZ, G. G., ABBOT, P., ROBINSON, A. R., MILLER, R. N., HALEY, JR, P. J., LESLIE, W. G., MAJUMDAR, S. J., PANG, A., AND LEKIEN, F. Quantifying uncertainties in ocean predictions. *Oceanography 19*, 1 (2006), 92–105.

[59] LERMUSIAUX, P. F. J., CHIU, C.-S., AND ROBINSON, A. R. Modeling uncertainties in the prediction of the acoustic wavefield in a shelfbreak environment. In *Proceedings of the 5th International conference on theoretical and computational acoustics* (May 21-25 2002), E.-C. Shang, Q. Li, and T. F. Gao, Eds., World Scientific Publishing Co., pp. 191–200. Refereed invited manuscript.

[60] LERMUSIAUX, P. F. J., HALEY, P. J., LESLIE, W. G., AGARWAL, A., LOGUTOV, O., AND BURTON, L. J. Multiscale physical and biological dynamics in the Philippine Archipelago: Predictions and processes. *Oceanography 24*, 1 (2011), 70–89. Special Issue on the Philippine Straits Dynamics Experiment.

[61] LERMUSIAUX, P. F. J., HALEY, JR., P. J., JANA, S., GUPTA, A., KULKA-RNI, C. S., MIRABITO, C., ALI, W. H., SUBRAMANI, D. N., DUTT, A., LIN, J., SHCHERBINA, A., LEE, C., AND GANGOPADHYAY, A. Optimal planning and sampling predictions for autonomous and lagrangian platforms and sensors in the northern Arabian Sea. *Oceanography 30*, 2 (June 2017), 172–185. Special issue on Autonomous and Lagrangian Platforms and Sensors (ALPS).

[62] LERMUSIAUX, P. F. J., MALANOTTE-RIZZOLI, P., STAMMER, D., CARTON, J., CUMMINGS, J., AND MOORE, A. M. Progress and prospects of U.S. data assimilation in ocean research. *Oceanography 19*, 1 (2006), 172–183.

[63] LERMUSIAUX, P. F. J., AND ROBINSON, A. R. Data assimilation via Error Subspace Statistical Estimation, part I: Theory and schemes. *Monthly Weather Review 127*, 7 (1999), 1385–1407.

[64] LERMUSIAUX, P. F. J., ROBINSON, A. R., HALEY, P. J., AND LESLIE, W. G. Advanced interdisciplinary data assimilation: Filtering and smoothing via error subspace statistical estimation. In *Proceedings of The OCEANS 2002 MTS/IEEE conference* (2002), Holland Publications, pp. 795–802.

[65] LERMUSIAUX, P. F. J., SUBRAMANI, D. N., LIN, J., KULKARNI, C. S., GUPTA, A., DUTT, A., LOLLA, T., HALEY, JR., P. J., ALI, W. H., MIRABITO, C., AND JANA, S. A future for intelligent autonomous ocean observing systems. In *The Science of Ocean Prediction*, vol. 17 of *The Sea*. Sears Foundation for Marine Research, 2017. In press. Special issue of Journal of Marine Research, vol. 75.

[66] LEUNG, S. An eulerian approach for computing the finite time lyapunov exponent. *Journal of computational physics 230*, 9 (2011), 3500–3524.

[67] LEUNG, S. The backward phase flow method for the eulerian finite time lyapunov exponent computations. *Chaos: An Interdisciplinary Journal of Nonlinear Science 23*, 4 (2013), 043132.

[68] LEVEQUE, R. J. *Finite volume methods for hyperbolic problems*, vol. 31. Cambridge university press, 2002.

[69] LIN, G., SU, C.-H., AND KARNIADAKIS, G. E. Predicting shock dynamics in the presence of uncertainties. *Journal of Computational Physics 217*, 1 (2006), 260–276.

[70] LIN, J. Notes on re-orthonormalization, 2017.

[71] LIN, J., AND LERMUSIAUX, P. F. J. Bayesian learning for high-dimensional dynamical models with application to two-dimensional turbulent bottom gravity currents. In preparation.

[72] Liu, W. K., Belytschko, T., and Mani, A. Probabilistic finite elements for nonlinear structural dynamics. *Computer Methods in Applied Mechanics and Engineering 56*, 1 (1986), 61–81.

[73] Liu, W. K., Belytschko, T., and Mani, A. Random field finite elements. *International journal for numerical methods in engineering 23*, 10 (1986), 1831–1845.

[74] Loeve, M. Probability theory, vol. ii. *Graduate texts in mathematics 46* (1978), 0–387.

[75] Lolla, T., and Lermusiaux, P. F. J. A Gaussian mixture model smoother for continuous nonlinear stochastic dynamical systems: Applications. *Monthly Weather Review 145* (July 2017), 2763–2790.

[76] Lolla, T., and Lermusiaux, P. F. J. A Gaussian mixture model smoother for continuous nonlinear stochastic dynamical systems: Theory and scheme. *Monthly Weather Review 145* (July 2017), 2743–2761.

[77] Lu, P. G. Y. Bayesian inference of stochastic dynamical models. Master's thesis, Massachusetts Institute of Technology, Department of Mechanical Engineering, Cambridge, Massachusetts, February 2013.

[78] Lumley, J. L. *Stochastic tools in turbulence.* Courier Corporation, 2007.

[79] Lumpkin, R., and Pazos, M. Measuring surface currents with surface velocity program drifters: the instrument, its data, and some recent results. *Lagrangian analysis and prediction of coastal and ocean dynamics* (2007), 39–67.

[80] McLachlan, G., and Peel, D. *Finite mixture models.* John Wiley & Sons, 2004.

[81] Mead, J. Assimilation of simulated float data in lagrangian coordinates. *Ocean Modelling 8*, 4 (2005), 369–394.

[82] Molcard, A., Piterbarg, L. I., Gri, A., and Mariano, A. J. Assimilation of drifter positions for the reconstruction of the eulerian circulation eld. *Journal of Geophysical Research* (2003).

[83] Mudrick, S. On the use of a scale-dependent filter in channel model integrations. *Journal of Computational Physics 20*, 1 (1976), 33–49.

[84] Özgökmen, T. M., Molcard, A., Chin, T. M., Piterbarg, L. I., and Griffa, A. Assimilation of drifter observations in primitive equation models of midlatitude ocean circulation. *Journal of Geophysical Research: Oceans 108*, C7 (2003), n/a–n/a. 3238.

[85] Papoulis, A., and Pillai, S. U. *Probability, random variables, and stochastic processes.* Tata McGraw-Hill Education, 2002.

[86] PINARDI, N., CAVALERI, L., COPPINI, G., MEY, P. D., FRATIANNI, C., HUTHNANCE, J., LERMUSIAUX, P. F. J., NAVARRA, A., PRELLER, R., AND TIBALDI, S. From weather to ocean predictions: an historical viewpoint. In *The Science of Ocean Prediction*, vol. 17 of *The Sea*. Sears Foundation for Marine Research, May 2017, pp. 103–159. Special issue of Journal of Marine Research, vol. 75.

[87] PURSER, R. J. The filtering of meteorological fields. *Journal of climate and applied meteorology 26*, 12 (1987), 1764–1769.

[88] RAYMOND, W. H., AND GARDER, A. A review of recursive and implicit filters. *Monthly weather review 119*, 2 (1991), 477–495.

[89] ROSSBY, T. Evolution of lagrangian methods in oceanography. *Lagrangian Analysis and Prediction of Coastal and Ocean Dynamics* (2007), 1–38.

[90] RUDNICK, D. L., AND COLE, S. T. On sampling the ocean using underwater gliders. *Journal of Geophysical Research: Oceans 116*, C8 (2011).

[91] RUDNICK, D. L., DAVIS, R. E., ERIKSEN, C. C., FRATANTONI, D. M., AND PERRY, M. J. Underwater gliders for ocean research. *Marine Technology Society Journal 38*, 2 (2004), 73–84.

[92] SALMAN, H. A hybrid grid/particle filter for lagrangian data assimilation. i: Formulating the passive scalar approximation. *Quarterly Journal of the Royal Meteorological Society 134*, 635 (2008), 1539–1550.

[93] SALMAN, H. A hybrid grid/particle filter for lagrangian data assimilation. ii: Application to a model vortex flow. *Quarterly Journal of the Royal Meteorological Society 134*, 635 (2008), 1551–1565.

[94] SALMAN, H., KUZNETSOV, L., JONES, C., AND IDE, K. A method for assimilating lagrangian data into a shallow-water-equation ocean model. *Monthly Weather Review 134*, 4 (2006), 1081–1101.

[95] SAPSIS, T. P., AND LERMUSIAUX, P. F. Dynamically orthogonal field equations for continuous stochastic dynamical systems. *Physica D: Nonlinear Phenomena 238*, 23 (2009), 2347–2360.

[96] SAPSIS, T. P., AND LERMUSIAUX, P. F. J. Dynamically orthogonal field equations for continuous stochastic dynamical systems. *Physica D: Nonlinear Phenomena 238*, 23–24 (Dec. 2009), 2347–2360. doi:10.1016/j.physd.2009.09.017.

[97] SAPSIS, T. P., AND LERMUSIAUX, P. F. J. Dynamical criteria for the evolution of the stochastic dimensionality in flows with uncertainty. *Physica D: Nonlinear Phenomena 241*, 1 (2012), 60–76.

[98] SÄRKKÄ, S. *Bayesian Filtering and Smoothing*. No. 3. Cambridge University Press, 2013.

[99] SCHÄR, C., AND DURRAN, D. R. Vortex formation and vortex shedding in continuously stratified flows past isolated topography. *Journal of the atmospheric sciences 54*, 4 (1997), 534–554.

[100] SHADDEN, S. C., LEKIEN, F., AND MARSDEN, J. E. Definition and properties of lagrangian coherent structures from finite-time lyapunov exponents in two-dimensional aperiodic flows. *Physica D: Nonlinear Phenomena 212*, 3 (2005), 271–304.

[101] SHAPIRO, R. Smoothing, filtering, and boundary effects. *Reviews of geophysics 8*, 2 (1970), 359–387.

[102] SHAPIRO, R. The use of linear filtering as a parameterization of atmospheric diffusion. *Journal of the Atmospheric Sciences 28*, 4 (1971), 523–531.

[103] SHAPIRO, R. Linear filtering. *Mathematics of computation 29*, 132 (1975), 1094–1097.

[104] SHUMAN, F. Numerical methods in weather prediction: Smoothing and filtering. *Mon. Weath. Rev 85* (1957), 357–361.

[105] SILVERMAN, B. W. *Density estimation for statistics and data analysis*, vol. 26. CRC press, 1986.

[106] SLIVINSKI, L., SPILLER, E., APTE, A., AND SANDSTEDE, B. A hybrid particle–ensemble kalman filter for lagrangian data assimilation. *Monthly Weather Review 143*, 1 (2015), 195–211.

[107] SNYDER, C., BENGTSSON, T., BICKEL, P., AND ANDERSON, J. Obstacles to high-dimensional particle filtering. *Monthly Weather Review 136*, 12 (2008), 4629–4640.

[108] SONDERGAARD, T. Data Assimilation with Gaussian Mixture Models using the Dynamically Orthogonal Field Equation. Master's thesis, Massachusetts Institute of Technology, Department of Mechanical Engineering, Cambridge, Massachusetts, September 2011.

[109] SONDERGAARD, T., AND LERMUSIAUX, P. F. J. Data assimilation with Gaussian Mixture Models using the Dynamically Orthogonal field equations. Part I: Theory and scheme. *Monthly Weather Review 141*, 6 (2013), 1737–1760.

[110] SONDERGAARD, T., AND LERMUSIAUX, P. F. J. Data assimilation with Gaussian Mixture Models using the Dynamically Orthogonal field equations. Part II: Applications. *Monthly Weather Review 141*, 6 (2013), 1761–1785.

[111] SPILLER, E., APTE, A., AND JONES, C. Assimilating en-route lagrangian observations. *Tellus A 65* (2013).

[112] SUBRAMANI, D. N. *Probabilistic Regional Ocean Predictions: Stochastic Fields and Optimal Planning.* PhD thesis, Massachusetts Institute of Technology, Department of Mechanical Engineering, Cambridge, Massachusetts, Feb. 2018.

[113] SUBRAMANI, D. N., HALEY, JR., P. J., AND LERMUSIAUX, P. F. J. Energy-optimal path planning in the coastal ocean. *Journal of Geophysical Research: Oceans 122* (2017), 3981–4003.

[114] SUBRAMANI, D. N., AND LERMUSIAUX, P. F. J. Risk-optimal path planning in uncertain, strong and dynamic flows. *Ocean Dynamics* (2017). To be submitted.

[115] SUBRAMANI, D. N., WEI, Q. J., AND LERMUSIAUX, P. F. J. Stochastic time-optimal path-planning in uncertain, strong, and dynamic flows. *Computer Methods in Applied Mechanics and Engineering* (2018). In press.

[116] TAILLANDIER, V., GRIFFA, A., AND MOLCARD, A. A variational approach for the reconstruction of regional scale eulerian velocity fields from lagrangian data. *Ocean Modelling 13*, 1 (2006), 1–24.

[117] TAILLANDIER, V., GRIFFA, A., POULAIN, P.-M., AND BÉRANGER, K. Assimilation of argo float positions in the north western mediterranean sea and impact on ocean circulation simulations. *Geophysical research letters 33*, 11 (2006).

[118] TITAREV, V., AND TORO, E. Weno schemes based on upwind and centred tvd fluxes. *Computers & Fluids 34*, 6 (2005), 705–720.

[119] TITAUD, O., BRANKART, J.-M., AND VERRON, J. On the use of finite-time lyapunov exponents and vectors for direct assimilation of tracer images into ocean models. *Tellus A 63*, 5 (2011), 1038–1051.

[120] TITAUD, O., VIDARD, A., SOUOPGUI, I., AND LE DIMET, F.-X. Assimilation of image sequences in numerical models. *Tellus A 62*, 1 (2010), 30–47.

[121] TORO, E., AND BILLETT, S. Centred tvd schemes for hyperbolic conservation laws. *IMA Journal of Numerical Analysis 20*, 1 (2000), 47–79.

[122] TREFETHEN, L. N., AND BAU III, D. *Numerical linear algebra*, vol. 50. Siam, 1997.

[123] UECKERMANN, M., AND LERMUSIAUX, P. Hybridizable discontinuous galerkin projection methods for navier–stokes and boussinesq equations. *Journal of Computational Physics 306* (2016), 390–421.

[124] UECKERMANN, M., LERMUSIAUX, P. F., AND SAPSIS, T. Numerical schemes for dynamically orthogonal equations of stochastic fluid and ocean flows. *Journal of Computational Physics 233* (2013), 272–294.

[125] UECKERMANN, M. P., LERMUSIAUX, P., AND SAPSIS, T. Numerical schemes and computational studies for dynamically orthogonal equations. *Reports in Ocean Science and Engineering 10* (2011).

[126] VAN LEER, B. Towards the ultimate conservative difference scheme. iv. a new approach to numerical convection. *Journal of computational physics 23*, 3 (1977), 276–299.

[127] VAN LEEUWEN, P. J. Particle filtering in geophysical systems. *Monthly Weather Review 137*, 12 (2009), 4089–4114.

[128] VERNIERES, G., JONES, C. K., AND IDE, K. Capturing eddy shedding in the gulf of mexico from lagrangian observations. *Physica D: Nonlinear Phenomena 240*, 2 (2011), 166–179.

[129] VISBAL, M. R., AND GAITONDE, D. V. Very high-order spatially implicit schemes for computational acoustics on curvilinear meshes. *Journal of Computational Acoustics 9*, 04 (2001), 1259–1286.

[130] XIONG, X., NAVON, I. M., AND UZUNOGLU, B. A note on the particle filter with posterior gaussian resampling. *Tellus A 58*, 4 (2006), 456–460.

[131] XIU, D. *Numerical methods for stochastic computations: a spectral method approach.* Princeton University Press, 2010.

[132] XIU, D., AND KARNIADAKIS, G. E. The wiener–askey polynomial chaos for stochastic differential equations. *SIAM journal on scientific computing 24*, 2 (2002), 619–644.

[133] YAMAZAKI, F., MEMBER, A., SHINOZUKA, M., AND DASGUPTA, G. Neumann expansion for stochastic finite element analysis. *Journal of Engineering Mechanics 114*, 8 (1988), 1335–1354.